(12) **LEVEL** III _____ AL-E 300744

DNA 4731F

ADA083885

ASSESSMENT OF ROCKETBORNE AND AIRBORNE INFRARED DATA

PhotoMetrics, Inc.
442 Marrett Road
Lexington, Massachusetts 02173

DTIC
ELECTE
S MAY 6 1980 D
B

30 November 1978

Final Report for Period 1 December 1977—31 October 1978

CONTRACT No. DNA 001-78-C-0093

DDC FILE COPY

Prepared for
Director
DEFENSE NUCLEAR AGENCY
Washington, D. C. 20305

80 3 18 020

Destroy this report when it is no longer
needed. Do not return to sender.

REPORT DOCUMENTATION PAGE		READ INSTRUCTIONS BEFORE COMPLETING FORM
1. REPORT NUMBER DNA 4731F	2. GOVT ACCESSION NO.	3. RECIPIENT'S CATALOG NUMBER
4. TITLE *(and Subtitle)* ASSESSMENT OF ROCKETBORNE AND AIRBORNE INFRARED DATA		5. TYPE OF REPORT & PERIOD COVERED Final Report for Period 1 Dec 77—31 Oct 78
		6. PERFORMING ORG. REPORT NUMBER PhM-09-78
7. AUTHOR*(s)* I. L. Kofsky D. P. Villanucci W. S. Andrus		8. CONTRACT OR GRANT NUMBER*(s)* DNA 001-78-C-0093
9. PERFORMING ORGANIZATION NAME AND ADDRESS PhotoMetrics, Inc. 442 Marrett Road Lexington, Massachusetts 02173		10. PROGRAM ELEMENT, PROJECT, TASK AREA & WORK UNIT NUMBERS Subtask I25AAXYX960-12
11. CONTROLLING OFFICE NAME AND ADDRESS Director Defense Nuclear Agency Washington, D.C. 20305		12. REPORT DATE 30 November 1978
		13. NUMBER OF PAGES 176
14. MONITORING AGENCY NAME & ADDRESS*(if different from Controlling Office)*		15. SECURITY CLASS *(of this report)* UNCLASSIFIED
		15a. DECLASSIFICATION DOWNGRADING SCHEDULE

16. DISTRIBUTION STATEMENT *(of this Report)*

Approved for public release; distribution unlimited.

17. DISTRIBUTION STATEMENT *(of the abstract entered in Block 20, if different from Report)*

18. SUPPLEMENTARY NOTES

This work sponsored by the Defense Nuclear Agency under RDT&E RMSS Code
B322078462 I25AAXYX96012 H2590D.

19. KEY WORDS *(Continue on reverse side if necessary and identify by block number)*

Nuclear-Effects Simulation	Upper Atmosphere
Infrared Radiation	Radiation Transport
Photometry of Aurora and Airglow	Molecular Radiation Processes
Excitation of Air	

20. ABSTRACT *(Continue on reverse side if necessary and identify by block number)*

Past DNA/AFGL aircraft data on 2.8μm-band emission from the auroral particle-
irradiated atmosphere were systematically evaluated, and a detailed plan was
formulated for measuring its spatial-temporal variations with a radiometer
of much higher angular and intensity resolution and for interpreting this
structure in terms of aeronomy code models. Data from HAES-program sounding
rocket A18.219-1 are presented that show a large, unexpected enhancement of
the near-limb 4.2-4.3μm radiance above 90 km altitude closely associated in

DD $\begin{smallmatrix}\text{FORM}\\ 1 \text{ JAN } 73\end{smallmatrix}$ 1473   EDITION OF 1 NOV 65 IS OBSOLETE

20.   ABSTRACT (Continued)

time and space with energy input from incoming charged particles.   In addition energy deposition within the field of the interferometric spectrometer HIRIS II was calculated from optical (and incoherent-scatter radar) data taken at ground stations; SWIR radiometry results from another rocket probe were found to be consistent with results from other HAES investigations; and infrared/ optical measurements of concentrations of minor species important in atmospheric deionization are suggested (in three Appendixes).

Most, but not all, of the enhancements in radiation from the zenith atmosphere near $2.8\mu m$ measured by the aircraft's wide-field radiometer show no statistically-significant difference from one another.   Interpreted as nitric oxide overtone emission, the energy yield of the complete vibrational-cascade sequence derived from this subset is $0.4_5\%$.

The relative intensity of air fluorescence-correlated 4.2-$4.3\mu m$ radiation at elevation angles near 10° increases with rocket-platform altitude to values an order of magnitude greater than previously observed on downleg of A18.219-1.   These near-prompt enhancements may be related to the large-scale "pumping" of the atmosphere inferred from zenith radiometer data from this and other rocket probes, and the layering in the downleg near-limb altitude profiles reported in HAES 69.

PREFACE

The High Altitude Effects Simulation (HAES) Program sponsored by the Defense Nuclear Agency since early 1970 comprises several interrelated theoretical and experimental activities, e.g., ICECAP (Infrared Chemistry Experiments – Coordinated Auroral Program). The objective of these activities is to provide information for the development and validation of predictive computer codes designed for use with high priority DoD radar, communications, and optical systems.

Since the inception of the HAES Program, significant achievements and results have been described in reports published by DNA, service laboratories, and other participating organizations. Reports published since early calendar 1974 have been identified with an assigned HAES number and appropriate activity acronym (e.g., ICECAP) as part of the title. A complete and current bibliography of all HAES reports is maintained and available on request at DASIAC, DoD Nuclear Information and Analysis Center, 816 State Street, Santa Barbara, CA 93102, Telephone (805) 965-0551.

This report, which is No. 79 in the HAES series and the Final Report on Contract DNA001-78-C-0093, covers PhotoMetrics' work in assessing and evaluating sounding rocket and aircraft data on infrared sky backgrounds between 01 Dec 77 and 31 Oct 78. It applies procedures developed and referenced in PhotoMetrics' previous HAES reports 4, 27, 59, and 69 (Ref's 1-4) and the 13-15 Jun 77 HAES Infrared Data Review (Ref 5). Simulation data from the following HAES-ICECAP sources are evaluated –

ACCESSION for		
NTIS	White Section	☑
DDC	Buff Section	☐
UNANNOUNCED		☐
JUSTIFICATION		
BY		
DISTRIBUTION/AVAILABILITY CODES		
Dist.	AVAIL. and/or SPECIAL	
A		

Multi-instrumented rocket A18.219-1, launched
from Poker Flat Research Range, AK on
25 Feb 74

HIRIS II rocket IC630.02-1A, launched from
Poker on 01 Apr 76

USAF NKC-135A 55-3120 (Air Force Geophysics
Laboratory's IR-Optical Flying Laboratory)
aircraft missions performed from Eielson AFB,
AK between 22 Feb 75 and 16 Sep 77.

SUMMARY

The objective of the work reported here is to evaluate data from DNA-sponsored field programs in which the excitation of infrared/optical emissions by nuclear explosions in the atmosphere is simulated. Four data sets, which provide information about the intensity and structure of sky background radiation at wavelengths near 2.8 and 4.3μm and $\sim$4-22μm, were considered. In addition planning was performed for measuring at high spatial resolution and interpreting 2.8μm-band radiation from the energetic particle-irradiated upper atmosphere, and for measurement of short-wavelength infrared sky backgrounds under the disturbance conditions of a total solar eclipse.

The data from three series of aircraft flights in the auroral oval of a wide (10°)-field 2.8μm-band radiometer and coaligned air-fluorescence photometer were analyzed by a uniformly-applied, unbiased method (Section I). Most of the enhancements in the zenith radiance, interpreted as emission in the overtone of nitric oxide vibrationally populated in reactions following ionization-excitation of air, show no statistically-significant variation from a yield of 0.4$_5$% (energy output in the complete cascade sequence). Some of the flight data segments, however, indicate larger or smaller chemiluminous efficiencies.

Procedures are presented for assessing and evaluating the differences in spatial-temporal structure between the visible and 2.8μm-band surface radiances that are expected to be resolved by the narrow (0.36°)-field aircraft instruments, to validate and provide input parameters for computer models of SWIR emission under nuclear excitation. The Test Plan for the forthcoming SWIR "structure-sources" investigation (Appendix I) documents the aircraft instrument system, lists the airglow and auroral features to which each element is sensitive, and provides further background material on the program.

Data that show a quite-unexpected large enhancement in 4.21-4.305μm (FWHM) near-limb radiance correlated in time and direction with absorption of incoming-particle energy by the atmosphere are

presented (Section IV). These increases are detectable over the altitude range 90-110 km on upleg of HAES rocket A18.219-1, on whose downleg segment some excess 4.3μm-band emission associated with nearby particle precipitation was also measured; the apparent photon yield on upleg is at times considerably greater. The total radiant fluxes at low elevation angles on upleg are about half those measured on downleg (reported in HAES 69). The enhancements, which extend into the "near-prompt" time frame the large-scale and altitude-layered increases previously reported, do not appear consistent with the currently-accepted DoD models of 4.3μm-band radiation above ~ 90 km.

Energy input into the air in the field of the cryocooled interferometric spectrometer HIRIS II was calculated for three of the spectrum scans (Section 2). The principal source of data is elevation-scanning photometers, with support from all-sky camera photographs (from which air-fluorescent radiance in the directions of the rocket instrument's field can be determined) and the DNA 617 radar. The low elevation-angle SWIR radiometer data taken at low altitudes from A18.219-1 on downleg are shown to be consistent with the atmospheric emissions expected from previous HAES investigations and earlier segments of the rocket's data (Section 3). A plan for measurement of OH Meinel and O_2 $^1\Delta - ^3\Sigma$ airglow emissions during the February 1979 total solar eclipse is presented, and the application of the data in investigations of atmospheric deionization is reviewed (Appendix II). Suggestions for infrared/optical remote sensing of column-concentrations and altitude profiles of other minor species important in ionospheric relaxation are also presented (in Appendixes IV and V).

TABLE OF CONTENTS

LIST OF ILLUSTRATIONS

LIST OF ILLUSTRATIONS (continued)

7

LIST OF ILLUSTRATIONS (continued)

        (Additional illustrations are presented in Appendixes
        I(3), II(4) and VI(2))

LIST OF TABLES

(Additional tables are presented in Appendixes
I(3), IV(1) and V(1))

SECTION 1

EVALUATION OF SWIR EMISSION DATA FROM THE WIDE-FIELD AIRCRAFT RADIOMETER

BACKGROUND

In this Section we analyze in a systematic way the results of measurements of short-wavelength infrared radiation from the auroral particle-excited upper atmosphere that were made from AFGL's IR-Optical Flying Laboratory (USAF NKC-135A S/N 55-3120) during the periods 22 Feb - 16 Mar 75 (ICECAP 75; listed in Table 5 of Ref 2), 28 Feb - 28 Mar 76 (ICECAP 76; Table 6 of Ref 3), and 06 Sep - 16 Sep 77 (Table 1). (Data from a flight series in Aug - Sep 78 were not available in time for inclusion in this review.) The principal goal of these aircraft missions is to investigate the processes leading to, and the spatial-temporal structure of, emission near 2.8μm from air ionized and excited by absorption of nuclear radiations.

Previous reports on the program of flights in the auroral oval are listed in Table 1 of Appendix I, which includes a reasonably comprehensive review of the methods used and results to date. Particular reference is made to Ref 6 's description of the $10°$-field filter radiometer, which was the prime instrument; and to Ref's 2 and 3's derivation of an "equilibrium" yield (or energy efficiency) for what is interpreted as chemiluminescence in the vibrational overtone of nitric oxide. Table 2 presents data on the atmosphere-emission features detected in each flight series by the zenith-pointing SWIR radiometer (and the narrow-field instrument scheduled for operation in Spring 1979).

OVERVIEW OF THE RADIOMETER-PHOTOMETER DATA

A long (~100 hr) measurement time has been needed because of the comparative infrequency of sufficiently intense particle precipitation for acceptable signal/noise ratio in the air fluorescence-associated SWIR emission. Effective "threshold" over the somewhat-variable hydroxyl nightglow is an energy input rate that produces IBC II optical

Table 1. SWIR-chemiluminescence data flights in 1977
(from Eielson AFB, AK; all times UT)[†]

Identification	Date	Take off	Land	Data Start	End
719	06 Sep	0255	1027	0428[*]	0934
				0428[+]	0934
720	11 Sep	0243	1107	0408	1021
				0404	1005
721	12 Sep	0422	0947	0526	0914
				0529	0914
722	13 Sep	0803	1202	0852	1138
				0825	1133
723	14 Sep	0253	1045	0404	1010
				0406	1010
724	15 Sep	0612	1243	0630	1206
				0630	1206
725	16 Sep	0331	1124	0613	1056
				0537	1040

----

[*]PhotoMetrics-operated all-sky camera

[+]PhotoMetrics-operated 12 channel photometer (Ref 7) and low light
level video (Ref 8)

[†]Flight trajectories not yet available

Table 2 . SWIR radiometer response factors

Flight Series	FOV	FWHM, μm	Nominal OH Δv = 1, kR *	Thermal Background, kR	Fraction of NO Δv = 2 †	Zenith Transmission to NO Δv = 2	Prompt Fluorescence kR/kR 3914 Å ++
IC 75	10°⊙	2.752-2.910	94** 58*** (10 Mar 75)	21‡ 95‡‡	0.56	~0.75	≲ 0.3
IC 76, Summer 77, Summer 78	10°⊙	2.828-3.041	156*** 159*** (28 Mar 76) Variable (77)	3‡ 8‡‡‡	0.46	~0.965 (Ref 6)	≃ 0.2
Spring 79	0.36°□	2.832-3.125	188**	4‡	0.48	~0.96	See Appendix 1

---

* Includes atmosphere's transmission, ~0.95

** Calculated adopting mean OH band intensities in Ref 9

*** Observed

‡ Model in HAES 27

‡‡ Inferred for 10 Mar 75, IC-75-4 (HAES 59)

‡‡‡ Inferred for 08 Mar 76, IC-76-10

† Kennealy-DelGreco population data, Billingsley cascade (Ref 10)

++ Principally A → B, B → W transitions, may be partially quenched depending on altitude distribution

aurora for $\frac{1}{4}$ - $\frac{1}{2}$ hour. For this reason quantitatively-useful results have been derived from only about half of the flight missions. Fig 1 shows typical "good" zenith radiance data, in the format published by the measurement group. The signals from the coaligned radiometers and photometer have been integrated to 1/36 Hz bandwidth by a three-pole (RC-bridge) low-pass filter, or by essentially equivalent digital filtering.

Co-variance of the signals from the 2.828 - 3.041μm FWHM radiometer above its near-dc OH baseline and air-fluorescence photo-meter is readily apparent in Fig 1, as it is in general when $\geqslant$ IBC II aurora lies in the instrument fields. However, in the first reductions of some of the higher signal/noise data (Table 5 of Ref 6) the ratios of absolute magnitudes of these radiance increases vary substantially among data segments. A preliminary comparison of the SWIR chemiluminous efficiencies derived from these ratios with the two physical parameters that might be expected to cause such a variation, altitude of maximum energy deposition and total dose into the air volume in the previous $\sim$ minutes, showed no systematic dependence of inferred yield on either.

It was therefore decided to reduce and evaluate all the available aircraft radiometry data by a systematic, uniformly-applied procedure, to allow confidence limits to be assigned to the measurements of SWIR chemiluminous yields.

The signal/noise of the 3914 $\overset{o}{A}$ band-fluorescence is so much higher than that of the infrared chemiluminescence that it introduces negligible additional uncertainty in the photon ratios. Noise in the SWIR data (refer to the middle trace in Fig 1) has both a component from the detector (extending in frequency down to $\sim$ 2 cycles/min) and a component due to residual error in correcting-out the background of hydroxyl $\Delta v = 1$ airglow, whose intensity is indicated by the OH $\Delta v = 2$ monitor (lower trace). Detector noise is stated as 6.0 kR rms with 1/36 Hz bandwidth (Table 2, Ref 6). The absolute value of the other noise component is roughly twice that in the OH overtone, since the

14
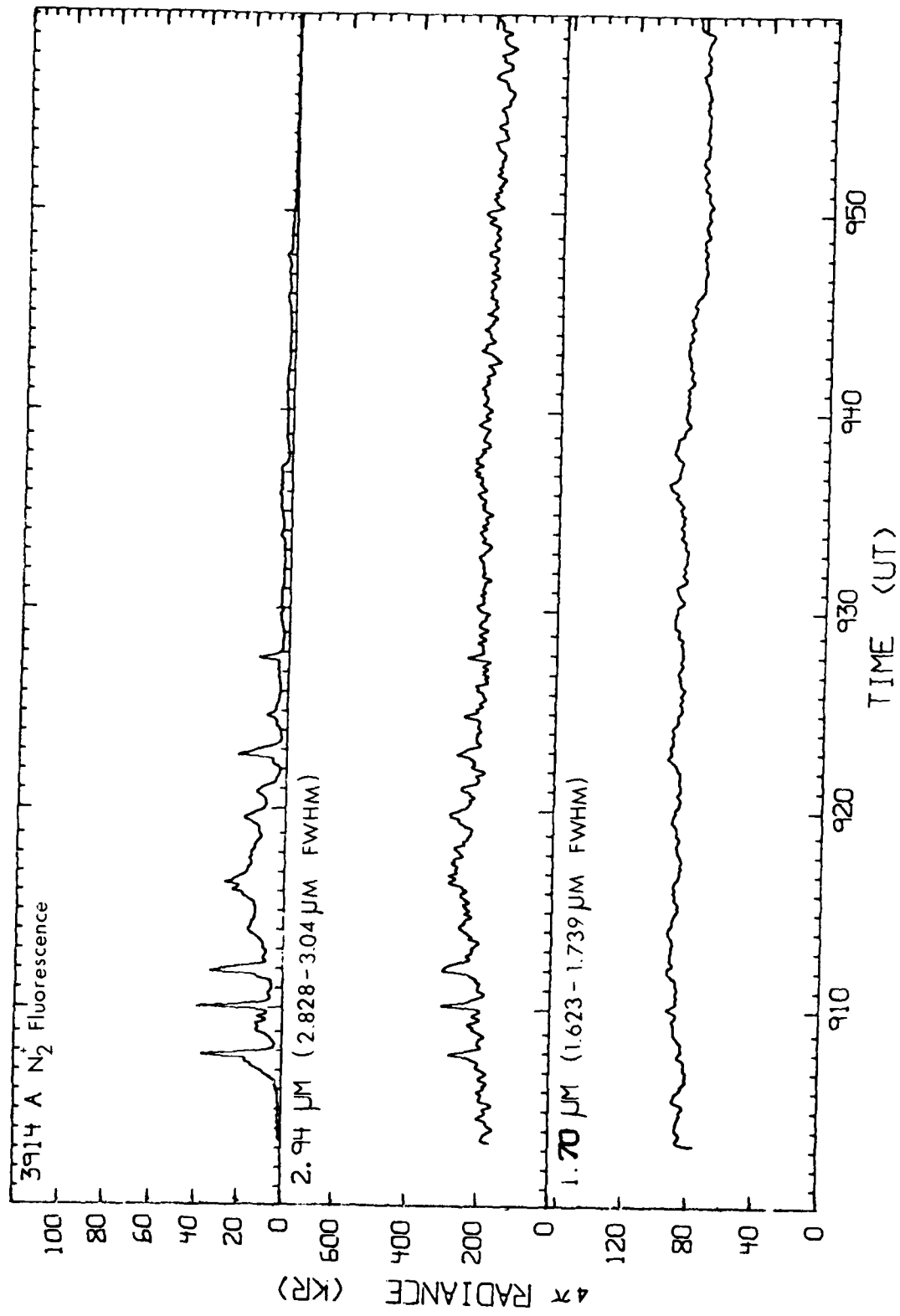
Figure 1. Typical high-quality zenith radiance data (for IC-76-16, 26 Mar 76; cross plot in Fig 2d).

15

ratio of intensities in the radiometer passbands – determined empirically – should be about a factor 2. A potential additional source of error is systematic offset between the two data streams, as evidenced by misalignment of maxima corresponding to isolated emitting features; a small shift on the time scale (of up to 9 sec; these shifts may be an effect to the signal integrating times) serves to realign all such peaks in a data flight.

STANDARD TREATMENT OF THE DATA

We reduced all the data taken under standard conditions in the same way, prior to considering instrument and flight effects that might introduce systematic differences among segments.

Cross-plots of simultaneously-measured photometer and radiometer signals (as in Ref 3) give meaningful results when the energy input, averaged over the fields of view, has small fractional variation over a "characteristic" time for SWIR output (that is, when predosing can be neglected). The projection of the fields at altitudes where incoming particle energy is absorbed is traversed by the aircraft in 1 min, and the data integration time needed to achieve adequate signal/ photon noise is about 1/2 min. As these times are longer than the expected time for aerochemical reactions to excite SWIR radiation (as described in Appendix I), even when the particle input is varying rapidly the cross-plot method would appear to provide a valid means for determining chemiluminescence yields.

The sampling or class interval (in reading from plots such as Fig 1) should be close to the stated integration time, 1/2 min. If it is less, the error in the photon ratio will be underestimated (since the data points are not independent of one another), and if it is more the field data are undersampled. Oversampling would not introduce artefacts or distortions in the slope of the regression curve, and as it appears from the traces that the "resolution" is somewhat less than 1/2 min we sampled each 15 sec. Since the statistical error in general

16

decreases with the square root of the number of data points, this interval decreases by $\sqrt{2}$ at the most the expected error in inferred yield.

The error estimate depends critically on the distribution of statistical weights assigned to data points. A cutoff at 2 kR 3914 $\overset{\circ}{A}$, which was applied in Ref 3 to the 10 Mar 75 flight data on the basis of visual lack of SWIR-fluorescence correlation at lower power-input levels, is one form of weighting; the concentration on isolated peaks in Ref 6's work is another form. To facilitate interpretation of the air-craft-program data we have reduced the cross-plots applying two separate statistical weightings, uniform counting all data points (no threshold) and proportional to the SWIR intensity.

Uniform weighting assumes equal absolute uncertainty for all radiometer data. In practice, those points at weak particle-precipitation levels do not appear to be levering the slope of the regression line, although their spread must be decreasing the correlation coefficient. The second weighting in effect assumes that the signal/noise increases with signal. Although this may appear justifiable on purely statistical grounds, the high input level data might be subject to greater instru-mental error because the more rapid changes in SWIR intensity (see Fig 1) accentuate the effects of imperfect match of the fields of view and other differences in response between the two instruments. If the fractional error is independent of the signal level, uniform weighting already gives higher statistical weight to the high-intensity data points.

To further facilitate interpretation of these data, the classical least-squares method applied to the scatter plots in Fig's 2a -g is briefly restated here. As previously noted, we assume that the 3914 $\overset{\circ}{A}$-band fluorescent intensities (abscissa, hereinafter referred to as x) have negligible uncertainty in comparison with that of the 2.9μm-band SWIR intensities (ordinate y). A linear relationship between output y and input x is assumed; the procedure could of course be extended to assess any quadratic term, which would indicate (in a statistical sense) nonlinearity of chemiluminescence yield. Slope and intercept of each

17
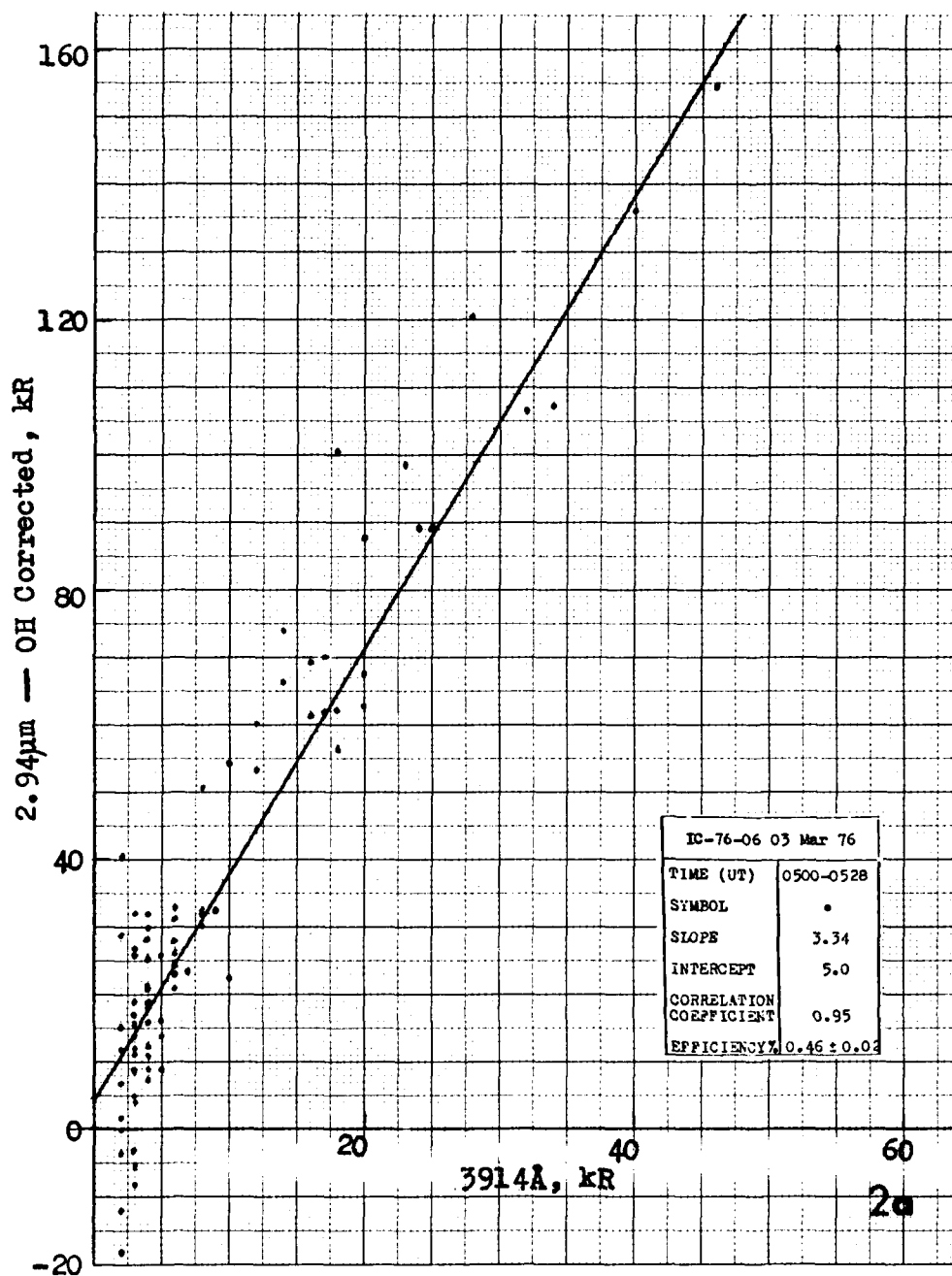
Figure 2a - g. Scatter plots of 2.828-3.041 μm (OH corrected) and 3914 Å-band zenith intensities for seven data flights of the 1976 and 1977 series. The straight lines are uniformly-weighted least-squares fits of the SWIR intensities using measured hydroxyl-band ratios. These results are summarized in Column 12 of Table 3 .

Figure 2b. 2.94μm — OH Corrected, kR vs. 3914Å, kR

IC-76-09 07 Mar 76			
TIME (UT)	0922-0928	0950-1030	1134-1145
SYMBOL	•	x	o
SLOPE	3.32	3.22	3.39
INTERCEPT	-2.5	1.1	-6.0
CORRELATION COEFFICIENT	0.86	0.92	0.98
EFFICIENCY%	0.45±0.10	0.44±0.03	0.46±0.02

The graph axes and labels:
- Y-axis: 2.94μm — OH Corrected, kR (values: 0, 80, 160, 240)
- X-axis: 3914Å, kR (values: 40, 80), labeled 2c

Labels on graph: 0740–0845, 0850–0925

IC-76-10 08 Mar 76		
TIME (UT)	0740–0845	0850–0925
SYMBOL	•	x
SLOPE	3.34	3.48
INTERCEPT	7.7	-9.9
CORRELATION COEFFICIENT	0.98	0.94
EFFICIENCY%	0.46±0.02	0.47±0.05

2.94μm — OH Corrected, kR (vertical axis; values 240, 160, 80, 0)

3914Å, kR (horizontal axis; values 40, 80)

1013-1055

1120-1159

0906-0931

IC-76-16 26 Mar 76			
TIME (UT)	0906-0931	1013-1055	1120-1159
SYMBOL	•	x	o
SLOPE	3.36	4.85	3.70
INTERCEPT	17.4	11.9	-6.9
CORRELATION COEFFICIENT	0.88	0.94	0.97
EFFICIENCY%	0.46±0.04	0.66±0.03	0.50±0.02

Figure showing correlation plot of 2.94 μm — OH Corrected, kR (y-axis) versus 3914 Å, kR (x-axis).

#720 11 Sept 77			
TIME (UT)	0436-0529	0820-0856	0911-0925
SYMBOL	•	x	o
SLOPE	4.10	3.15	2.58
INTERCEPT	-2.1	-6.8	8.7
CORRELATION COEFFICIENT	0.81	0.73	0.88
EFFICIENCY %	0.56 ± 0.06	0.43 ± 0.06	0.35 ± 0.04

80

60

2.94μm — OH Corrected, kR

40

20

0

20

40

60

3914Å, kR

2

#724 15 Sept 77	
TIME (UT)	0905-1000
SYMBOL	•
SLOPE	1.34
INTERCEPT	14.0
CORRELATION COEFFICIENT	0.58
EFFICIENCY	0.18 ± 0.04

#725 16 Sept 77	
TIME (UT)	0945-1005
SYMBOL	•
SLOPE	2.80
INTERCEPT	15.1
CORRELATION COEFFICIENT	0.84
EFFICIENCY %	0.38 ± 0.05

2.94μm — OH Corrected, kR

3914Å, kR

2g

regression line are then as usual determined by minimizing the sum of the squares of the ordinate (vertical) deviations between each data point and the test line (Ref 11, p 10), applying each statistical weighting. With uniform and proportional-to-y weighting the equations describing the slopes are

$$\frac{n\Sigma xy - \Sigma x\Sigma y}{n\Sigma x^2 - (\Sigma x)^2} \quad \text{and} \quad \frac{\Sigma y\ \Sigma xy^2 - \Sigma xy\ \Sigma y^2}{\Sigma y\ \Sigma x^2 y - (\Sigma xy)^2} \quad ,$$

where n is the number of data points. The corresponding equations for intercept on the y axis are

$$n^{-1}\ (\Sigma y - (\text{slope})\ \Sigma x) \quad \text{and} \quad (\Sigma y)^{-1}\ (\Sigma y^2 - (\text{slope})\ \Sigma xy) \quad .$$

Symmetric 90% confidence levels on these slopes were determined following the procedure on p 22ff, Ref 11. The choice of P% means that if the chemiluminescence measurements were repeated under the same geophysical and experiment conditions with the same values of x (that is, with an identical energy-input distribution) the probability of arriving at a slope that is included in the interval defined by the limits would be 0.01P. Higher/lower confidence limits increase/decrease the range of values in which the photon emission ratio may lie. The expression for limits on the slope is

$$\pm\ \text{limits} = t_{(n-2)} \cdot \frac{\sqrt{\overline{\Sigma(y - y')^2}}}{\sqrt{(n-2)\cdot[\Sigma x^2 - \frac{(\Sigma x)^2}{n}]}} \quad ,$$

where y' is the ordinate on the best-fit line and $t_{(n-2)}$ is given in tables of Student's distribution (p 240 of Ref 11, for example). Important assumptions implicit in assigning confidence limits are 1) that the y's at each value of x are normally distributed about a mean; and 2) that their variances a) are the same for all x with uniform weighting or b) decrease as y increases with proportional weighting.

The correlation coefficient r is a semiquantitative measure of the predictability of SWIR column emission rate for known air-

25

fluorescent intensity. r, defined as

$$\frac{n \Sigma xy - \Sigma x \Sigma y}{\sqrt{[n \Sigma x^2 - (\Sigma x)^2] [n \Sigma y^2 - (\Sigma y)^2]}}$$

for uniform weighting, can have values between -1 and +1, with ±1
representing direct correlation (y is known exactly for any x).

RESULTS AND PRELIMINARY DISCUSSION

Eight of the aircraft missions encountered sufficiently intense
and persisting natural particle precipitation to allow assignment of
meaningful confidence limits to the statiscally-averaged SWIR/visible
radiance ratios. Further quantitative information is available from
short segments of another flight, and in addition chemiluminous yields
of lower precision can be derived from two of the earlier flights; these
data will be treated separately.

The zenith radiances measured in seven 1976-77 missions were
read manually from 3x photographic enlargements of computer plots
similar to Fig 1, at 15 sec intervals without smoothing or favoring of
peak values resulting from auroral arcs. (Data for IC-76-10 were
received on a time scale so compressed that the minimum effective
sampling interval was 60 sec.) Radiances of the segment of hydroxyl
overtone measured by the 1.623-1.739μm (FWHM) radiometer were re-
duced by 0.2 kR/kR 3914 Å to subtract out prompt air fluorescence in
this wavelength band, a correction that has only a small effect on the
results. Fig's 2a-g show the visible-infrared cross-plots and list the
best-fit slope with uniform weighting of the data points, the intercept
of the regression line (one measure of the effectiveness of OH back-
ground correction), and the correlation coefficient of each sample.

Fig's 2a - g also give the chemiluminous efficiencies derived from
these slopes for the complete $\Delta v = 2$ sequence of NO, which is assumed
to be the sole component of the fluorescence-associated SWIR emission.
The calculation applies the assumptions about nitric oxide vibrational
radiation processes stated in Ref 2, with the spectral distribution
changed to conform to that recently derived from laboratory measure-
ments (by COCHISE, Ref 10). This distribution results from the

26

reaction of N^2D with O_2 (only), and therefore the absolute SWIR-photon yields would be different from these quoted if $NO^{\dagger}$ ($v \geqslant 2$) is also excited by other mechanisms. It also applies the OH $\Delta v = 1/\Delta v = 2$ intensity ratios measured in each flight at times when the particle-energy inputs were weak (< IBC I aurora). The uncertainties listed in Fig's 2a-g and Table 3 refer to 90% confidence limits for the statistically-determined straight-line fits, without consideration of possible systematic errors in the field data.

These yields are summarized in Column 12 of Table 3, along-side sets derived with the aforementioned proportional weighting (Column 13) and applying a "recalibration" of the SWIR radiometer as described below (Column 14). Earlier (unpublished) results with non-uniform sampling,thresholding and two corrections for hydroxyl are shown for comparison (in Columns 6-11), along with the mean OH zenith intensities measured for each of the twelve data segments (in Columns 3-5). Theoretical ratios of the in-band OH intensities (second foot-note in Table 3) were derived by the procedure in Ref 2 . Table 3 also includes the results of Ref 3 's reduction of data from the one 1975 flight under intense aurora, adjusted downward for the updated spectrum of NO overtone emission (56% of which lies within the radio-meter's FWHM); the radiances from this flight, received on a com-pressed time scale, were sampled at uniformly-spaced 150 sec intervals after some manual smoothing and thresholded at 2 kR 3914 $\overset{o}{A}$.

Some further data from short segments of three flights, which required correction for the overlying atmosphere's thermal emission and absorption, are summarized in Table 4 . For the 01 Mar 76 mission the SWIR radiometer's wavelength-sensitivity band was broadened to 2.48-3.04μm FWHM and its field narrowed to 5° circular, and in the 1975 flights the lower half-response point was at 2.75μm (Table 2). Since the thermal component below ~2.85μm prevented use of hydroxyl-intensity ratios, SWIR backgrounds in these data were determined by visual averaging. Absolute chemiluminous yields were calculated directly from 12 photon ratios in isolated arcs and a single weak, broad glow (4 kR 3914 $\overset{o}{A}$, ~constant over 12 min flight time) in the 1976 flight. The relative response of the radiometer to the NO

27

Table 3. NO vibrational overtone energy efficiencies derived for selected measurement periods during the 1975, 76 and 77 data flights of NKC-53120.

1	2	3	4	5	6	7	8	9	10	11	12	13	14
		OH Δv = 1&2 Backgrounds, kR	OH Δv=1 / OH Δv=2 = M		SWIR Photons / 3914 Å Photon***		Intercept, kR***		Chemiluminous Efficiency*(%)		Chemiluminous Efficiency†† (%)		
Mission Date	Time UT				Using T	Using M	Using T	Using M	Using T	Using M	Uniform†	Proportional†††	Recalibrated+
IC-75-4 10 Mar 75	0805-0930 } 1120-1215 } 0930-1120	40 40			3.02 4.03		Probably thermal emission (Ref 2) 158 95	12.3	0.45 ± 0.09 r=0.80 0.60 ± 0.12 r=0.88		0.45 ± 0.09 0.60 ± 0.12	} 150 sec sampling, manual smoothing	
IC-76-6 03 Mar 76	0500-0528	110	65	1.7	2.50	2.57	-14.3	12.3	0.34 ± 0.03	0.35 ± 0.03	0.46 ± 0.02	0.41 ± 0.02	0.42
IC-76-9 07 Mar 76	0922-0928 0950-1030 1134-1145	120 105 110	70 62 69	1.7 1.7 1.6	2.88 3.45 3.36	2.52 3.45 3.30	-12.3 -23.9 -39.6	12.7 -0.8 -4.1	0.39 ± 0.25 0.47 ± 0.07 0.46 ± 0.03	0.35 ± 0.26 0.47 ± 0.07 0.45 ± 0.03	0.45 ± 0.10 0.44 ± 0.03 0.46 ± 0.02	0.33 ± 0.09 0.47 ± 0.02 0.46 ± 0.02	0.38 0.42 0.42
IC-76-10 08 Mar 76	0740-0845 0850-0925	102 102	60 60	1.7 1.7	3.32 2.97	3.38 2.94	-19.4 -26.3	8.6 1.7	0.46 ± 0.03 0.41 ± 0.05	0.46 ± 0.05 0.40 ± 0.05	0.46 ± 0.02++ 0.47 ± 0.05++	0.43 ± 0.02++ 0.41 ± 0.03++	0.45 0.46
IC-76-16 26 Mar 76	0906-0931 1013-1055 1120-1159	160 156 165	76 74 78	2.1 2.1 2.1	2.93 4.51 3.56	2.93 4.51 3.56	14.4 16.4 7.1	14.4 16.4 7.1	0.40 ± 0.11 0.62 ± 0.06 0.49 ± 0.05	0.40 ± 0.11 0.62 ± 0.06 0.49 ± 0.05	0.46 ± 0.04 0.66 ± 0.03 0.50 ± 0.02+++ (0.50 ± 0.02)	0.42 ± 0.04 0.63 ± 0.02 0.46 ± 0.02+++	0.29 0.42 0.28
720 11 Sep 77	0436-0529 } 0820-0856 } 0911-0925	84	99	0.85	0.36 3.68 3.23	2.37 3.24 3.17	-115.0 -173.5 -114.6	-1.8 -15.7 5.2	0.05 ± 0.62 0.50 ± 0.18 0.44 ± 0.08	0.32 ± 0.49 0.44 ± 0.15 0.43 ± 0.06	0.56 ± 0.06 0.43 ± 0.06 0.35 ± 0.04+++ (0.40 ± 0.02)	0.53 ± 0.05 0.33 ± 0.05 0.33 ± 0.05	0.67 0.52 0.42
724 15 Sep 77	0905-1000	25	70	0.36	2.34	1.54	-179.5	11.6	0.32 ± 0.09	0.21 ± 0.06	0.18 ± 0.04	0.16 ± 0.03	0.72
725 16 Sep 77	0945-1005	30	85	0.35	2.50	2.17	-116.0	19.8	0.34 ± 0.08	0.30 ± 0.08	0.38 ± 0.05	0.35 ± 0.03	1.27

* Average measured under < IBC I power-input conditions during the flight or segment

** M = measured. Theoretical ratio T = 2.1 in 1977-76, 1.3 in the 1975 flight

*** Slope and intercept at 0 kR 3914 Å, determined from best-fit as described in text

† Previous non-uniform sampling of radiance data: ~ 1/2 - 1 min intervals; uniform weighting above a 5-10kR 3914Å threshold

†† Systematic data sampling at uniform 15 sec intervals: uses observed OH ratio M

††† Data points weighted uniformly, and given statistical weight proportional to the SWIR intensity

+ Data points weighted uniformly, and efficiencies normalized to an OH Δv = 1 level of 100 kR

++ Data sampled at 1 min. intervals. IC-76-10 only

+++ All data points included in the fit: r=0.90 for 76-16, 0.87 for 720

28

Table 4. NO vibrational energy efficiencies indicated by additional[†] measurement periods in the 1975 and 1976 flight series

Time UT	3914 Å, kR	2.8μm, kR[*]	$\boxed{\dfrac{2.8\mu m}{3914\,\text{Å}}}$	Chemiluminous Efficiency (%)[†]
01 Mar 76 (IC-76-5)				
-30 sec	17	79	$4\frac{1}{2}$	0.38 ± 0.04
0945[**]	34	196	6	0.51 ± 0.04
+30 sec	18	148	8	0.68 ± 0.06
[0947 - 0959][**]	4	42	$10\frac{1}{2}$	0.9 $\substack{+\ 0.3 \\ -\ 0.4}$
-30 sec	13	70	$5\frac{1}{2}$	0.47 ± 0.12
1030	20	110	$5\frac{1}{2}$	0.47 ± 0.12
+30 sec	16	80	5	0.42 ± 0.10
-30 sec	29	130	$4\frac{1}{2}$	0.38 ± 0.07
1050	56	220	4	0.33 ± 0.05
+33 sec	33	136	4	0.33 ± 0.07
1053	9	60	$6\frac{1}{2}$	0.55 ± 0.15
1056	12	50	4	0.34 ± 0.20
All above data points averaged as described in text				0.31 ± 0.08[++]
02 Mar 75 (IC-75-2)				
[0825 - 0845]	4	$19\frac{1}{2}$	5	0.75 ± 0.35
[0920 - 0943]	6	23	4	0.60 ± 0.25
[0943 - 0956]	5	18	$3\frac{1}{2}$	0.53 ± 0.20
11 Mar 75 (IC-75-5)				
[0800 - 0820]	$18\frac{1}{2}$	49	$2\frac{1}{2}$	0.38 ± 0.20

[*]Background subtracted: 265 kR 0945 - 0959, 250 kR 1030 - 1056

[**]Bracketed values average over period; others refer to isolated peaks

[†]Error estimate considering only reading inaccuracy, probably lower limits to actual error; refer to text

[++]90% confidence limit on slope, uniform weighting. Intercept on SWIR axis is 30 kR; if regression line is forced to go through the origin, the efficiency becomes 0.39 ± 0.09%

[†]Not included in Table 3

vibrational overtone was determined to be 0.89 by planimetry of the spectrum provided by AFGL (Ref 10) and an effective weighted atmosphere transmission of 0.84 was derived from the argument that 0.75 of the NO radiation between 2.48 and 2.86μm is transmitted to the aircraft (calculated line-by-line, Ref 2) and attenuation at wavelengths above 2.86μm is small enough to be neglected. Yields from brief data segments in the two 1975 flights (final four entries in Table 4) were calculated by the procedure applied to the 10 Mar 75 missions in Ref 3; the SWIR background subtracted was again determined by interpolation.

The error estimates assigned to the data points in Table 4 consider only the expected uncertainties in the hydroxyl-plus-thermal background and in reading radiances from the plots given in Ref 6. In view of the fact that unsystematic treatment of limited data segments and "correlated peaks" from the other aircraft flights leads to a similarly large scatter in apparent chemiluminous yield – refer to Table 5 of Ref 6, and to Table 3 – these estimates are most probably lower limits to the actual uncertainty in each data point. The final line entry for the 02 Mar 76 flight in Table 4 is the result of a uniformly-weighted least-squares straight line fit to the twelve preceding data points (with 90% confidence limit uncertainty). Failure of the regression line to pass through the origin, along with a "statistical" chemiluminous yield lower than those derived from simple radiance ratios, is most likely due to the inherent uncertainty in SWIR background (note that the data in Fig 18 of Ref 6 indicate different baselines over successive time intervals). When the regression line is forced through the origin the averaged chemiluminous yield (0.39 ± 0.09)% falls within the range for the other 1976 flight missions.

Returning to Table 3, we note that results for eight of nine segments of the four 1976 flights are largely self-consistent, the exception being those from the period 1013-1055 on 26 Mar (refer also to Fig 2d). The reduced data from the 1975 radiometer, which (as described in Ref 3) apply to a breakup between 0930 and 1120 and

more or less isolated arcs at other times, may be considered consistent with those from 1976. Chemiluminous yields derived from the 1977 flight data, on the other hand, vary among themselves by as much as a factor three. (The lowest value results from a data set with correlation coefficient 0.58 (Fig 2f), in comparison to the 0.86 - 0.98 range of the 1976 data and 0.73 - 0.88 of the other 1977 data.)

This variability is accompanied by somewhat anomalous hydroxyl airglow backgrounds, as is indicated in Table 3 and plotted in Fig 3 for the six flights of the series. The weak OH $\Delta v = 1$ signal results in fundamental/overtone ratios considerably smaller than predicted from theory, even assuming no mechanism favoring excitation of OH in the low vibrational states that produce the bands to which the SWIR radiometer is sensitive (its response is discussed in Appendix I). As Fig 3 shows, the large decrease after 11 Sep 77 in measured fundamental-band radiance is not correlated with local magnetic activity. (Appendix III of Ref 3 shows an increase of mean hydroxyl-overtone intensity with the sum of the local K-indexes in the period 12-24 hr before the 1975 flight missions (Fig III-9), and reviews other evidence for dependence of the OH intensity and rotational temperature on geomagnetic storm activity.) Additionally, the other major intermediate-period geophysical influence on the natural hydroxyl airglow, stratospheric warmings, increase rather than decrease its column intensity (Fig's III-6 and III-7 of Ref 3).

An alternative hypothesis is that the SWIR radiometer's response was changing during the 1977 measurement series. Correction for such a change by normalizing the radiance increases associated with air fluorescence to a zenith hydroxyl background of 100 kR (in the radiometer's sensitivity band) gives the chemiluminous yields in Column 14 of Table 3 . This procedure appears to overcorrect the measured yields, and in any case decreases the self-consistency of the flight data.

31
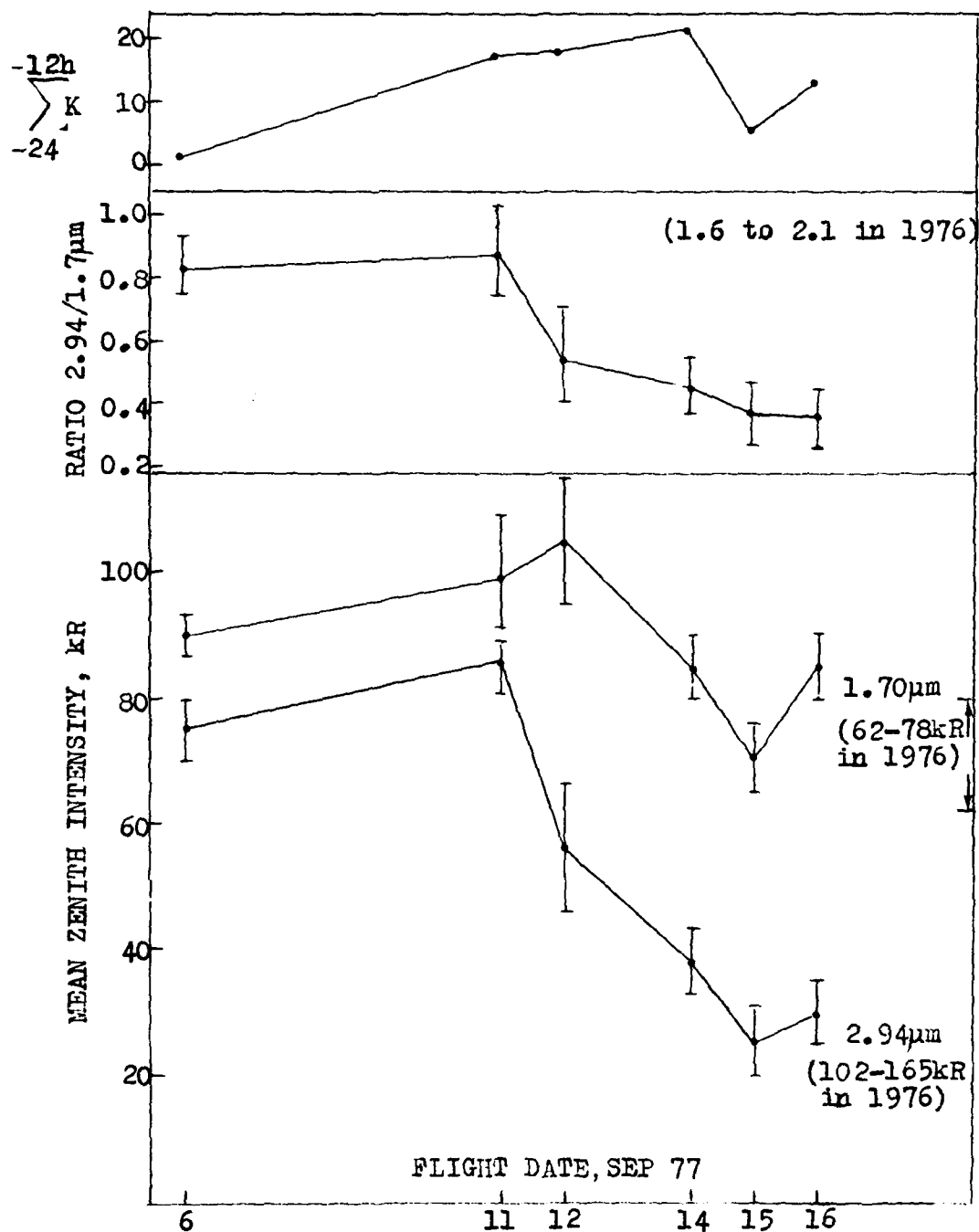
Figure 3 . Mean measured OH Meinel-band intensities in the six
1977 data flights, and sums of the 3-hour Fairbanks
K-indexes in the period 12-24 hours before flight.

IC76-06   03Mar76
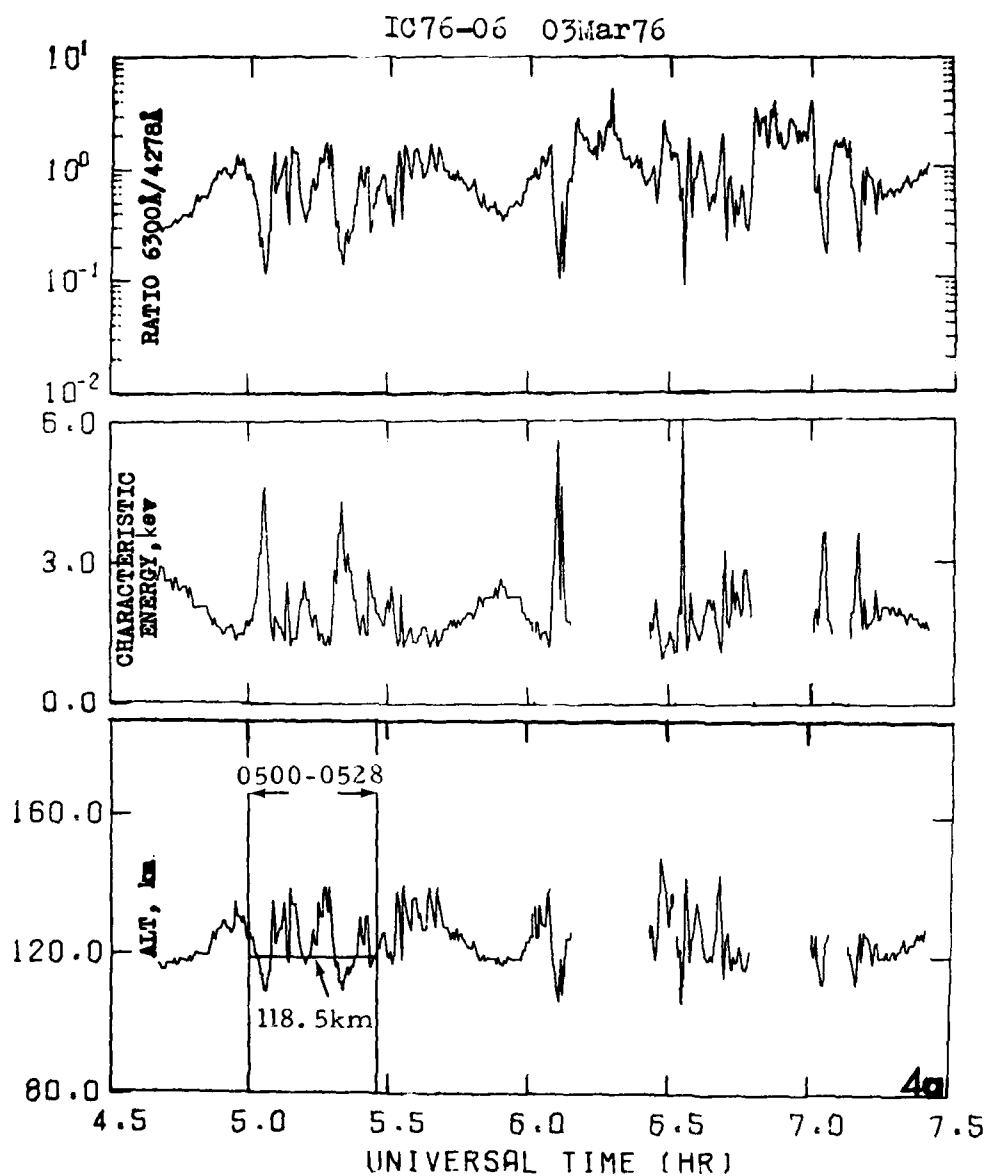
Figure 4a - g.   Plots of 6300 Å/4278 Å photon ratio, characteristic
energy of incoming electron flux, and altitude of peak
energy deposition for the seven 1976-77 data flights in
Fig 2a - g and Table 3. The altitudes indicated are
averages over the time intervals of the scatter plots.

33

IC76-09 07Mar76

4b
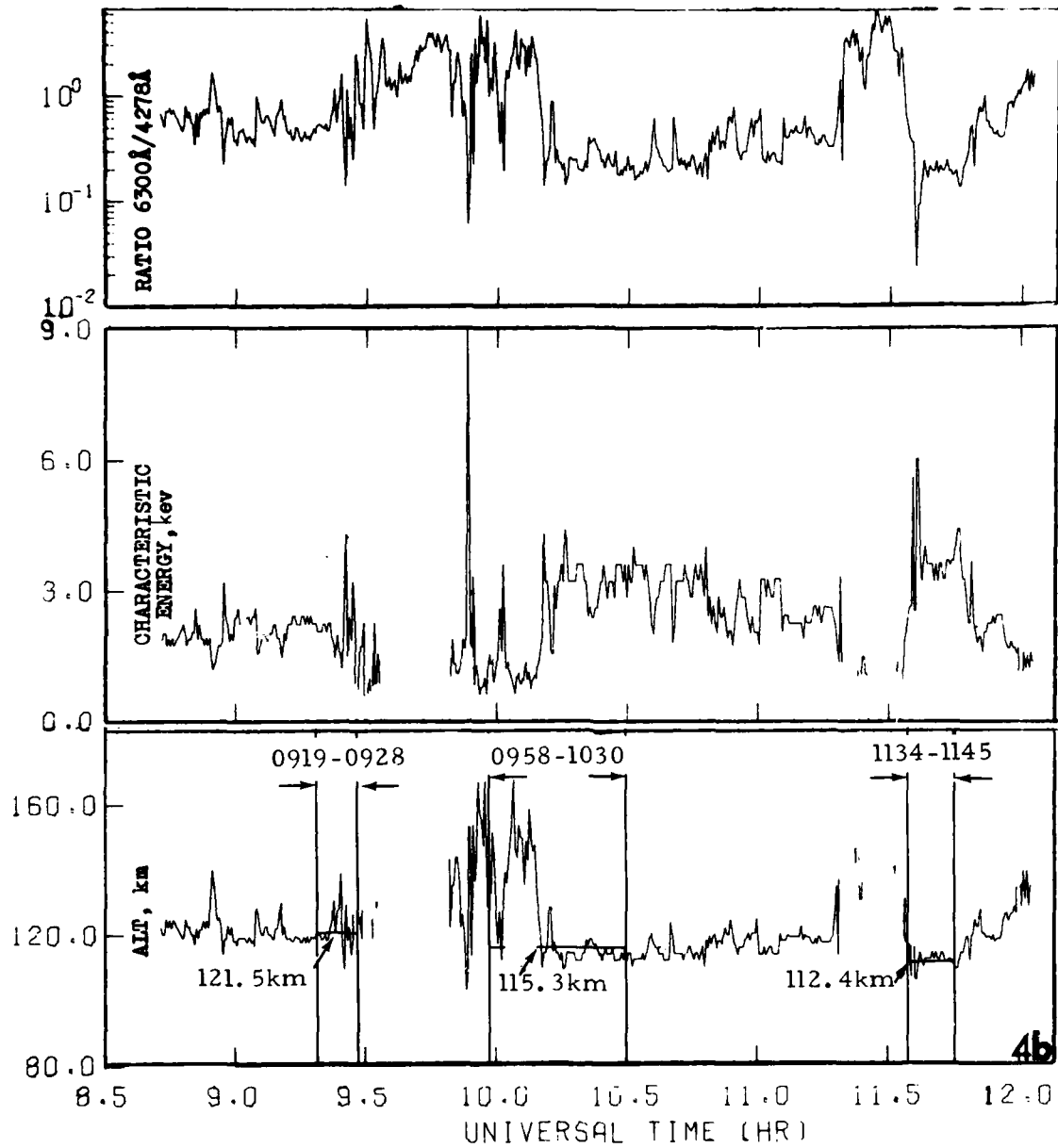
IC76-10   08Mar76
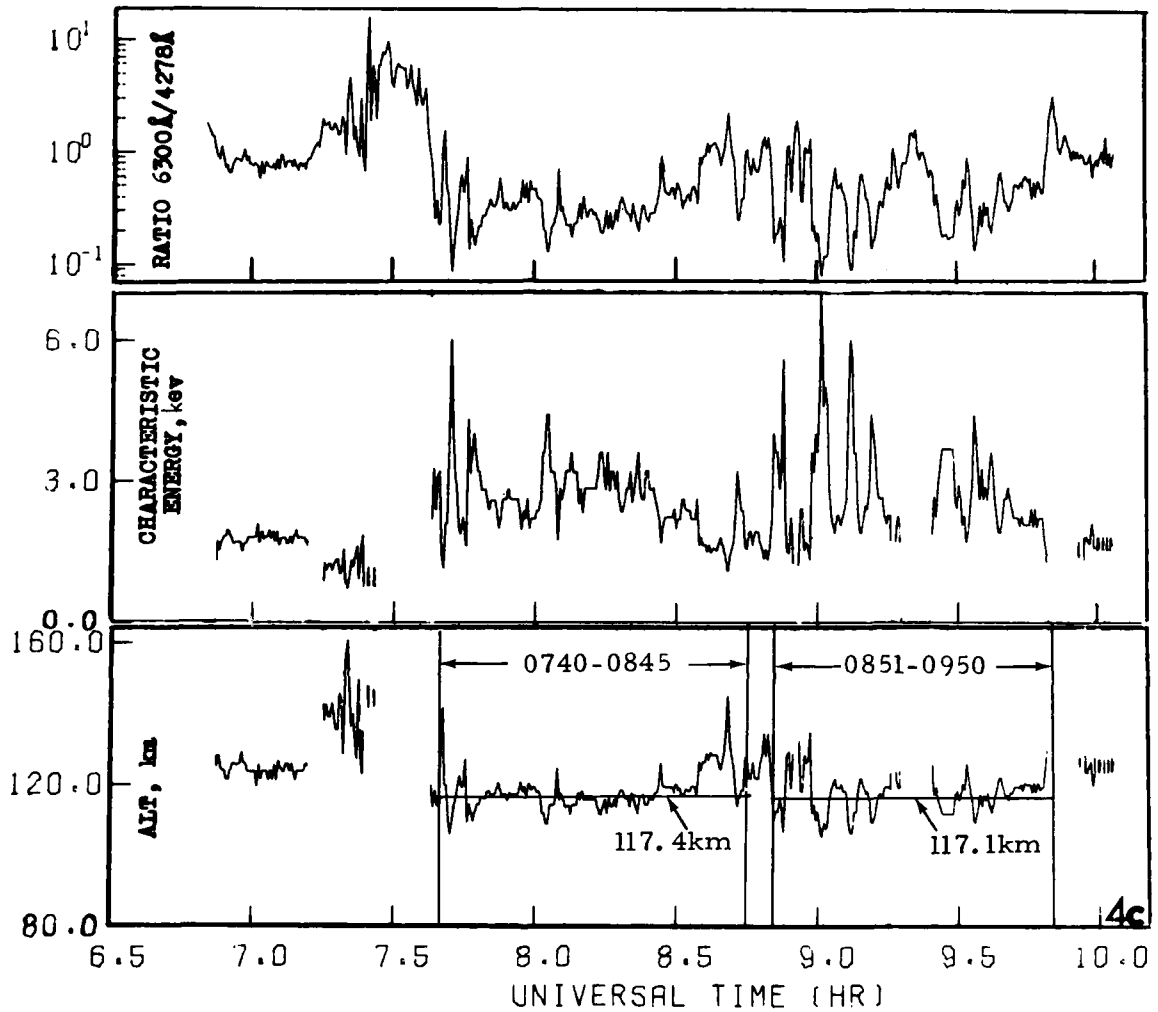
IC76-16 26Mar76

#720 11Sept77

RATIO 6200X 4278X

CHARACTERISTIC ENERGY, keV

ALT, km

0911-0925

126.0km

0820-0856

134.5km

0436-0529

127.5km

UNIVERSAL TIME (HR)

4e

#724 15sept77

0905-1000
121.0km

UNIVERSAL TIME (HR)

RATIO 6300Å/4278Å
CHARACTERISTIC ENERGY, kev
ALT, km

38
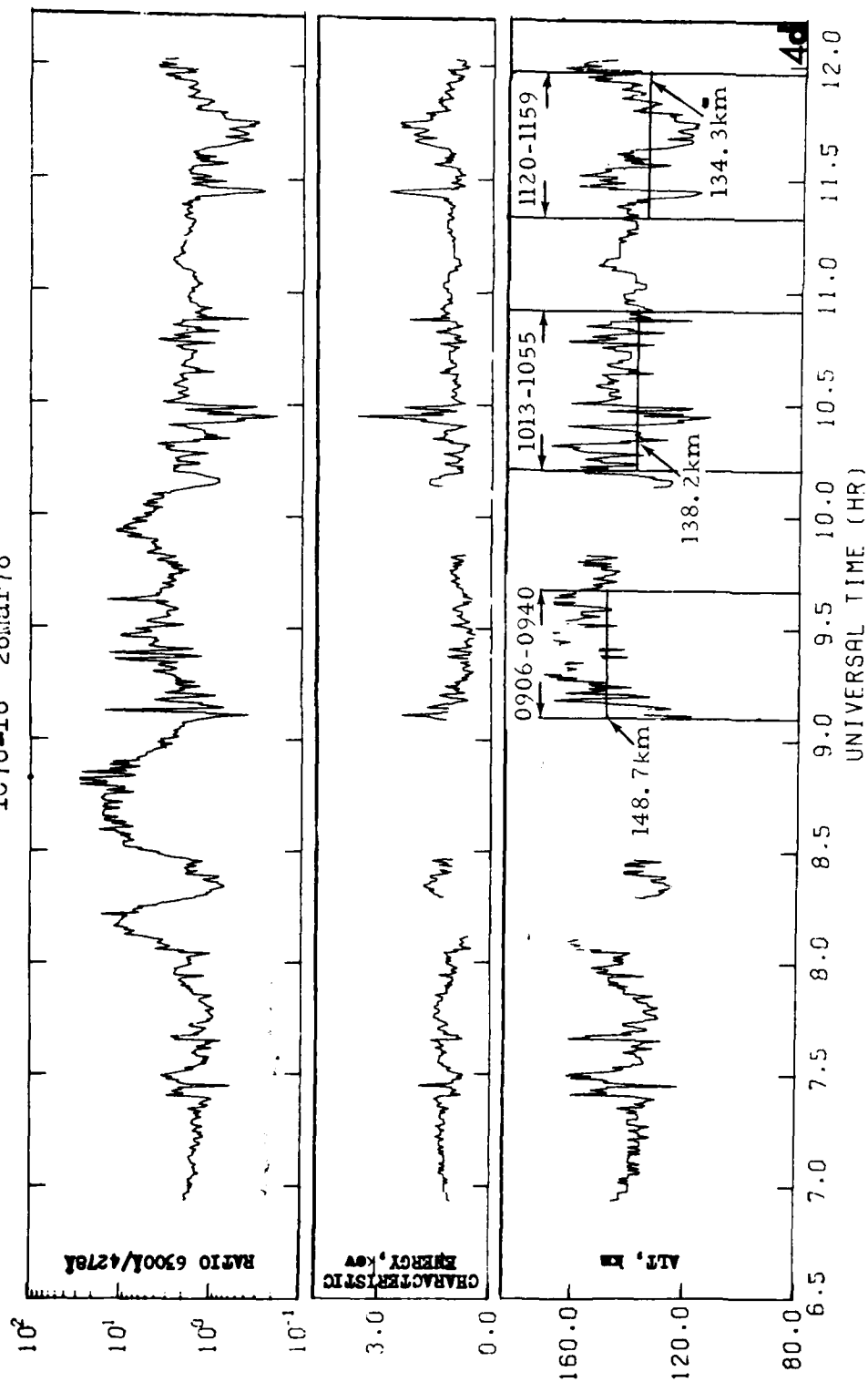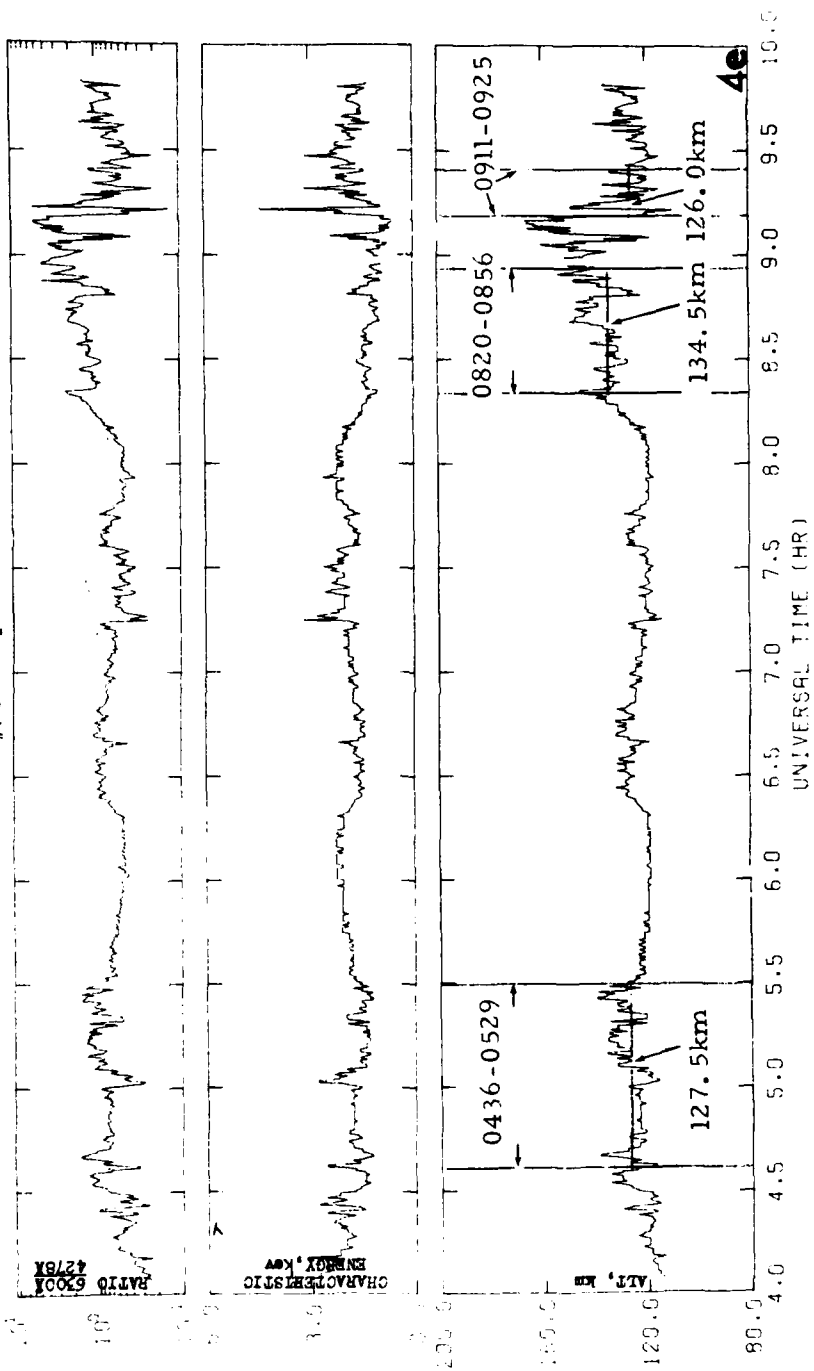
#725 16Sept77
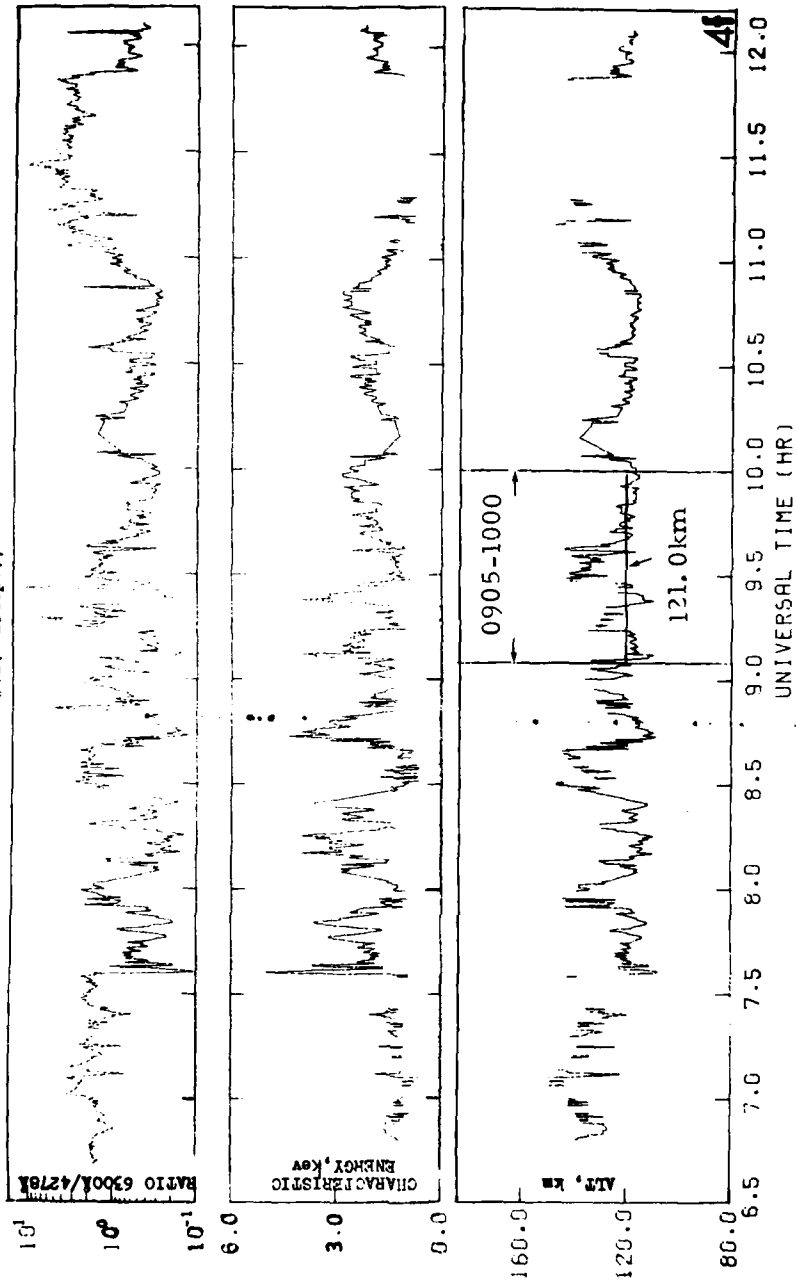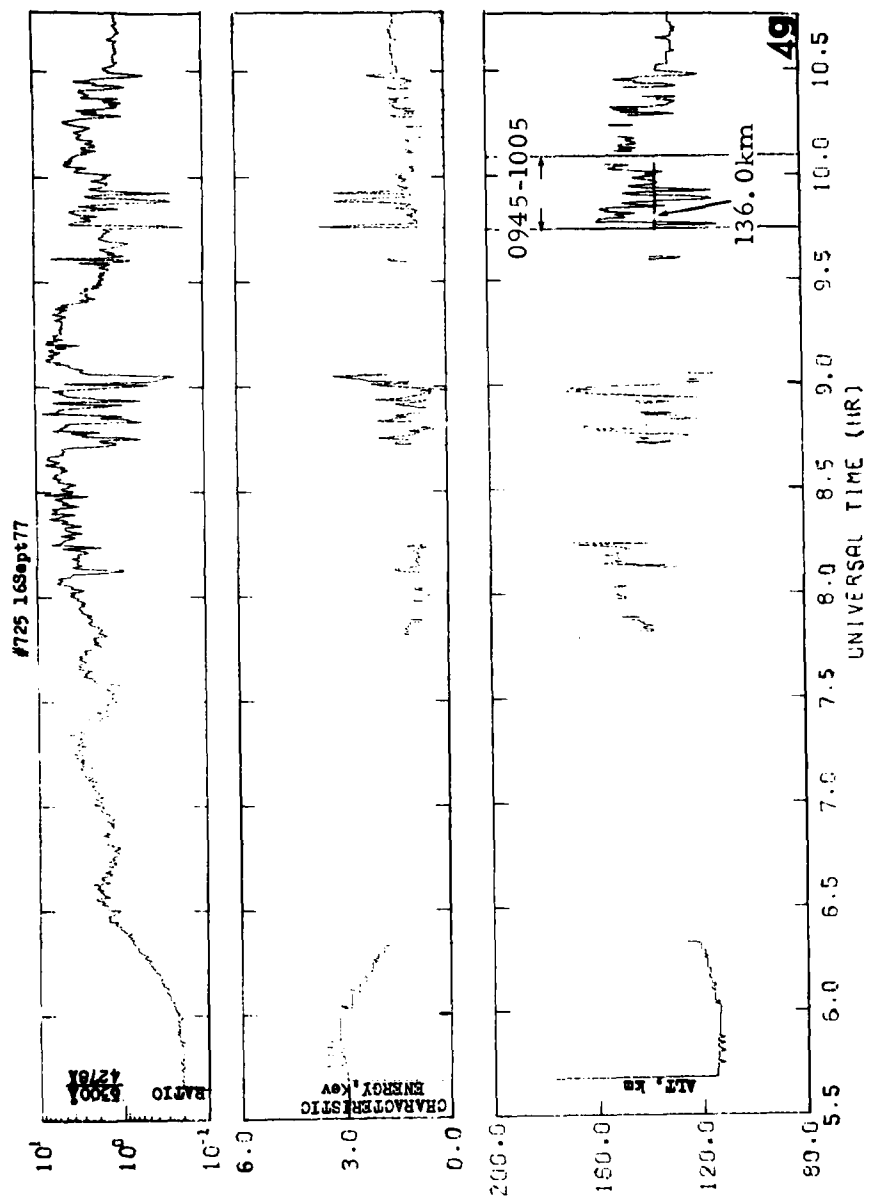
The altitudes at which the energy deposition rate is a maximum, calculated as described in Appendix II of Ref 3, are plotted for the seven 1976-77 flights in Fig's 4a-g. A very preliminary comparison of the mean peak deposition altitudes during the data segments with the chemiluminous efficiencies derived from the regression lines shows no obvious trends. Not enough energy deposition profiles are as yet available from the DNA 617 incoherent scatter radar to permit comparison with the measured yields (data including only the IC-76-6 and - 10 flight periods have been reduced).

SUMMARY AND RECOMMENDATIONS

Results from uniform application of explicitly described procedures for deriving SWIR-chemiluminous yields in energetic particle-irradiated air from the aircraft data base are summarized in the last three columns of Table 3. The uncertainties quoted refer to the statistical precision of slopes of regression lines – they are 90% confidence limits, perhaps somewhat low because the original traces are probably oversampled –, and make no direct statement about the accuracy of the experiment as a whole or of measurements of infrared and air-fluorescent radiance made in individual flight segments. The errors bars assigned in Table 4 to the less reliable (albeit generally confirmatory) data from three flights across limited regions of particle precipitation are estimated from the uncertainties in reading and interpreting the data provided, and again are not intended to comment on absolute experiment accuracy.

Treating the data in a standard way has the effect of lessening the segment-to-segment variability of SWIR chemiluminous efficiency. Variations from a mean outside a generally-accepted confidence level remain, however, particularly in the 1977 data sets that exhibit low coefficients of correlation (in effect, large scatter about the best-fit photon ratio straight-line). Nonlinearity of infrared output with energy input is not detectable at any reasonable level of significance in the individual cross-plots; all the data from the 1976 flights in

40

Table 3 are now being lumped together in a further search for curvature. The lack of detectable variation of chemiluminous yield with altitude of peak energy deposition as measured by the spectroscopic-ratios method (at least in a preliminary comparison with both quantities averaged over relatively long times) may be an effect of the broad minimum in $NO^{\dagger}$ radiation probability near 100 km. Such a minimum was observed in an arc by a HAES-program sidelooking rocket radiometer (Section II of Ref 3) and is predicted from laboratory results on collisional quenching (in Ref 12). (Further energy-input profiles (refer to Table 8 of Ref 3) are forthcoming from the Chatanika radar.) The altitude profiles of input and relative SWIR yield are now being multiplied and summed to determine the sensitivity of vertical column-integrated emission to the precipitating particles' characteristic energy parameter (α in Section II).

The question of the extent to which the variation in SWIR yield inferred here from the 1977 data is a real physical effect or an artefact of instrument response (or other experiment variable) can best be answered by 1) an investigation of the radiometer system's performance in the 1977 flight series, and 2) a review of available supporting data on the hydroxyl intensity-vibrational distribution and rotational temperature in the high-latitude region traversed, presence of thin high-altitude clouds, and other geophysical parameters that might influence SWIR radiances measured in the aircraft's zenith. (An internal calibration source, such as used in the AFGL/DNA rocket instruments, serves to check on the stability of the radiometer, but not the condition of its chopper and window.) Further information on this critical issue is expected from the data taken in Aug 78 flights of the wide-field instruments, and of course from the greatly-improved SWIR radiometry planned for Spring 1979 (Appendix I).

SECTION 2

ENERGY INPUT IN HIRIS II's FIELD

BACKGROUND

The pointing of the cryocooled interferometric spectrometer carried on HAES rocket IC630.02-1A (HIRIS II, 01 Apr 76; the instrument's design is documented in Ref 13) is reviewed in Section V of Ref 4 . The spectrometer's 2°-circular field of view in effect described a cone with apex angle 165°, whose axis pointed at 9° elevation-130° geomagnetic azimuth (Fig's 31-33 of Ref 4). 25.4 double-sided interferograms were compiled during each of six 34.5-sec rotations. Ref 4 also showed, in a semiquantitative way, how the tumbling field intercepted the precipitating particle-excited air to the S and N of the rocket's trajectory (Fig 34 is an example); and listed some times at which optical aurora − qualitatively described by the All-Sky camera projections, Fig 58 of Ref 3 − and/or thermal infrared radiation from the nadir atmosphere lay in the field (Table 5).

The first 22 spectral scans record emission from the instrument cover, an in-flight calibration source, and/or the lower hemisphere. Rotation 1 is defined (Table 4 of Ref 4) as starting with scan 23, which began at 100.9 sec after launch when the rocket's altitude was 96.3 km and the field orientation was 0.0° eℓ-36.9° geomagnetic az. When the instrument is pointing near the horizon its elevation angle increases or decreases by about 15° in a 1.36-sec interferogram cycle. This change in elevation results in a substantial range of intercept altitudes on, and thus of column excitation rates in, distant regions of energetic-particle precipitation. In this Section we calculate, from groundbased photometry data, the instantaneous rates and time-integrated energy inputs for three interferometer scans of particular interest.

ENERGY-INPUT CONDITIONS

As has been previously described in Ref's 4 , 14, and 15, the spatial distribution of particle energy input near Poker Range changed rapidly during upleg and somewhat more slowly during downleg of the rocket's trajectory. The 3914 $\overset{o}{A}$-band radiance in the rocket's zenith was ~ 50 kR up to near the time data-taking began, and then fell to less than 20 kR through the measurement period as the main region of particle precipitation moved rapidly southward. The power input within the interferometer's field was a maximum when it pointed at low elevation angles toward series of auroral arcs that lay to the N and S (the $\sim$NE-SW "scan direction" resulting from the rocket's coning places these arcs in the field). For example about halfway through the first rocket rotation, in scan 34 starting at 106 km altitude, the west limb of the intense (50-75 kR 3914 $\overset{o}{A}$ projected to the PKR meridian-scanning photometers) discrete arc then just S of PKR comes into the field of view; the spectra in scans 34 and 35 show signal at wavelengths just above 5.3μm, and scan 35 (elevation angles below 11.7^{o}) also shows the expected CO_2 and O_3 atmospheric-emission bands.

Preliminary efforts to predict which of the spectral scans would have the largest chemiluminescence component gave an indication, when the actual reduced interferograms became available, that the emission was more closely correlated with the "prompt" energy input than with predosing in the previous $\sim$1 min. The maximum signal/noise ratios in the NO vibrational-fundamental wavelength region between 5.3 and 5.8μm are at every limb-crossing found to be in that spectrum scan which adjoins the one showing onset (on downswing) or end (on upswing) of strong thermal-emission background. An example is scan 36, -3 to -17° elevation, in which this strong background causes the instrument system gain to decrease and completely dominates the spectrum. That is, the aurora-associated infrared enhancements are all at low elevation angles, where the van Rhijn radiance gain is large. In practice, scans with high "chemiluminescent" signal/noise ratios

are better identified by direct reference to the library of spectra than by calculating from earth-limb models the thermal background for the instrument's altitude and elevation angle(s).

A systematic review of these intensity-uncalibrated spectra shows the following general features of the signal in the NO $\Delta v = 1$ region. Little or no emission appears above the noise at instrument elevation angles above $\sim 30^{\circ}$, although further processing of the spectrum data may show signal to $\sim 50^{\circ}$ on downswing of Rotation 1 (scans 33 and 32), when the nearby arc to the S is in the instrument's field . Spectral intensities are higher when the interferometer points southwest $\sim 212^{\circ}$ geomagnetic from the rocket, than northeast, $\sim 37^{\circ}$; they are also higher on downleg than upleg. These observations are qualitatively consistent with what would be expected from the visible fluorescence distributions shown in the All-Sky projections. The maximum depression angle in the first scan in which thermal emission swamps chemiluminescence increases with rocket altitude, as would be expected. Above 120 km, chemiluminous emission still dominates radiation at elevations (at an end of the interferometer's scan) near $\sim -10^{\circ}$. On the other hand when the rocket altitude has fallen to between 84 and 68 km (Rotation 6, on downleg), no 5.3-5.8μm signal is discernible in the spectra at any elevation angle, and the intensities of 9.8μm O_3 and 15μm CO_2 bands are high even in the zenith direction.

In this regard, the 4.26μm CO_2 ν_3 band intensity is considerably higher on upleg than on downleg of the trajectory. On upleg it is strong at altitudes between 96.3 km (start of pointing into upper hemisphere) and 107.9 km (resumption of intense thermal emission from the lower hemisphere) and then missing in the spectrum scans above 116.1 km (instrument field again reaches 0° el, Rotation 2 begins). On the other hand the double-peaked CO_2 signal is not reliably detectable in downleg Rotation 5, 109 to 98 km, and it is missing in Rotation 6, 84 to 68 km. (Presumably the failure of the 4.26μm-band emission to be resolved in the spectra taken by the instrument when it was pointing

into the lower hemisphere and when it was at altitudes below ~84 km
is an artefact of the limited dynamic range of the interferograms,
which under these conditions are dominated by thermal emission between
~9 and 17μm.) A similar difference in intensity near 4.3μm with
latitude was observed by both the vertical-viewing (Ref 16) and side-
viewing (Section II , and Ref 3) spectroradiometers on HAES rocket
A18.219-1 (1974 multi), which has been interpreted as being caused
by a difference in predosing. Energy input in the ~5 min before
passage of HIRIS II was greater near upleg than downleg, which is
quantitatively consistent with the interferometer measurements. The
altitude profile of CO_2 radiation density will be reviewed in detail when
the reduced ν_3-band intensities become available.

This previous dosing, as noted above, did not have a similiar
effect on the 5.3-5.8μm chemiluminescence. The strongest signals
in the NO $\Delta v = 1$ spectral region are on downleg when the interferometer
is pointing at the instantaneously-most-intense optical aurora.

POWER AND ENERGY INPUT IN SCANS 125,137, and 24

The highest signal/noise ratios in the 5.3-5.8μm region appear
to be in the two limb spectra of Rotation 5. These were therefore
analyzed by the interferometer group, along with scan 24 of Rotation 1,
in which the spectral intensities were about an order of magnitude less.
The viewing geometry at the start/end of each 1.26 sec data scan (1.36 sec
minus 0.1 sec for mirror flyback) is outlined in Table 5 .

Table 5 . Geometry for spectral scans analyzed

	Scan 125 (Upswing 5)	Scan 137 (Downswing 5)	Scan 24 (Upswing 1)
Time, sec	238.5'239.8	254.7'256.0	102.2'103. 4
Rocket altitude, km	108.9'108.2	98.6'97.7	97.3'98.2
Elevation, deg	-6.2'+ 8.0	+15.2'+1.4	+14.1'+27.9
Azimuth, deg (geomagnetic)	40.3'37.0 (Northeast)	218.2'215.2 (Southwest)	34.9'32.9 (Northeast)

Figure 5. All-sky view from Poker Flat of the distribution of visible air fluorescence between 248 and 253 sec after launch of HIRIS II. Pointing of the USU elevation-scanning photometer, the Chatanika radar, and the projection of the field of view of the interferometric spectrometer during scans 125 and 137 is shown.

Fig 5, the all-sky projection of the optical aurora at PKR (90 km S and $12\frac{1}{2}$ km W of the rocket) between 248 and 253 sec, presents an overview of the spatial distribution of particle-energy input in the 238 - 256 sec period spanned by the two Rotation 5 scans. The distribution showed little change over this time, as evidenced by the three all-sky views between 224 and ~267 sec from PKR and from FYU (~90 km N of the rocket) in the HIRIS II photographic montage, Fig 58 of Ref 3. The corresponding view from FYU with a labeling of the areas of particle precipitation is in Fig 6. Fig 7, an exposure from FYU between 100 and 109 sec, gives similar information for scan 24. The dashed curved lines in Fig's 5, 6 and 7 are the projections of the interferometer's field onto these all-sky "maps," in which zenith angles are progressively more compressed toward the horizon. The usual caveats about interpretation of the projections of the three-dimensional scene onto the camera's 2-D image plane of course apply.

We have used these all-sky images, the narrow-angle meridian photometer scan data from PKR (Ref 17) and FYU, some input from the DNA 617 incoherent-scatter radar at Chatanika, and models of the altitude profiles and the atmosphere's scattering-extinction to provide best-estimates of the column energy deposition rates in the interferometer's field during (and before) these three interferometer scans. The (near-) meridian photometer operated at PKR by Utah State University scanned in elevation along azimuth 16° E of N $\rightleftharpoons$ 16°W of S, and the two operated by the University of Alaska Geophysical Institute as part of Poker Flat Research Range's support of rocket launches were as usual pointed in the geomagnetic meridian plane (as shown in Fig 5, which also gives the pointing directions of the Chatanika radar, and Fig 6).

Energy inputs were first calculated without considering out-scattering or in-scattering of 3914 $\overset{\circ}{A}$ or 4278 $\overset{\circ}{A}$ air-fluorescence photons by the lower atmosphere. These results were then corrected applying the principles outlined in Section V of Ref 3, as described below.

47
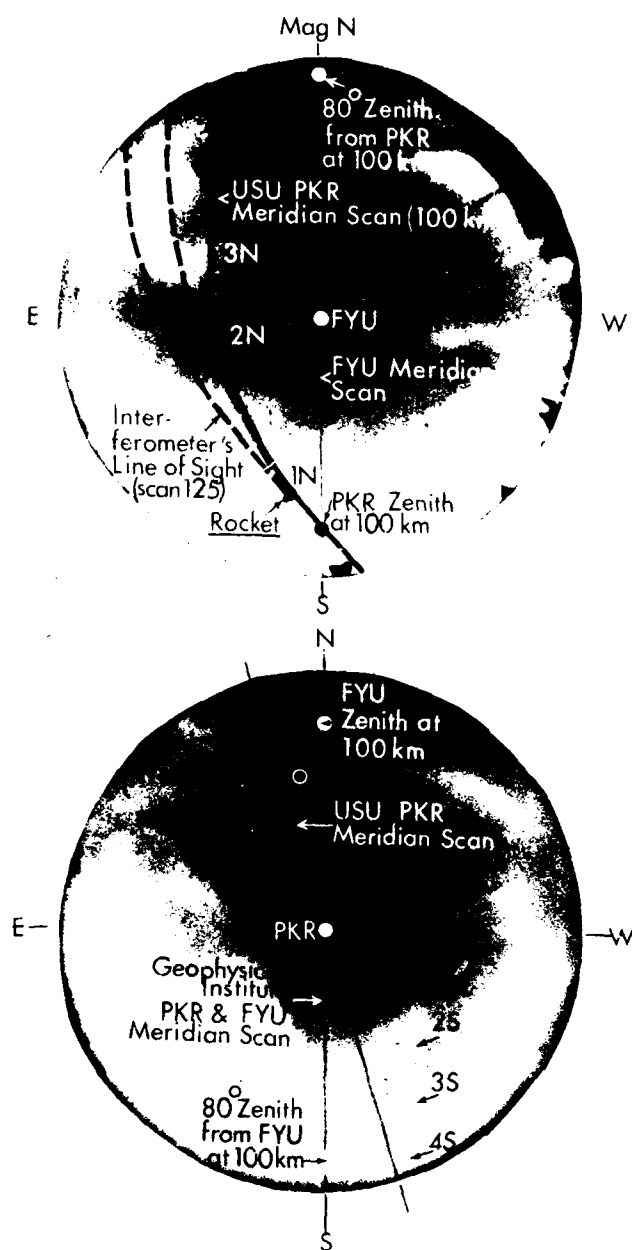
Figure 6. All-sky views from FYU (top) and PKR
(bottom, reproduced from Fig 5) near
250 sec after HIRIS II launch, with identi-
fication of the emitting regions. The top
view shows the intercept of the PKR-USU
near-meridian scanning photometer's
field on the 100-km altitude plane and the
projection of the interferometer's line of
sight to FYU.

48

W

True N

Mag
N

OFYU
Zenith

227.9°El 33'

1N

DNA
617
Radar
115 km

Rocket at 10?? sec
97.3 km

2N

141°El 35Az

Interferometer's
Line of Sight
Scan 24

E

S
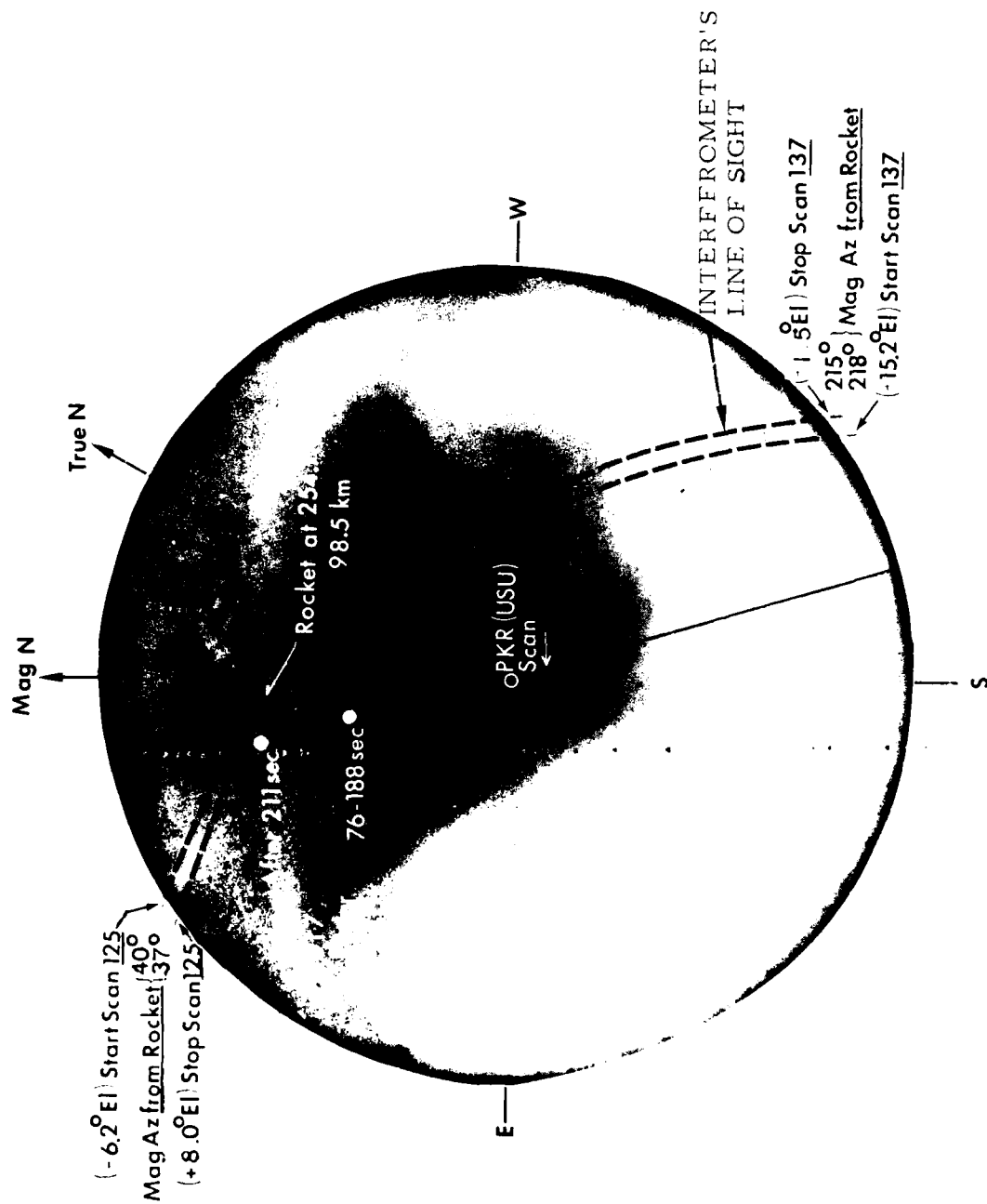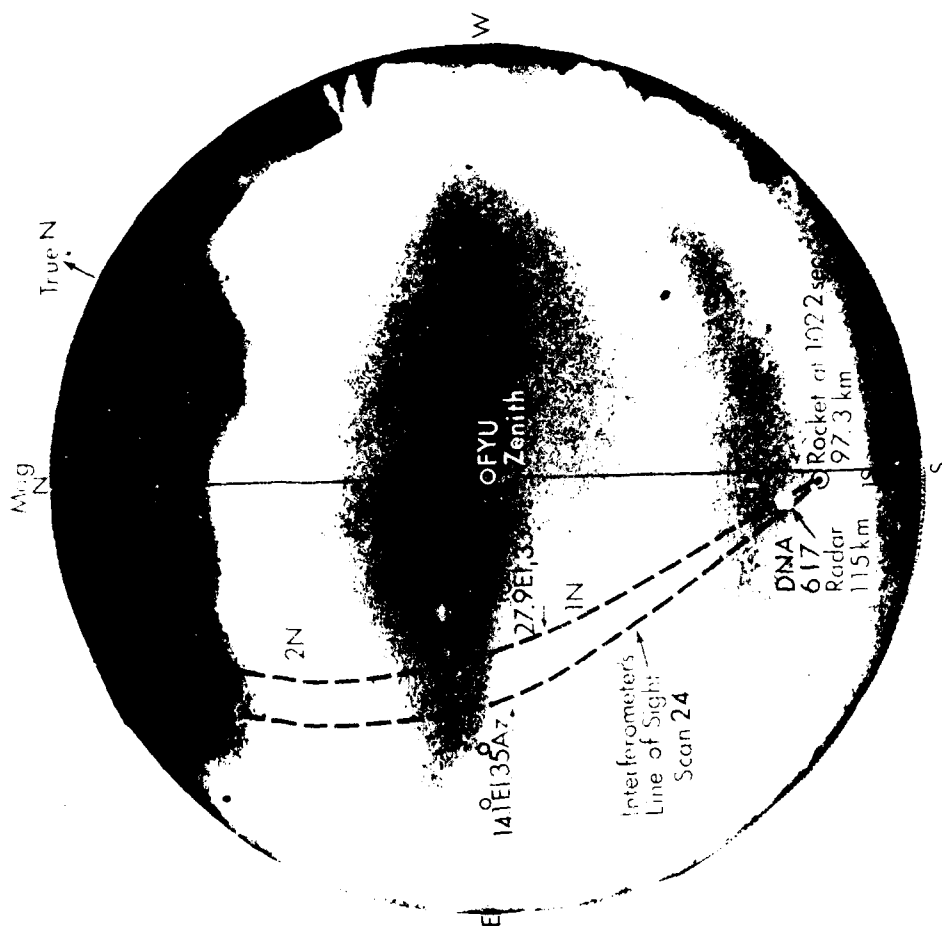
Figure 7. All-sky view from Fort Yukon of the distribution of visible air fluor-escence between 100 and 109 sec after launch of HIRIS II. The pro-jection of the axis of the interferometric spectrometer's field of view during scan 24 (with elevation and azimuth angles measured from the rocket), and the Chatanika radar beam's intercept at 115 km altitude are shown.

Scan 137

Fig 5 indicates that the dependence of visible radiance on elevation angle, as viewed from PKR, was similar in the pointing directions of the PKR photometer and the rocketborne interferometer. An equidensity contour plot of this continuous-tone film frame, which quantifies the radiance distribution, shows that the error introduced by applying the PKR photometer's geometry to the spectrometer's field was small compared to the other errors in assessing power input. This plot also shows that the auroral radiance was sufficiently uniform in the E-W direction to allow triangulation to the nearer isolated arc S of PKR (3 S in Fig 6) from the 1-dimensional "images" compiled by the two scanning photometers.

The photometer scans from the two stations closest in time to interferometer cycle 137 are reproduced in Fig's 8 and 9. From a comparison of N_2^+ First Negative band and OI 5577 $\overset{o}{A}$ intensities at three near-intercepts of the two fields at 110 km altitude (30° zenith angle from PKR – 50° from FYU, 45 – 35°, and 55° - 15°) it was found that the sky radiances reported from the PKR instrument are at least 50% higher than those from FYU. As PKR measures 3914 $\overset{o}{A}$ and FYU 4278 $\overset{o}{A}$, the result for N_2^+ emission is in the opposite direction to what would be expected from out-scattering by the atmosphere (without consideration of buildup). The aforementioned equi-density plot shows that this difference is not due to variations in auroral brightness over the small separation between the intercepts of the two fields. Further, the difference is not explained by a decrease in overall particle-precipitation in the short time between the starts of the two elevation scans. Thus the systematic variation in signal is most probably caused by a difference in the photometers' absolute calibrations.

The PKR meridian-photometer data and the all-sky photographs from the two stations were used in dividing the upper atmosphere within the spectrometer's field into four major emitting regions. This division allows altitude profiles of energy deposition to be fit to the discrete

50
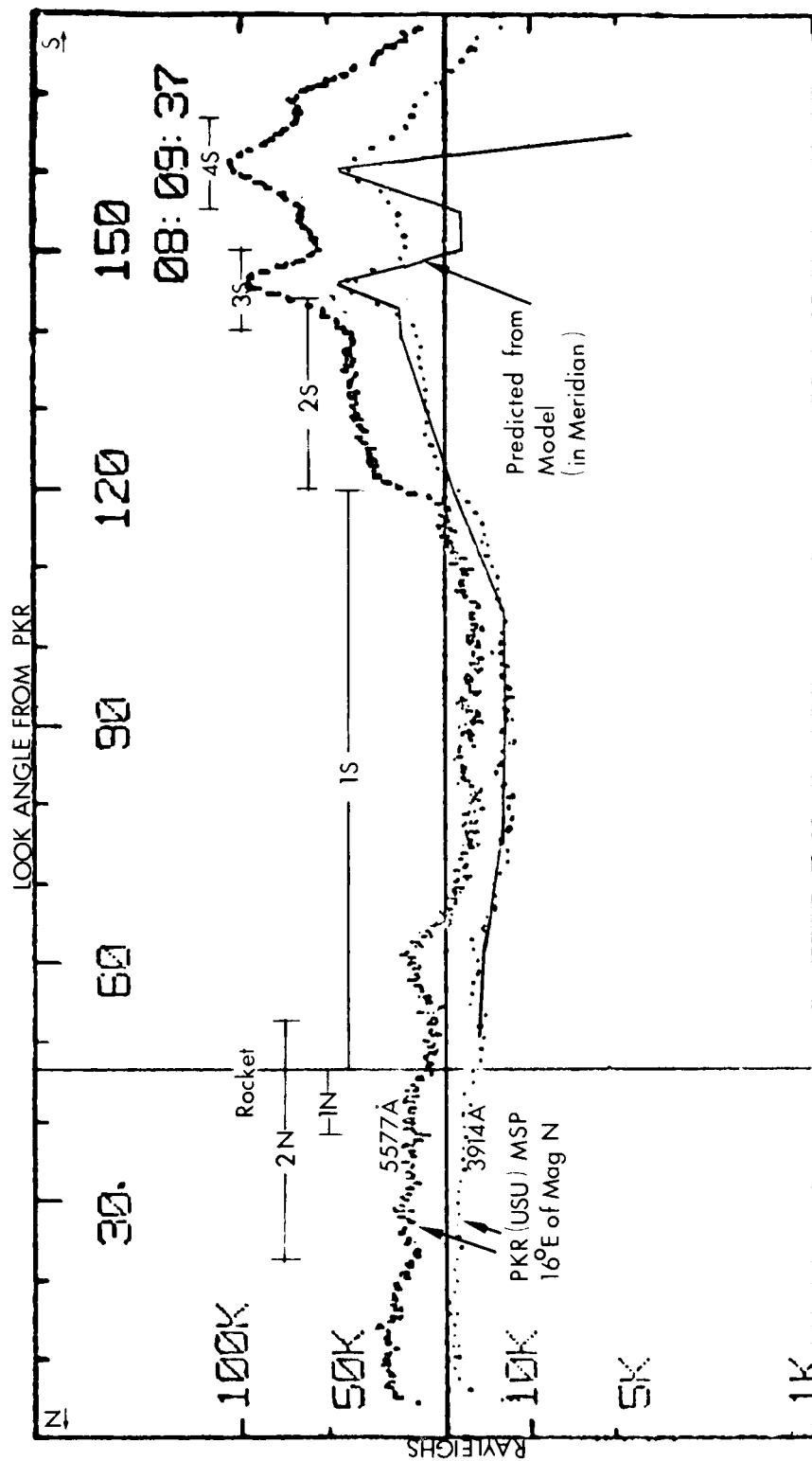
Figure 8. Photometer elevation scan from PKR in a plane 16° E of N starting in the north at 257 sec after launch of HIRIS II, with identification of emitting regions. The fit of the model system of discrete arcs and diffuse areas (for scan 137) is indicated by the solid line.
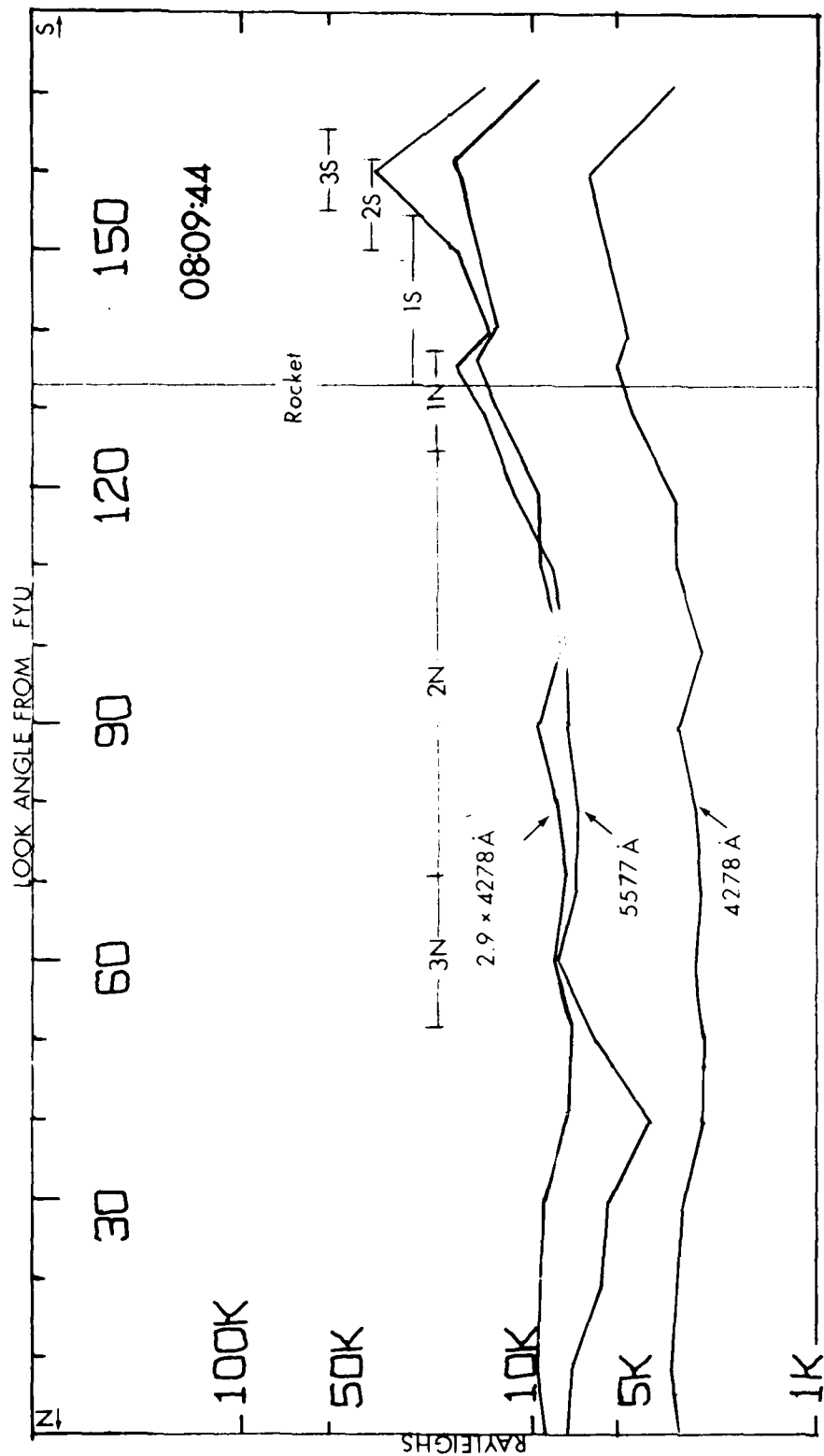
Figure 9. Geomagnetic meridian photometer scan from FYU starting in the north 264 sec after launch of HIRIS II, with identification of emitting regions (reduced from the film record and calibrations supplied by Poker Flat Research Range). The intensity of the N_2^+ First Negative 0, 1 band with head at 4278 Å is 1/2.9 that of the 0,0 band at 3914 Å, when scattering is neglected.

arcs and large diffuse areas, into which are incident electrons having different characteristic energies. The resulting schematic meridian plane projection of the emitting features in the instrument's field is shown in Fig 10.

The more northerly of the two intense arcs to the south, (3 S in Fig 6), which lies near 57° zenith angle from PKR, was located by the two-station triangulation procedure in Ref 1 . The altitude of peak emission from this arc was found to be near 115 km, and its horizontal distance from PKR 150 km. A second arc far to the south, peaking at 72° zenith angle from PKR (labeled Region 4 S) is effectively outside the field of the FYU photometer. As it has about the same apparent intensity as the 57° arc its peak emission is assumed to be at the same altitude, and it is therefore placed as shown on Fig 10. Both isolated arcs are as usual taken to be oriented along the geomagnetic field, 13° S of the zenith.

Model volume emission rate profiles for these two regions were derived using the procedure in Ref 18, assuming a power-exponential energy distribution of the form $N(E) \sim E \exp -(E/\alpha)$ for the incoming electrons. The 115 km altitude of peak radiance is fit by characteristic energy $\alpha = 3$ keV. A characteristic energy of 1.4 keV was adopted for the diffuse-auroral regions (1 S and 2 S), on the basis of recent observations that show these regions usually to be associated with stably trapped electrons having characteristic energy lower than 2 keV (Ref 19). Additionally, the Chatanika radar measured α's of $\sim$1.5 keV a few minutes before HIRIS II was launched in what appears to be a similar background-aurora region (Ref 20). The resulting peak emission altitude for these large areas is about 135 km. The volume emission rate profiles were taken as uniform across the horizontal "width" of each of the regions.

To validate and normalize the intensity calculation, we attempted to reproduce the radiance distribution measured by the PKR scanning photometer by varying the boundaries of the four idealized regions.

53
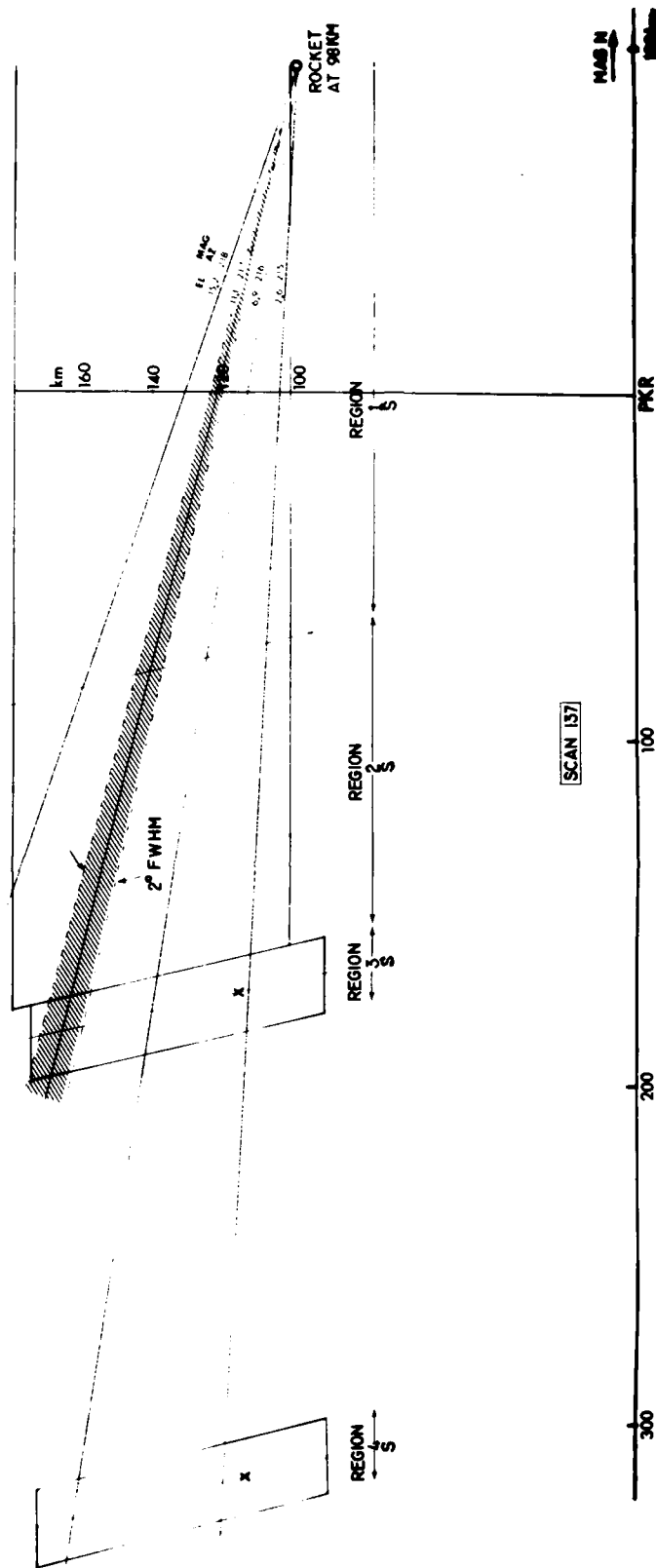
Figure 10. Meridian plane projection of the HIRIS II interferometric spectrometer's viewing geometry on the model fluorescing regions during scan 137. Earth curvature was taken into account in the actual calculation of column emission rates within the instrument field.

54

(The data from FYU were not used photometrically because the scan 137 auroral features lay so near that station's southern horizon that scattering corrections would be subject to unacceptably large error.) Uniformity over 5 km altitude intervals was adopted for the calculation. The relative volume emission rates assigned to each cell were then summed over that column in which maximum radiance was measured to normalize the absolute rate at the altitude of peak deposition (which need not coincide with the altitude of peak surface brightness). This procedure inherently takes into account the increasing path length through the emitting regions with increasing zenith angle from PKR, that is, the van Rhijn gain. The optimum synthetic meridian scan, reproduced in Fig 8 from the geometry of Fig 10 (the arcs 3S and 4S "fit" at 20 km width), shows reasonable agreement with the PKR data, indicating that the excitation model adopted is satisfactorily self-consistent.

The elevation angle of the instrument's optic axis decreased from 15.2° to 1.4° in the course of the 1.26-sec interferometer scan. The rocket, 94 km N of PKR and at 98 km altitude, was about 260 km NE of the field's intercept on the nearer discrete arc (Region 3S; refer to Fig 10). Thus during the compilation of interferogram 137 the instrument made an essentially vertical scan of the two arcs (as Fig 10 shows), extending over 70 km ($260 \tan 15^\circ$) on the nearer one, and over an even greater altitude range on the more distant one. The viewing geometry also included long path lengths through the diffuse, higher-altitude emitting regions 1S and 2S that lay between the arcs and the rocket probe.

The model 3914 $\overset{o}{A}$ volume emission rates within the interferometer's field of view were summed, taking into account earth curvature (which raises intercept altitudes on the more distant (Region 4S) arc by 14 km). The resulting apparent column emission rates are shown in Fig 11. Most of the air fluorescence in the earlier half of the spatial scan comes from the diffuse nearby regions, as the field intercepts the distant isolated arcs at high altitudes were volume emission rates are low (see Fig 10). Later when the field swings nearer the rocket's

55
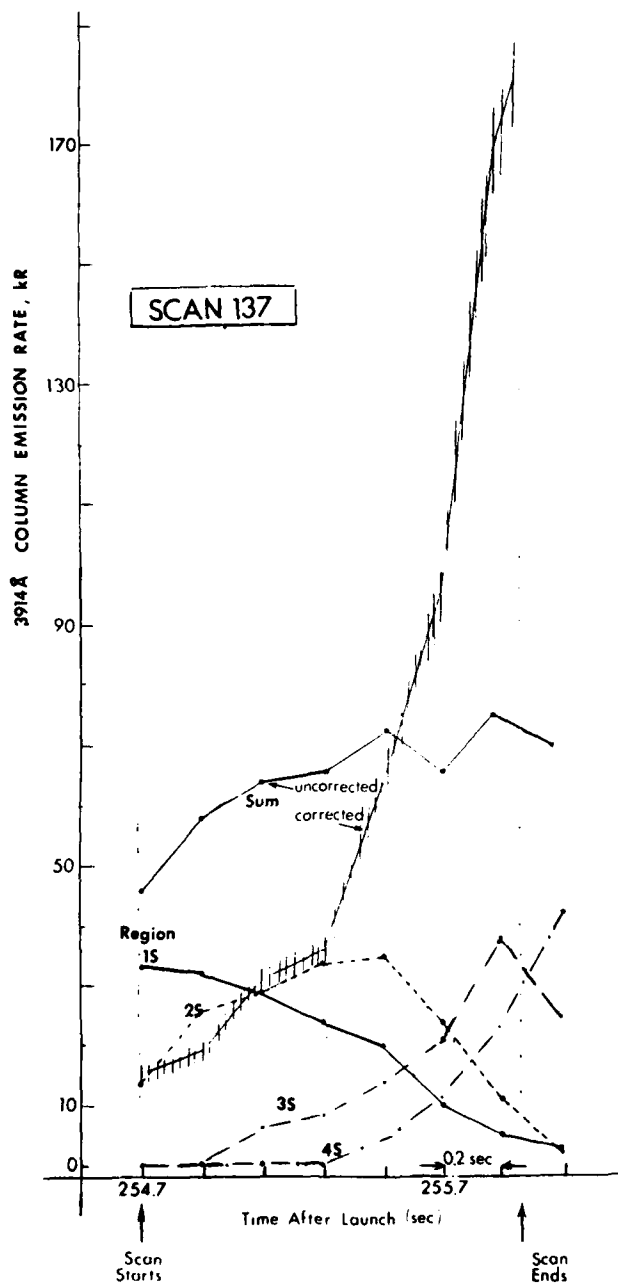
Figure 11. Power input within the HIRIS II interferometer's field during scan 137. The vertical hatched line is the total after correction of the input data for out- and in-scattering by the lower atmosphere; the vertical extent of the hatching is not intended to reflect the estimated uncertainty. Individual contributions from the four emitting regions, labeled 1S - 4S in Fig 6 , are uncorrected.

horizontal, it cuts altitudes below the diffuse regions and at which the harder electrons present in auroral arcs deposit their energy. As would be expected from the near-equality of the path lengths through the isolated arcs from PKR and from the rocket, the maximum 3914 Å radiances calculated are not substantially different from those measured by the ground-based photometer (in Fig 8).

Scattering in the lower atmosphere decreases the apparent radiance of the intense arcs toward the horizon 3S and 4S, photons from which contribute to the apparent brightness of the fainter regions 1S and 2S. The particle-energy flux measured in the northern section of Region 1S from the PKR photometer data can be checked against that inferred from the incoherent-scatter radar data in Ref 20 using the procedure described in Section V of Ref 3 (see also Ref 21). (The radar returns, which refer to 15° az $- 43^\circ$ e ℓ, appear to have a component from reflection off the rocket body.) Manual integration from the electron density contours of the auroral ionosphere measured at 255 sec (Fig 14 of Ref 20), adopting a recombination coefficient of 3×10^{-7} cm^3/sec and one 3914 Å- band photon emitted per 22 ion pairs, gives an equivalent 3914 Å radiance at 47° zenith angle of 10 kR. The "average" vertical energy flux during HIRIS II's flight quoted in Ref 20, 8 erg/cm^2 sec, also converts to 10 kR (47° tilted) column emission. 3914 Å brightnesses from PKR measured photometrically (Fig 8) are nearer 15 kR. (Compare Fig 70 of Ref 3, which places the radar-derived column intensities similarly below the photometrically-derived intensities away from bright arcs.) This indicates that about a third of the photons appearing to come from the direction of Region 1S actually originate elsewhere, most probably in the strongly-irradiated regions to the south. The best-estimates in Fig 11 for the section of the interferometer scan during which column intensities are dominated by Region 1S and 2S have been lowered to reflect this artefact.

A larger and potentially more uncertain correction is required for the two bright arc regions, which are 1.8 to 3.2 air masses from

the photometer at PKR. Narrow-beam transmission of 3914 Å radiation through a clear winter model atmosphere is 0.53 per air mass, the outscattering being very closely half Rayleigh-molecular and half due to aerosols (Ref 22). The actual meteorological conditions, as measured at Fairbanks airport and reported in Ref 15, are reasonably expected to reflect the model. Air temperature was 23° F and visibility 15 miles, and therefore the concentration of aerosols would not be anomalously low. The model narrow-beam transmissions to arc Regions 3S and 4S would then be 0.33 and 0.126 respectively.

Buildup of in-scattered photons in the directions of these two arcs has the effect of raising the atmosphere's effective transmission. An estimate for 57°, following the result for a similarly-located arc in Fig 70a of Ref 3, is 0.5. For 72° zenith angle, a reasonable corrected transmission is 0.2. The peak corrected brightness then becomes 84 kR and 210 kR respectively. Because of the large van Rhijn gains, these *regions would appear as only IBC III aurora to an observer directly* below.

The inherent uncertainty in correcting for buildup makes the accuracy of the power input estimate in Fig 11 decrease toward the end of the interferometer scan. Mean error is expected to be about ± 50%. Accuracy could be increased by applying the radiation-transport calculation procedures outlined in the references listed in Section V of Ref 3.

The effect of correction for in- and out-scattering of photons by the lower atmosphere is to show the strong variation in particle energy input to the air volume within the instrument's field during this interferometer scan. Increases in fluorescent radiance with instrument elevation angle or rocket altitude as large as that shown in Fig 11 have in fact been routinely measured by ICECAP's multi-instrumented rockets' side-viewing photometers, under generally-similar conditions of auroral particle irradiation.

Scan 125

During this scan the interferometer's optic axis swings up from 6.2° below to 8° above the horizontal from 108.5 km altitude. Fig's 5 and 6 show the instrument to be "inside" arc 1 N, with its field extending through the same angular region as the broad diffuse glow 2 N and the bright patch 3 N. As this last area lies outside the region scanned by the ground-based photometers, its radiance distribution was measured with the aid of the equi-density contour plot of (a copy of) the FYU all-sky negative, shown as Fig 12. Absolute values were assigned to contours by reference to the FYU 4278 Å meridian photometer scan starting in the north horizon at 237 sec. The data from FYU were used to avoid the severe and uncertain correction to the auroral intensities needed for the high zenith angle view from PKR. All FYU radiance readings were increased by 50% to standardize sky brightnesses to those measured at "crossovers" by the USU elevation-scanning photometer at PKR.

Triangulation from the two ground stations placed the maximum of arc 1 N at 115 km altitude. As Region 3 N had comparable peak brightness, emission altitude profiles that would result from a maxwellian incoming-electron beam with characteristic energy 3 keV were assigned to both areas. Following the same arguments used for scan 137, a characteristic energy of 1.4 keV was adopted for diffuse Region 2 N. Fig 13 shows a meridian-plane projection of the three regions, and Fig 14 (bottom) the calculated column intensities. Vignetting by the all-sky lens (10% at 40° zenith angle, 20% at 60°; Ref 23) was taken into account in transferring the photometer data to Region 3 N. This strongly-emitting volume, ~ 150 km from the HIRIS II rocket, lies below the interferometer's field near the beginning of the scan cycle.

The model atmosphere of Ref 22 predicts narrow-beam transmission of 0.57 per air mass for 4278 Å radiation. Taking into account buildup as described for scan 137, we estimate an effective
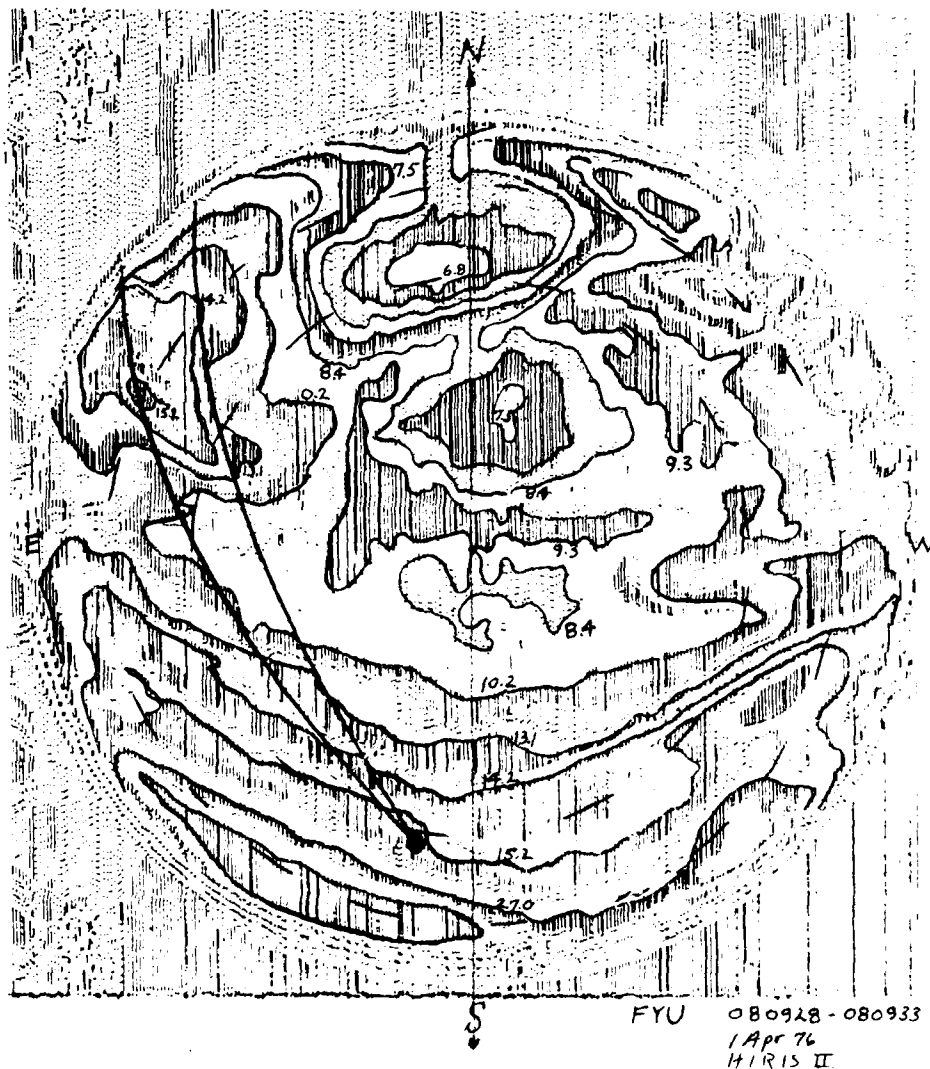
Figure 12. Equi-density contour plot from the FYU
all-sky frame 248-253 sec after launch
of HIRIS II.   Absolute brightnesses in units
(2.9 x N_2^+ 4278 Å) kR were assigned to the
contours from the FYU meridian photometer
data, without correction for vignetting by
the lens (10% at 40° zenith angle, 20% at 60°:
this was taken into account in the final
calculation of column intensities).

Figure 13.   Meridian plane projection of the HIRIS II interferometric spectrometer's viewing geometry on the model fluorescing regions during scan 125. The volume emission rate profile for a "maxwellian" electron beam with characteristic energy α = 3 keV is that adopted for the discrete intense arcs (such as Regions 1 and 3).
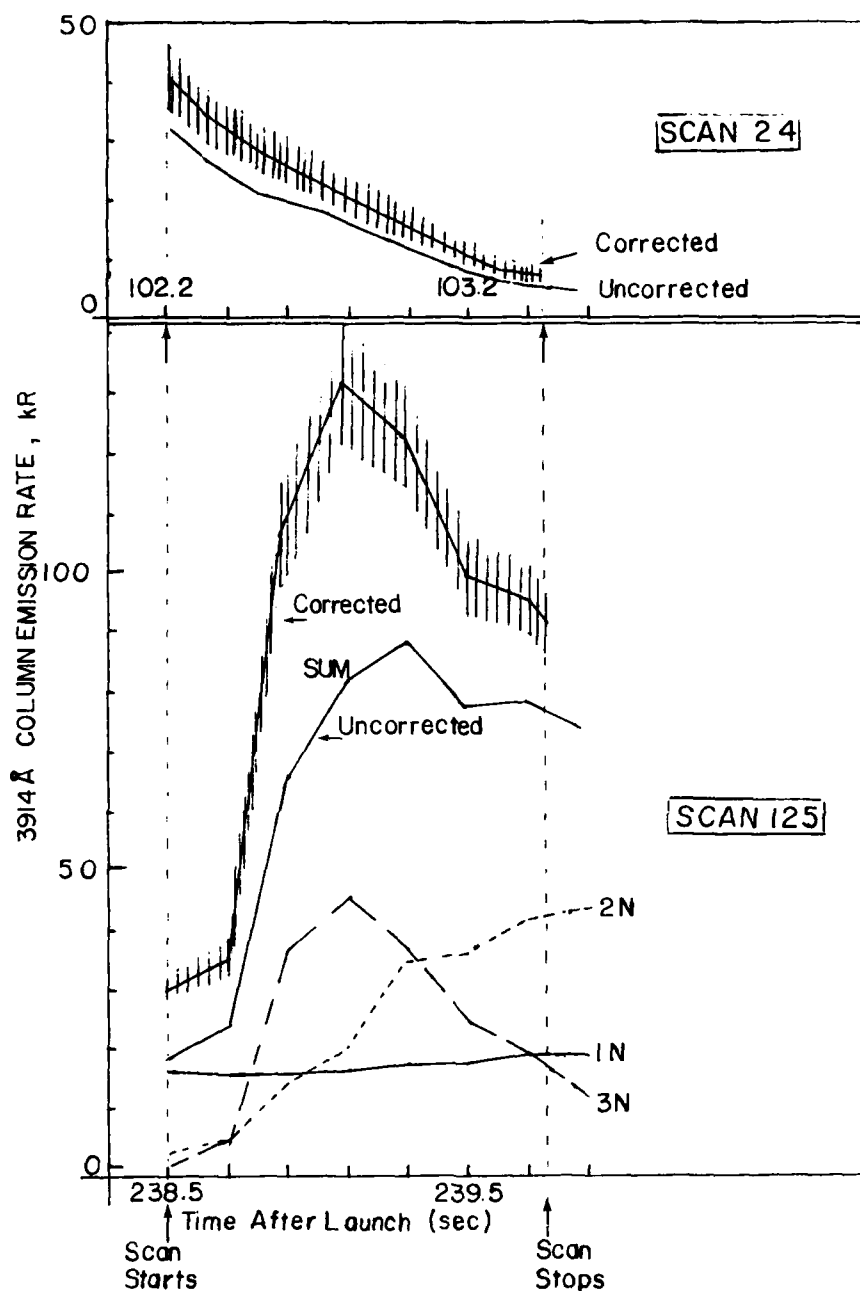
Figure 14. Power input within the HIRIS II field during scans 24
(top) and 125 (bottom). The vertical hatched line in
each plot represents the total column intensity after
correction of the input data for out- and in-scattering
by the lower atmosphere (hatch length again does not
indicate the expected accuracy). Individual contri-
butions from the three emitting regions in scan 125
(1N - 3N) are uncorrected.
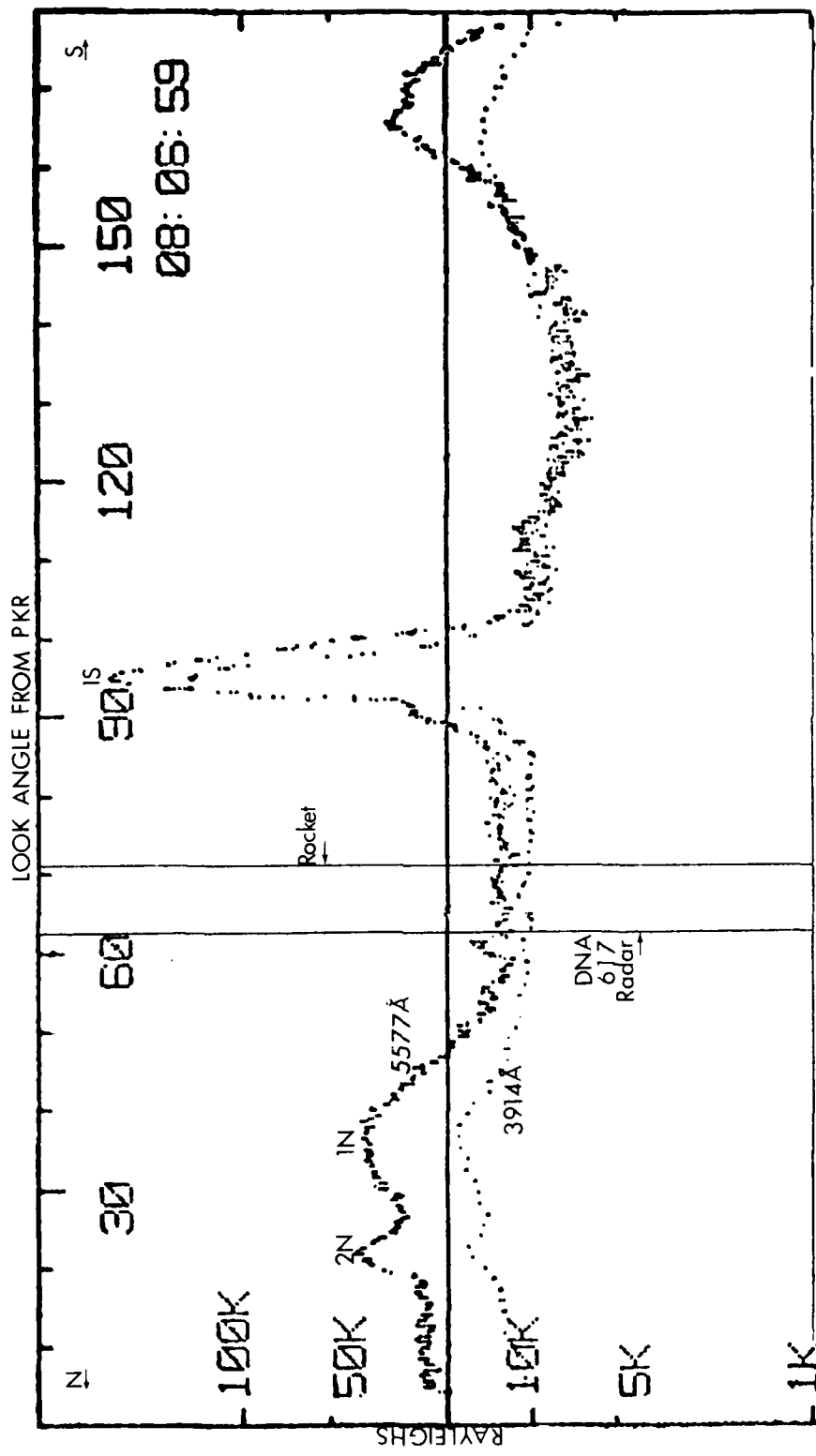
Figure 15. Photometer elevation scan from PKR in a plane 16°E of Mag N starting in the north at 99 sec after launch of HIRIS II. The emitting regions (for scan 24) are identified; and the directions to the rocket and of the Chatanika radar beam are as shown. Note the highly variable 5577 Å/ 3914 Å ratio, suggesting substantial buildup of the shorter wavelength radiation.

63

transmission of 1/1.7 for Region 1 N (40° zenith angle), 1/2.0 for 3 N (60°), and 1/0.67 for the diffuse glow 2 N. The resulting best-estimate column emission intensities during scan 125 (hatched line in Fig 14) have a mean about 50% above that of scan 137 (Fig 11) with some-what less extreme variation over the period in which the interferogram is compiled.

Scan 24

During this upleg scan the interferometer's optic axis points between 14° and 28° elevation angle from 98 km altitude. Fig 7 shows the projection from FYU of the instrument's field against the projection of the photographic-visible aurora. The two north-lying arc regions labeled 1 N and 2 N, and the narrow intense arc 1 S near PKR's zenith (which contributes to the apparent sky radiance north of PKR), are also indicated in the USU photometer's elevation scan, Fig 15.

Arc 1 N is too broad and diffuse to permit effective triangulation (it projects as a uniform band extending 30° in zenith angle in the FYU meridian photometer's scan). Since its radiance is comparable to that of the bright arcs in Fig's 5 and 6, we assigned to 1 N the same relative altitude profile (for 3 keV characteristic electron energy). Two-station triangulation to arc 2 N placed the peak volume emission rate at 107 km, or α = 5 keV. The resulting meridian-plane projection in Fig 16 shows that Region 2 N, despite its high (IBC III-) surface bright-ness in the views from FYU and PKR (Fig 15), makes only a negligible contribution to the intensities in the columns from the rocket in scan 24. In addition most of the emission in the weak diffuse region between the rocket and Region 1N would be expected to lie above the instrument's field of view.

The 3914 $\overset{\circ}{A}$ vertical-column intensity in this diffuse region calculated from the incoherent-scatter radar data (Fig 14 of Ref 20) is 3-4 kR at 103 sec. The photometrically-measured intensity in the
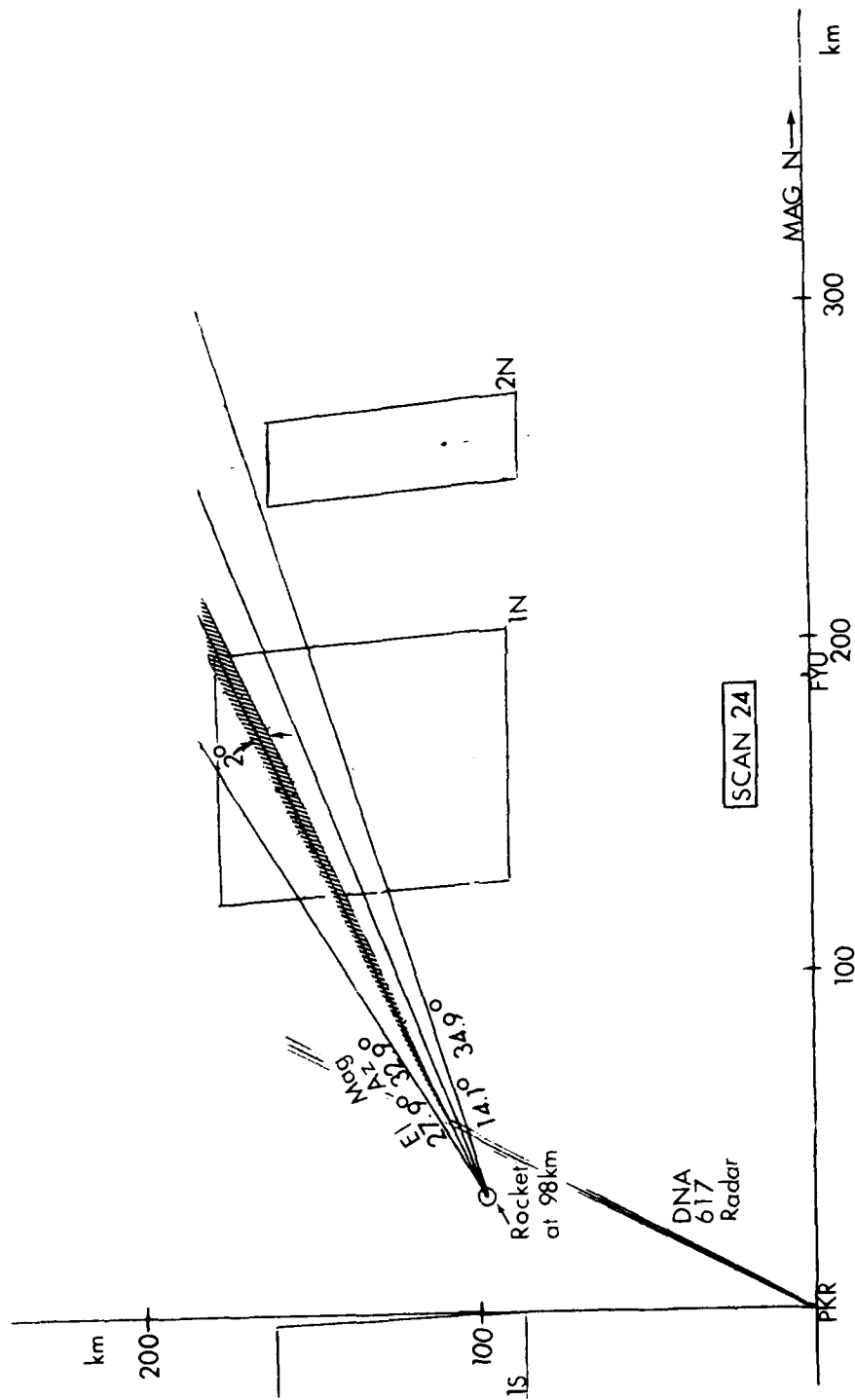
Figure 16. Meridian plane projection of the HIRIS II interferometric spectrometer's viewing geometry on the model fluorescing regions during scan 24. The Chatanika radar's beam is pointing to the weakly-irradiated region between arc Regions 1 N and 1 S (see Fig 7).

same pointing direction, corrected to the zenith, is 10 kR from PKR
(Fig 15) and 8-9 kR from FYU (4278 Å data adjusted to 3914 Å).
The difference between the photometric and radar-derived results is
in all probability due to photons from the bright arcs $\sim 30^{\circ}$ to the N
and S of the region of auroral ionosphere scattered in the direction of
the instrument by the lower ionosphere. To correct the fluorescent
intensities measured in Region 1 N, we subtracted 6 kR 3914 Å for this
buildup, applied the narrow-beam transmission of 0.57 per air mass,
and then increased this first-approximation effective transmission by
10% to take into account increased inscattering from the broad emitting
region itself and arc 2 N.

The resulting wide-beam transmission of 1/1.3 (which is high
because of the low zenith angle of the emitting feature and the strong
particle irradiation nearby) was used in calculating the best-estimate
column intensities plotted in Fig 14. The average energy deposition
rate during compilation of HIRIS II interferogram 24 is about 1/6 that
of interferogram 125. Although the absolute column fluorescent in-
tensity is low, the relative variation of input during this scan cycle is
comparable to that for the two Rotation 5 scans.

PREVIOUS DOSING, COMMENTS

Fig's 11 and 14 summarize the results of this calculation of
the rates at which charged particles from the magnetosphere deposit
energy into the air lying in the HIRIS II spectrometer's field of view
during three 1.26-sec data-taking periods. The time variation, a
feature of all the scans, is due to the large (and monotonic) change in
altitude at which the projection of the rotating instrument's field
intercepts the profile of energy absorption. Best estimates of the
average power inputs for interferograms 137, 125 and 24 are 62, 94,
and 17 kR 3914 Å respectively. (Multiply by 22 x 35 x 10^9 for units
eV/cm^2 -col sec.) The ratio for the two Rotation 5 scans is much
nearer unity than indicated by first-cut calculations that neglected

earth curvature, applied N_2^+ First Negative band radiances with the calibration of the FYU photometer, and (in particular) missed the important contribution of Region 3 N.

These power inputs, whose accuracy is estimated at roughly ± 50% (the principal source of error is expected to be the correction for scattering of the air-fluorescence photons by the lower atmosphere), are based on the calibration of the Utah State University elevation-scanning photometer that operated at Hilltop station, Poker Flat Research Range. The accuracy could be somewhat increased by using the N_2^+ First Negative band/OI 6300 $\text{\AA}$ line intensity ratios to improve determination of peak arc emission altitudes. This was not attempted primarily because the uncertain state of the calibrations of the meridian photometers that measured oxygen red-line emission did not appear to justify the effort in correcting, using the radiation transport methods referenced in Ref 3, for scattering to ground stations from extended sources at high zenith angles.

Total column energy inputs in times less than 30 sec previous to each scan can be estimated by multiplying the averaged power inputs given above by the desired interval. (An expected upper limit to the period over which predosing affects production of $NO^{\neq}$ ($v \geqslant 2$) is about 30 sec (Appendix I)). During the ~ 40 sec just before scan 24 the broad arc region 1N moves south at 1° zenith angle per 10 sec, while its surface brightness decreases by about 35%; the lowering of the intercept altitude of the instrument's field toward the "bulge" in the profile (refer to Fig's 13 and 16) compensates the column intensities for the decreased precipitating-particle flux. The change in spatial distribution and intensity of the optical aurora just before and during Rotation 5 is expected to have less effect on power inputs than the estimated error in the power-input calculations, and therefore a constant predosing rate can be applied for interferograms 137 and 125.

SECTION 3

INTERPRETATION OF A18.219-1's LOW ALTITUDE SWIR DATA

INTRODUCTION

We finalize here our preliminary interpretation (in Section I of Ref 4) of the angular distribution of 2.43- 3.11μm radiance that was measured by HAES rocket A18.219-1's sidelooking filter radiometer on downleg at altitudes below about 92 km. Our conclusion remains, that the SWIR signal is due to a combination of earth-limb radiations and the air fluorescence-associated emission also measured at higher rocket altitudes. That is to say, the data from the side-pointing instruments can be explained without invoking a contribution from the thermally-emitting rocket wake material that is thought to have entered the field of the axially pointing variable-filter radiometer (Appendix B of Ref 16), an artefact that impacts interpretation of the 2.8μm altitude profile and emission mechanism (p 404 ff of Ref 5, and Ref 16).

DATA REVIEW

Our previous reduction of these data (Section II of Ref 3) indicated that when the rocket altitude was between 120 and 95 km the radiant intensities measured by the SWIR radiometer and fluor-escence photometer correlate moderately well, both over complete elevation-azimuth scans and in directions where the column emission rate was high. The photon ratio shows a minimum near 110 km, perhaps related to the collisional quenching processes described in Appendix A of Ref 12 (refer to Fig's 47b and 50c of Ref 3). The column-intensity data taken as a whole, and without correction for SWIR "background" not obviously associated with prompt air fluor-escence, indicate that on the average 8.7 in-band photons are emitted per N_2^+ First Negative 3914 Å-band photon (the straight-line fit shown in Fig 51 of Ref 3). In pointing directions at which the radiances are high over a series of rocket spins, the background level lends itself

to subtraction; this decreases the photon ratio to 5. The resulting effective chemiluminescence efficiences for an assumed spectrum of NO $\Delta v = 2$ vibrational band radiation, 0.6% and 0.3+ %, straddle the 0.45% inferred from laboratory data (if $1\frac{1}{2}$ N^2D atoms are produced per ion pair, p 250 of Ref 5). An altitude-integrated figure of 0.6% is determined from one aircraft flight of a 2.76-2.9μm FWHM radiometer underneath auroral particle-excited air (the result given in Section IV of Ref 3 corrected for the overtone cascade spectrum recently derived from the laboratory results).

As A18.219-1's altitude decreases below 92 km, a van Rhijn increase-like cyclical background becomes superposed on the radiometer's signal, so that the apparent correlation extends over an increasingly smaller range of azimuth. (Recent identification of a 90° correction to the reported azimuth angles (Section I of Ref 4) renders invalid our first discussion of this excess radiation (p 98 of Ref 3). By 85 km the mean radiance level over a spin cycle has reached $\sim 2\frac{1}{2}$ MR, reducing strongly the "contrast" of any fluorescence-related SWIR component; see for example Fig 49b of Ref 3 (for which the abscissa should be shifted in azimuth by -90°).

ASSESSMENT OF THE BACKGROUND

We adopt, and then test, the hypothesis that the excess signal when the rocket is below 92 km is due to hydroxyl airglow plus leakage into the imperfectly-baffled radiometer of thermal radiation from the atmosphere.

Chemiluminescent emission from the OH Meinel bands comes principally from the altitude range 80-90 km, and has typical vertical-column intensity $\frac{1}{4}$ MR $\pm$ a factor ~ 2 in the radiometer's passband (depending on geophysical conditions; see Appendix III of Ref 3). The thermal component's apparent intensity depends on the sensitivity of the radiometer to off-axis radiation, and would be expected to be azimuthally symmetric. If the aforementioned wake material were distributed about the rocket in a flat uniform "pancake," it would mimic this earth-limb radiation.

The total radiometer signal B(IR) is the sum of the fluorescence-related and background signals, which can be expressed as

$$B(IR) = C \cdot B(F) + f(h) \cdot \csc \Theta.$$

Here B(F) is the measured 3914 $\overset{\circ}{A}$ N_2^+ -band fluorescent intensity, C is the column-averaged photon ratio (fluorescence-associated SWIR)/ (3914 $\overset{\circ}{A}$), and f(h) $\csc\Theta$ is the contribution from OH airglow plus thermal leakage radiation when the instrument's optic axis points at elevation angle Θ from altitude h. A cosecant or van Rhijn-like radiance dependence is adopted because of its past success in explaining results of rocket photometry; specifically, this functional form "linearized" radiometer leakage near 5.3μm (Section I of Ref 3) and optically thin thermal 4.3μm radiation (Section I of Ref 4). C was set at 5.0 photons/photon for the initial calculations.

The results of application of this relationship to the data from five rocket spins starting between 83.6 km and 94.4 km altitude are shown in Fig's 17a-j. All the plots of the background radiant intensity (B(IR)-CB(F)) show the same general behavior as those of Fig 4 of Ref 4 ; a roughly linear dependence on path length; an increase with decreasing altitude during a single spin (in which the rocket's altitude decreases by $\sim \frac{1}{2}$ km), so that the graph of intensity against $\csc\Theta$ does not close on itself; and a weakening dependence on elevation angle with increasing altitude. They also fail to show discernible dependence of the excess 2.42-3.11μm signal on azimuth angle, which indicates that if the wake material is contributing it must be essentially uniformly distributed in azimuth. Similar data from the (lower) altitude at which the rocket's axis has erected to near the vertical as it starts to destabilize — so that the cosecant of the radiometer's elevation angle varies by only $\pm$ 25% in $\sim 1\frac{1}{2}$ spin cycles (Fig 18) — provide further confirmatory evidence of the lack of azimuth dependence.
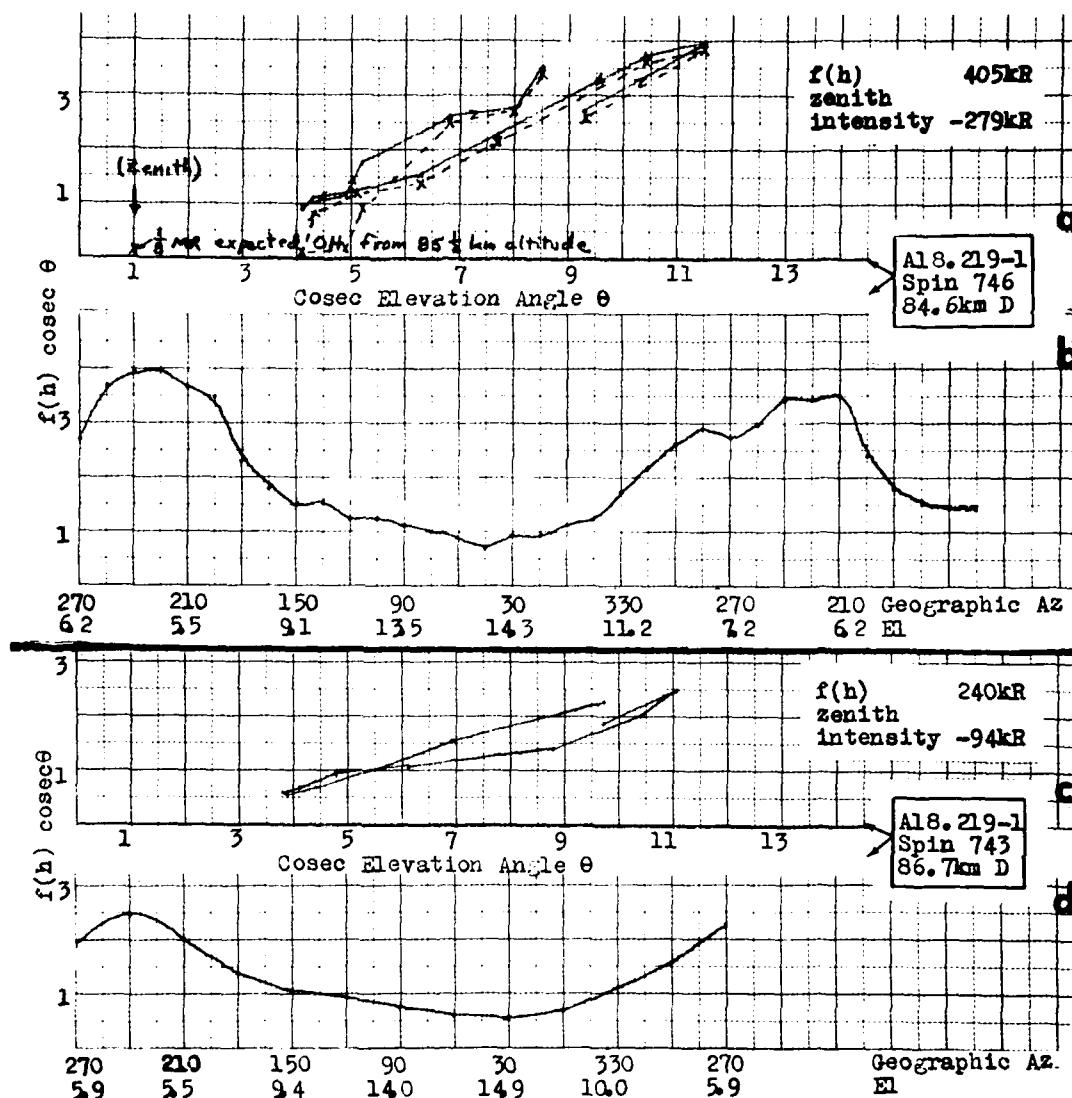
Figure 17a -j. Plots of f(h) x cosecant (radiometer elevation angle Θ) against cosec Θ and against geographic az/el for five downleg spin cycles of A18.219-1. Dots and solid lines are calculated with a 2.8μm SWIR/N_2^+ λ3914-band photon ratio of 5.0; x's and dashed lines assume 8.7 photons/photon (see text). The least squares best-fit slopes f(h) and extrapolated zenith intensities are shown at upper right of the plots for each altitude.

f(h)   140kR
zenith
intensity 15kR

A18.219-1
Spin 740
33.8km D

e
f

f(h)   61kR
zenith
intensity 111kR

A18.219-1
Spin 736
91.6km D

g
h

f(h)   0kR
zenith
intensity 332kR

A18.219-1
Spin 732
94.4km D

i
j
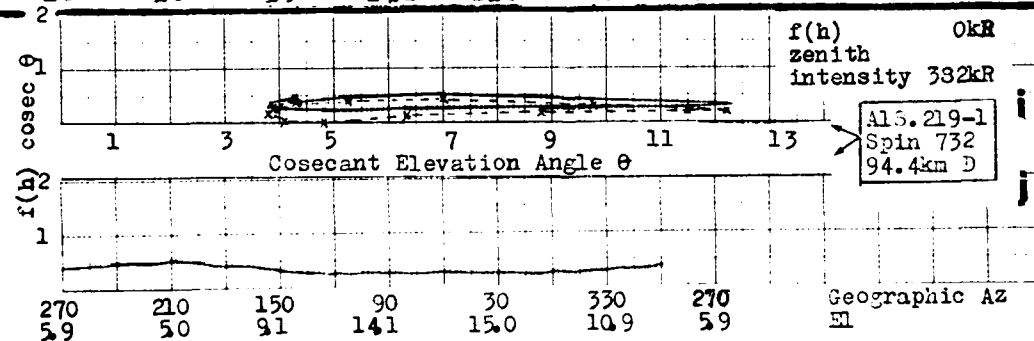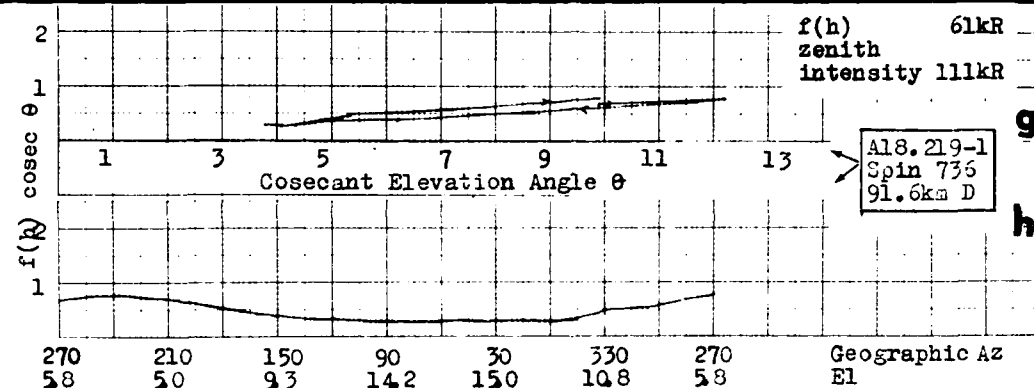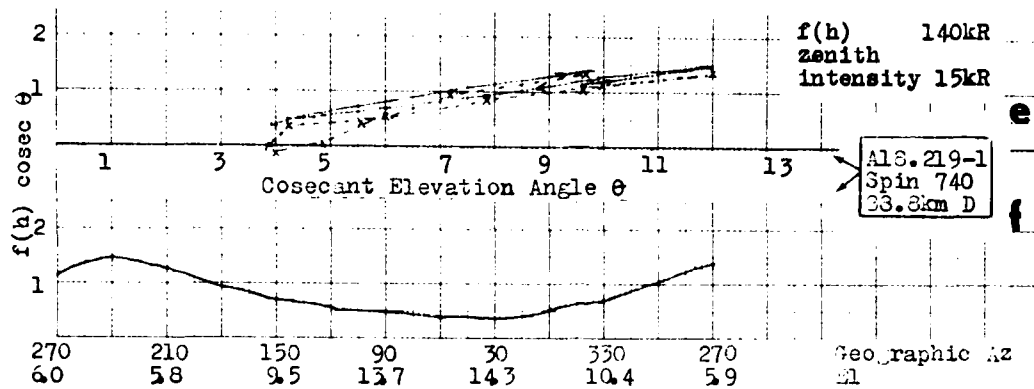
Consider next the variation of radiance with el-az at 84.6 km (Fig 17a). Although the data do not have sufficient resolution to permit accurate extrapolation to high elevation angles, they do indicate that intensity at the zenith would be substantially less than 1 MR; a best-fit to the data points in fact indicates a small negative intercept. From this altitude the expected OH zenith intensity in the radiometer's passband is about 0.1 MR. On the other hand the measured radiances at low elevation angles are about a factor two higher than predicted by an accurate calculation that uses the OH $\Delta v = 2$ altitude profile determined in ICECAP flight A30.205-3 (06 Mar 72) and corrects for the finite (5° FWHM) field of view of the radiometer (Fig 10 of Ref 24). For example at 7° elevation the model of Ref 24 predicts 1 MR, while A18.219-1 data show $2\frac{1}{2}$ MR. Thus some azimuth-independent emission other than hydroxyl airglow alone is needed to explain the elevation-angle dependence of the signal as the axis of the instrument's field approaches the horizontal.

The dependence on rocket altitude of the total excess radiometer signal is measured by $f(h)$. This parameter, determined from the slopes of the least-squares-fits to the plots in Fig's 17a, c, e, g and i, is shown in 19a for the altitude range $94-84\frac{1}{2}$ km. The essentially-linear. increase of $f(h)$ with air density at the rocket (Fig 19b) provides strong evidence that leakage of thermal radiation from the atmosphere — frequently present in past rocket data taken with infrared radiometers of very similar design — is the source of the excess signal.

A partial recalculation with $C = 8.7$ photons/photon (Fig's 17a, e, i) gives qualitatively similar results, but with lower (higher negative) values for the radiance intercepts at the zenith. This suggests that the higher value of C overcorrects, so that the lower photon ratio probably more accurately represents the SWIR chemiluminous efficiency.

CONCLUSION

This analysis shows that the side-viewing radiometer signal overlaying air fluorescence-associated SWIR emission below 94 km

Figure 18. Azimuth-elevation angle plot of f(h) cosec Θ at 83.1 km on downleg of A18.219-1, when the rocket was nearly vertical.

Figure 19a-b. Altitude and atmospheric-density profiles of f(h) as determined in the text.
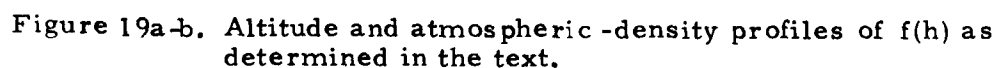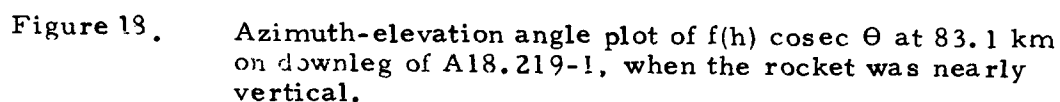
on downleg of A18.219-1 is consistent with thermal and hydroxyl-airglow radiation from the atmosphere. The excess signal is not related to destabilization-tipover of the descending rocket, which begins 10 km after the increase first becomes detectable. In order for rocket wake material to contribute substantially to the measured emission, it must both be distributed symmetrically in azimuth and have mean surface radiance proportional to the local atmospheric density. It should be noted that this analysis does not rule out the proposed (Ref 5) narrow wake above the rocket in the field of the axially viewing radiometer-spectrometer, which would be at elevation angles far above those reached by the side viewing radiometer; what it does show is that the excess signal from the side-viewing radiometers is in all probability unrelated to emission from such a source.

SECTION 4

4.3μm RADIATION PROFILES AND FLUORESCENCE-CORRELATED ENHANCEMENT ON UPLEG OF A18.219-1

INTRODUCTION

This Section contains a preliminary overview, without inter-pretation, of the air fluorescence-correlated increases in 4.21-4.305μm (FWHM) sky background unexpectedly present on upleg of A18.219-1 (25 Feb 74), and a reduction to altitude profiles of the data taken by the multi-instrumented rocket's side-viewing filter radiometer. It also includes some information on the source of the recurring spurious off-scale signals observed on upleg.

A weaker "near-prompt" component of the 4.3μm-band radiance in directions of particle-energy input was seen on downleg of this rocket flight, and is evaluated in Section II of Ref 4. The upleg radiometry data in addition carry some low-resolution information about spatial structure in the excess 4.3μm emission, which has potential impact on system performance. It should be noted that the model of the upper atmosphere's radiant intensity near 4.3μm curently dominant in the nuclear-effects community does not include prompt processes, but rather focuses on the partially-trapped 4.26μm CO_2 resonance radiation (Ref 25), which produces a "smooth" sky back-ground. On the other hand a body of thought exists (Ref 12) on other molecular species whose vibrational spectrums overlap the 4.2 - 4.3μm band (some of which figure in the aforementioned analysis of the down-leg data).

BACKGROUND, DATA QUALITY REVIEW

The radiometer's wavelength response is shown in Fig 18 of Ref 4 against model emission spectra of these species. Its field of

76

view is about 6° circular, and its optic axis points at 80° from the
sounding rocket's long axis, about which the rocket is rotating at 2.0
rev's/sec (refer to Section I of Ref 4 for a more detailed description
of the pointing geometry). After stabilization (86 km) this long axis
: :riented $5\frac{1}{2}^O$ from the zenith at geomagnetic azimuth 202°, so that
the elevation of the fields of the radiometer and coaligned photometers
swings between $4\frac{1}{2}^O$ at 202° az and $15\frac{1}{2}^O$ at 22° az. The distribution of
particle precipitation surrounding the rocket's trajectory is reviewed
in Section II of Ref 3, and a higher-resolution projection of the side-
looking radiometer's field on an intense stable auroral arc during the
periods of enhancement is shown later in this Section (in Fig's
26 and 27.)

Increases in 4.3μm-band intensity on both downleg and upleg at
azimuths where the 3914 $\overset{o}{A}$-band fluorescent intensity is high were
first noted in Section II of Ref 3, and a partially-correlated broad
4.3μm feature in the downleg data is reported in Section II of Ref 4.
In this latter Section we derived effective fluorescent-or-chemilumin-
escent efficiencies of $\frac{1}{4}$ to $\frac{1}{2}\%$ in the narrow-azimuth downleg en-
hancement, depending on the vibrational emission spectrum assumed.

Altitude and azimuth profiles of the component of 4.3μm radia-
tion at low elevation angles that does not follow the instantaneous
energy input are presented in Section I of Ref 4 for downleg. The
altitude profiles exhibit two regions of inflection, one above and one
below the altitude of maximum photon flux. This "layering" is
presumably due to the local increases in vibrational temperature of CO_2
caused by collisional energy transfer from particle-excited $N_2^{\ddagger}$, which
are overlaid on the profile of effective temperature that results from
transport of 4.26μm-band radiation from below (that is, it probably
comes from the superposition of long-period auroral pumping on the un-
disturbed vibrational distribution, as described in Ref 25). Because of
the greater predosing toward the north, the downleg and upleg altitude

profiles differ considerably, as shown in Fig 53 of Ref 3. The zenith data from A18.219-1 also show an increased 4.3μm radiance on down-leg, and similar differences between the two segments of the trajectory also appear in the data from other HAES rockets. The layering struc-ture, however, is not resolved in the vertical column views of the disturbed atmosphere. (Elevation and azimuth angles assigned to A18.219-1 in Ref 3 are in error, and are corrected in Section I of Ref 4. Thus the comparison of altitude profiles in Fig 53 of Ref 3 refers to $6 \pm \frac{1}{2}^{\circ}$ el, 180° geomagnetic az (viewing directly south, where no aurora-associated enhancements are discernible).)

The el-az scans from upleg of A18.219-1 were the last to be addressed because they show occasionally-strong noise pulses. In spite of this background, however, good quality altitude profiles can be derived, and show an enhancement in 4.3μm-band radiance in the general direction of the nearby auroral arc. Examples of the two types of noise in the radiometer traces are shown in Fig's 20, 21 and 22. Their altitude-and-azimuth "profile" may be characterized as follows

- (62 km: instrument door opens);

- 62-69 km: narrow ($\sim 10^{\circ}$ az) spikes up
  to 60 MR, similar to those from the
  2.4-3.1μm sidelooking radiometer (and
  also present in the radiometry data from
  the 1973 multi rocket A18.205-1);

- 69-91 km: many random noise spikes of
  peak typically 10 MR and occasionally
  50 MR, as shown in Fig 20 and 21a (the
  3914 Å trace has little noise and an
  el-az dependence similar to that reported
  from other multi rocket flights near
  isolated arcs, Fig 21b);
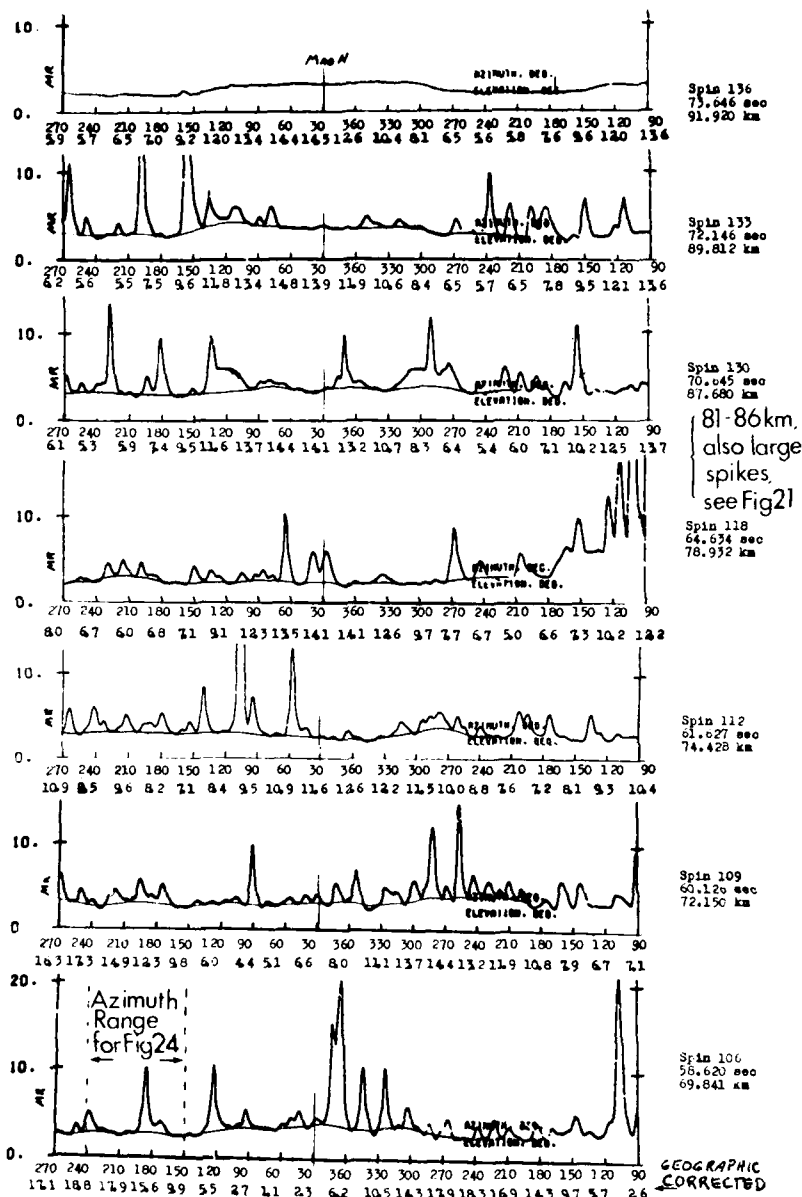
Figure 20. 4. 3μm radiometer azimuth-elevation spin
cycles on upleg of A18.219-1 showing
random appearing narrow noise spikes and
manually smoothed background level between
70 and 90 km. First evidence of the fluor-
escence-correlated increase is near 87 km.

79

A18.219-1   LINK 1   IRIG 10

LAMBDA 4.25   66.136 SEC.   81.150 KM.   SPIN 121

onset

(a)

A18.219-1

59.624 SEC   71.382 KM.   SPIN 108

3914Å →

←4.3μm

CORRECTED GEOGRAPHIC

(b)
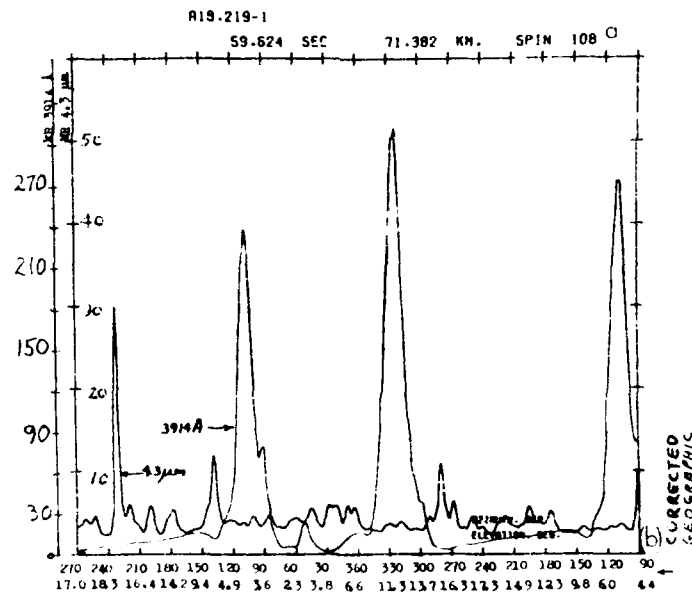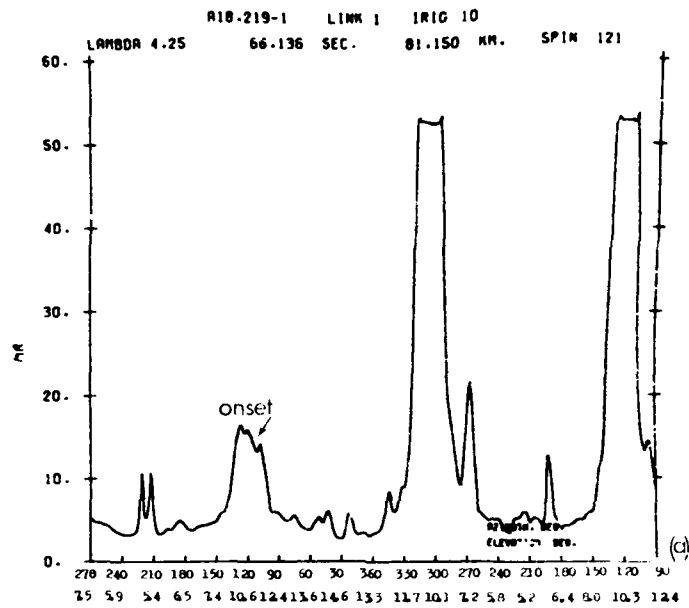
Fig. 21 a-b.   4.3μm and 3914 Å azimuth-elevation spin
cycles on upleg of A18.219-1 showing
a) onset of the intense thermal spikes at
81 km and b) representative (uncorrelated)
infrared and air-fluorescence signals at
low rocket altitude.

kR 3914 Å

μWR 4.3 μm

—50

270 —

—40

210 —

—30

150 —

—20

90 —

Spin 166
88.644 Sec
111.826 km

—10

4.3μm

3914Å

Corrected
Geographic

30 —

Mag
N

0 —

| 270 | 240 | 210 | 180 | 150 | 120 | 90 | 60 | 30 | 360 | 330 | 300 | 270 |
| 6.6 | 5.7 | 6.0 | 7.4 | 9.4 | 11.7 | 13.4 | 14.3 | 14.0 | 12.7 | 10.6 | 8.4 | 6.6 |

60 —   —10

Spin 161
86.145 Sec
108.659 km

3914Å

30 —

4.3μm

0 —

| 270 | 240 | 210 | 180 | 150 | 120 | 90 | 60 | 30 | 360 | 330 | 300 | 270 |
| 6.6 | 5.8 | 6.0 | 7.3 | 9.3 | 11.5 | 13.3 | 14.2 | 14.0 | 12.7 | 10.7 | 8.6 | 6.8 |
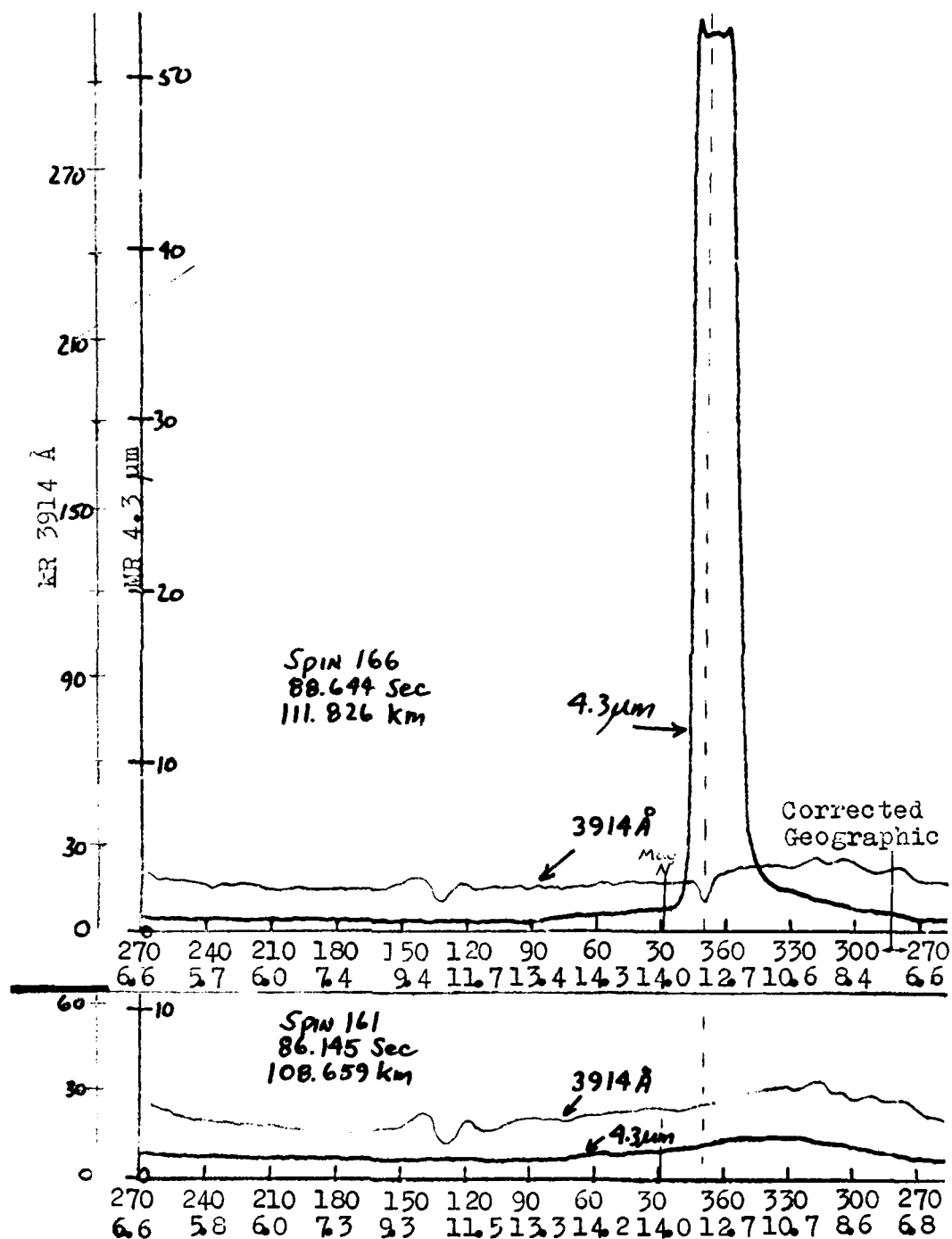
Figure 22. 4.3μm and 3914 Å azimuth-elevation spin cycles on upleg
of A18.219-1 showing reappearance of the off-scale spike
and partial obscuration of the air fluorescence near 340°
mag az.

81

- 81-86 km: two peaks offscale 20°-30° in azimuth repeating regularly at 90° and 270° geomagnetic az (Fig 21a shows their onset), in addition to the aforementioned random pulses;

- 91-110 km: no pulses of either type, the sporadic noise having disappeared abruptly in the trace starting at 91 km;

- 110-111 km: grow-in of a <u>single</u> isolated peak at 340° geomagnetic azimuth;

- 111-125 km: isolated offscale peak at 340° geomagnetic, with "shoulder" extending $\sim 120^{\circ}$ in az, general appearance as in Fig 22;

- 125-133 km: peak centered at 340° varying erratically in intensity between 10 MR and offscale;

- 133 km-apogee (190 km): isolated peak at 340°, decreasing in maximum intensity;

- (apogee-downleg, no isolated peak (as noted in Section 3) or noise spikes).

Our procedure in accessing these data was to estimate the baseline below the narrow random spikes (as shown in Fig 20) and ignore those az-el segments with the regularly-occurring spurious increases.

ALTITUDE PROFILES

Profiles of the atmosphere's radiance at low elevation angles in the 4.21-4.305μm wavelength band between 70 and 120 km altitude are plotted at 30° azimuth intervals in Fig's 23a-ℓ. Intensities below 91 km are expected to be upper limits because of the inherent inaccuracy
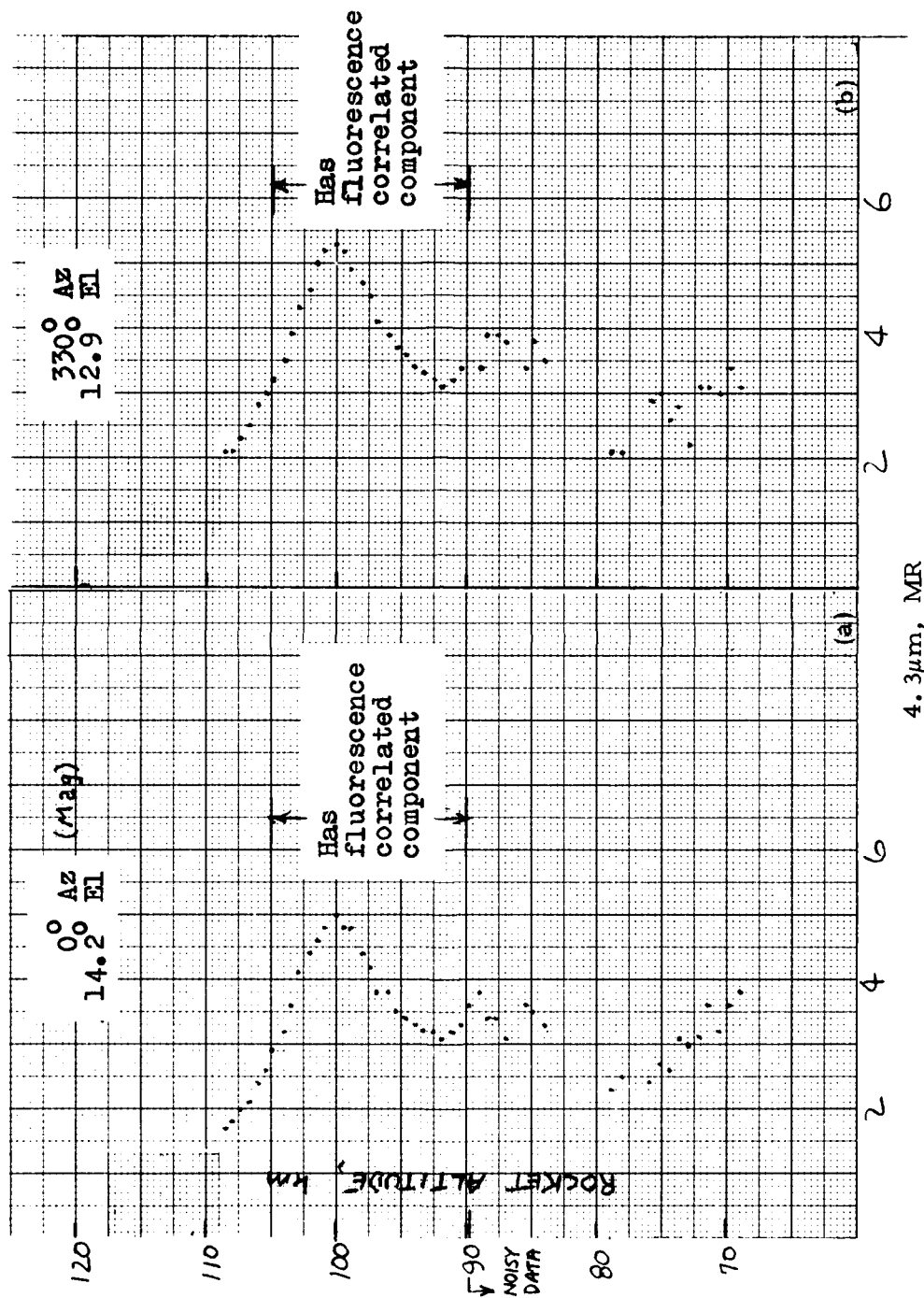
Figure 23a-ℓ   Altitude profiles of 4.3μm radiance measured at 30° azimuth intervals by
(pp 83-88)   the side-looking radiometer on upleg of A18.219-1. The 90° correction
                 to the azimuth angles described in Ref 4 has been applied.   Similar low
                 elevation-angle radiance profiles taken on downleg are in Fig 6 Ref 4.

270° Az
8.5° El

Has
fluorescence
correlated
component

23(d)

300° Az
10.8° El

Has
fluorescence
correlated
component

ROCKET ALTITUDE, Km

120
110
100
90 ← NOISY DATA
80
70

4.3μm, MR

23(c)

23(e)

23(f)

ROCKET ALTITUDE, km

150° Az
7.1° El

180° Az
5.8° El

4.3μm, MR

NOISY DATA

23(g)

23(h)

Has
fluorescence
correlated
component

90° Az
11.5° El

120° Az
9.3° El

4.3μm, MR

ROCKET ALTITUDE, Km

NOISY DATA

120
110
100
90
80
70

23(i)

23(j)

4.3μm, MR
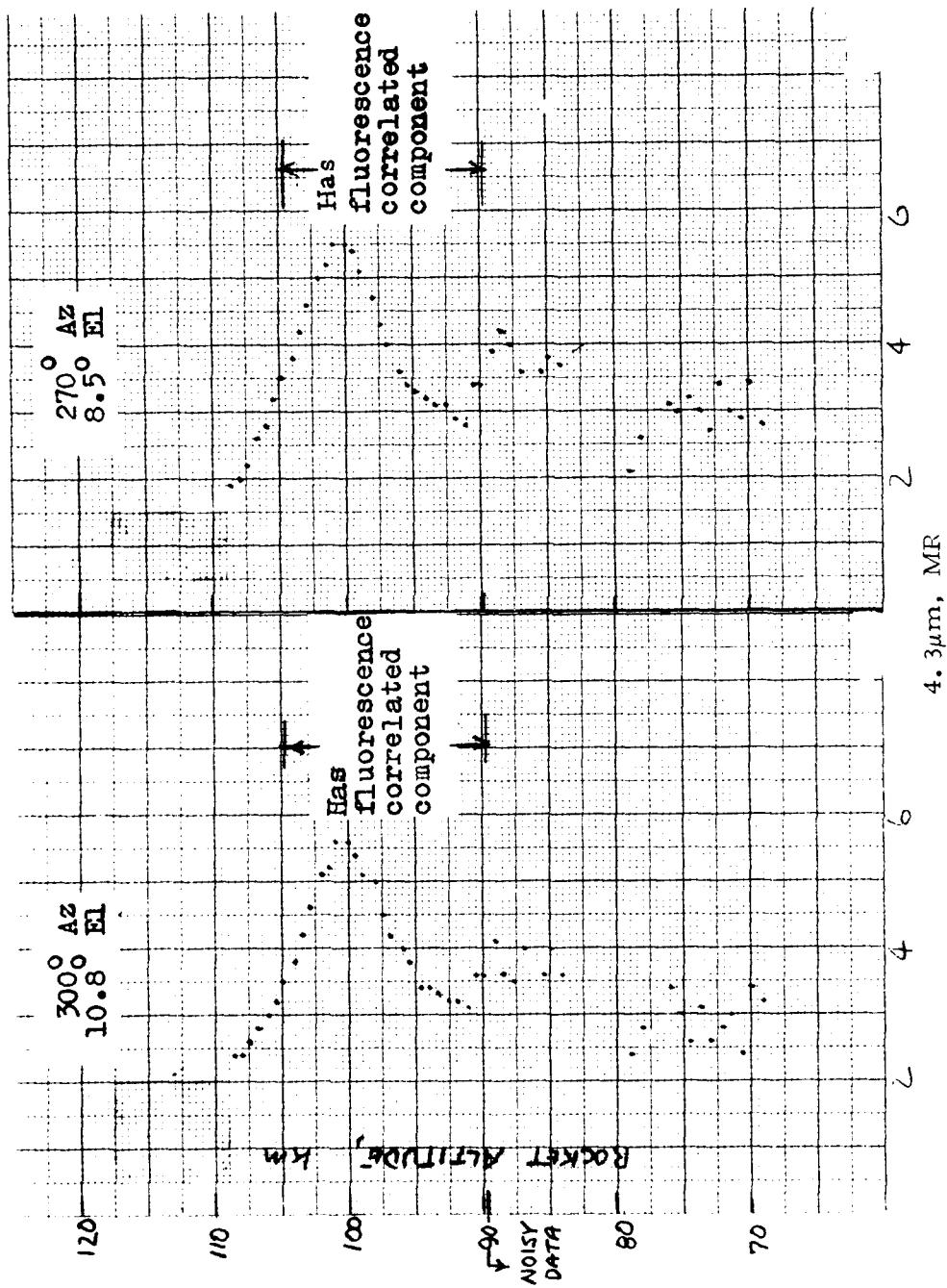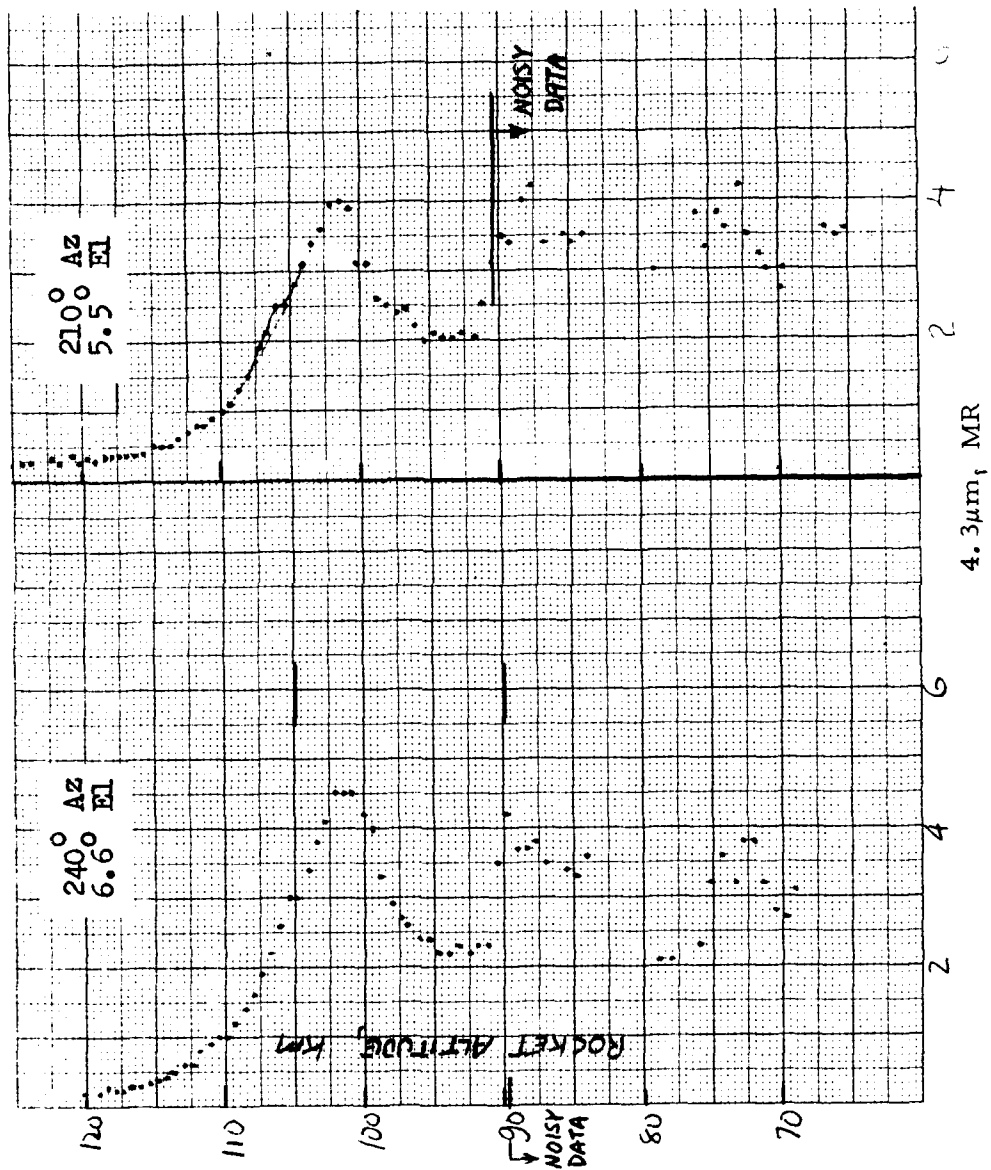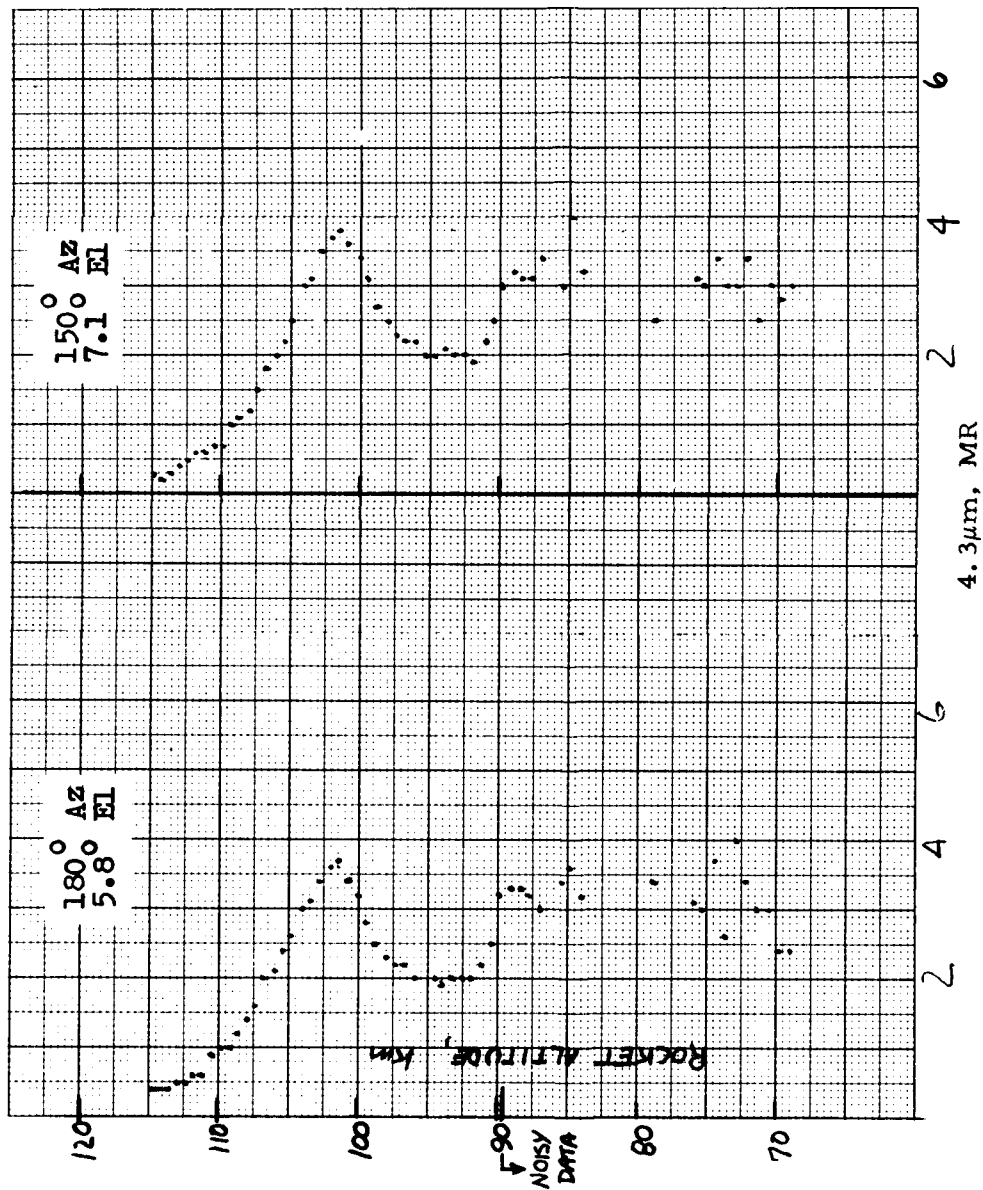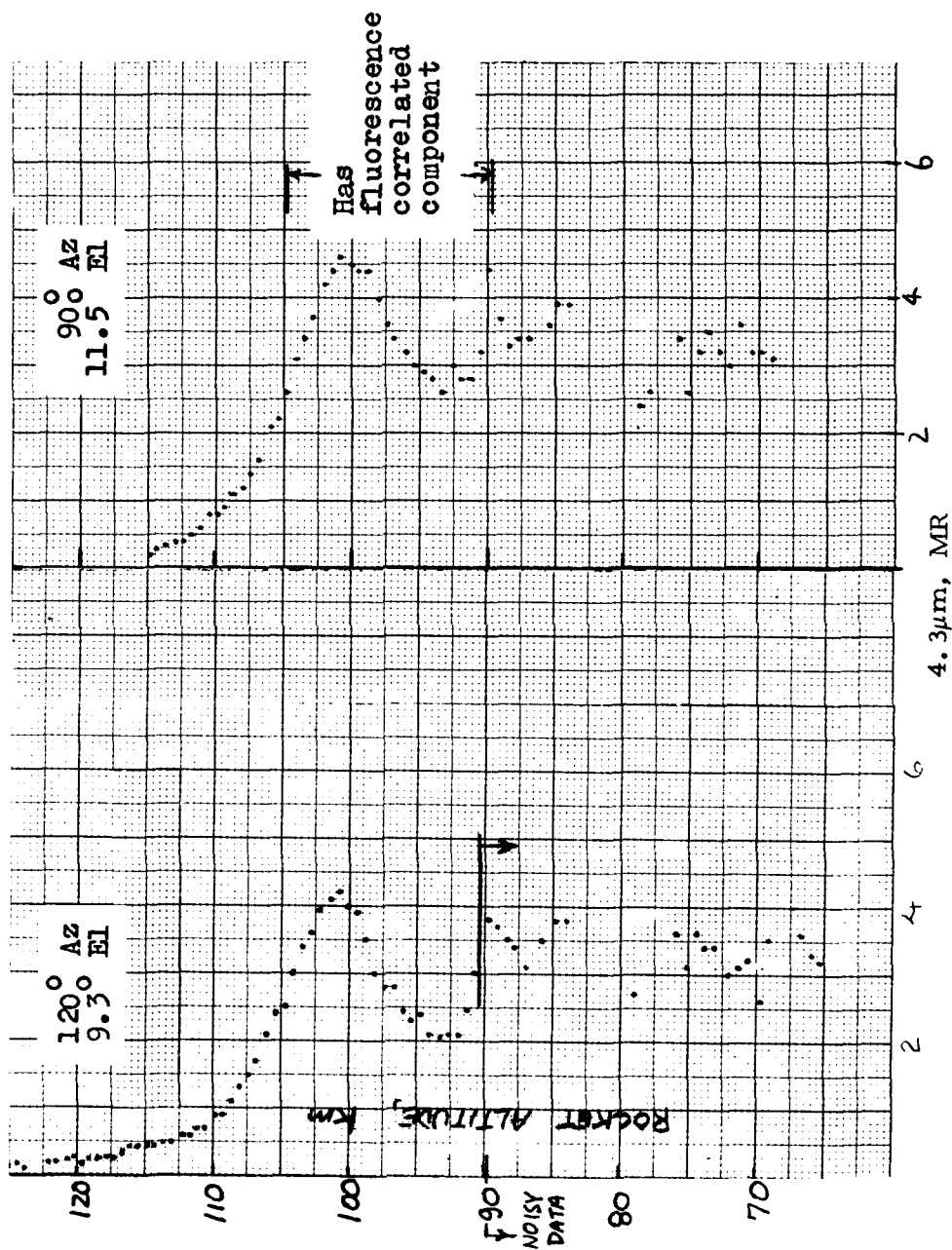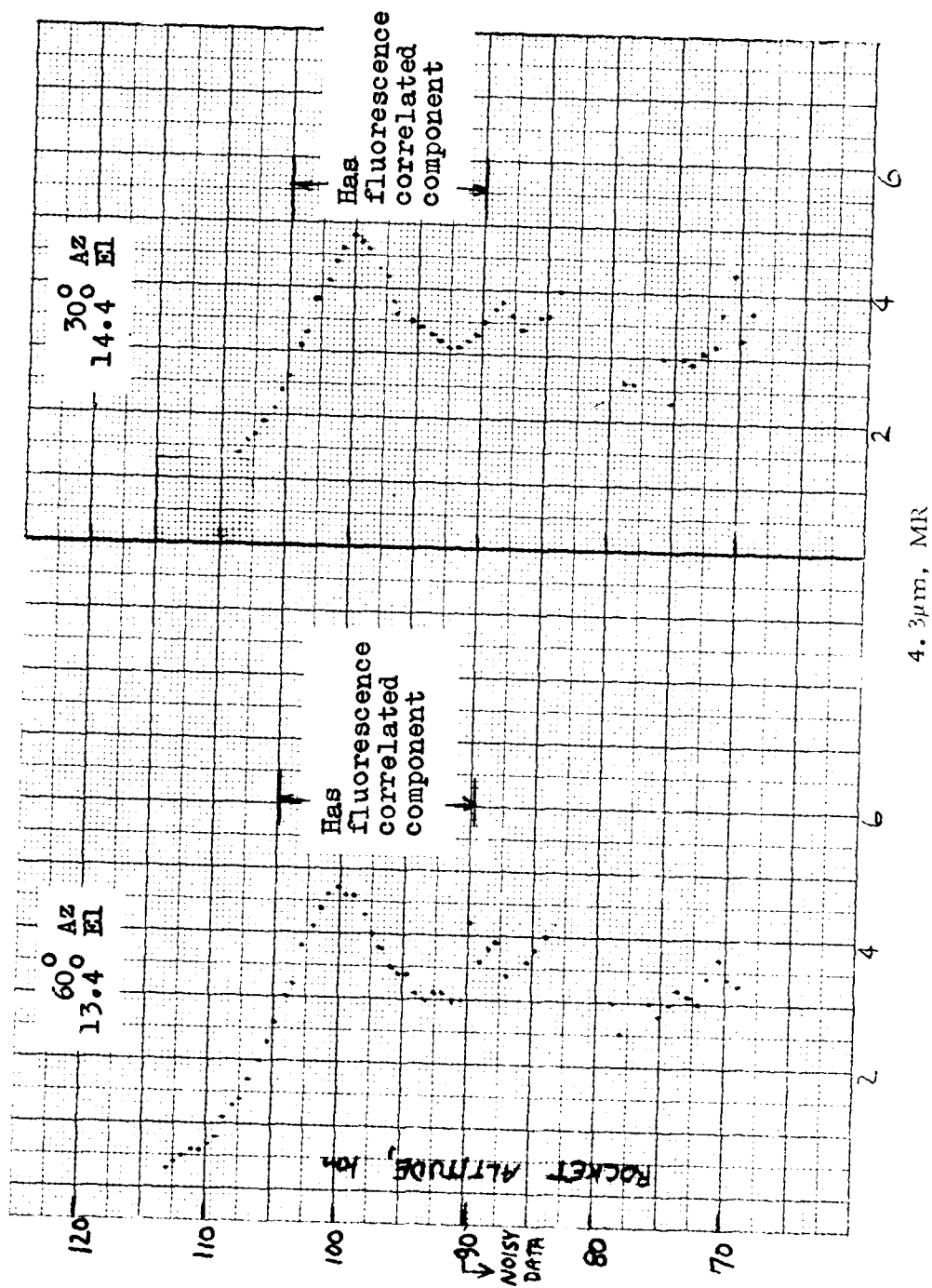
23(k)   23(ℓ)

in smoothing-out the noise (the closely packed spikes probably raise the baseline, as Fig 20 indicates). All the altitude profiles peak between 4 and 5.5 MR close to 110 km; the maximum photon fluxes are about half those of the downleg set (Fig 6 of Ref 4), and lie $\sim$ 3 km higher. Only one profile, that for 210° az -5.5°el, presents any reasonable indication of the altitude layering observed on downleg.

Fig 24 is a profile of the radiance distributions averaged over the (generally-southward) geomagnetic azimuth interval 210° to 120° for 70 - 91 km. As the atmosphere is optically thick to 4.26μm-band CO_2 radiation at these altitudes (as shown in Section I of Ref 4), minimal dependence on elevation angle (van Rhijn-like modulation) is expected. A "bulge" appears present between 80 and 90 km, which is perhaps related to the process of energy transfer from $OH^{\dagger}$ inferred from other HAES rocket data and described in Ref 26.
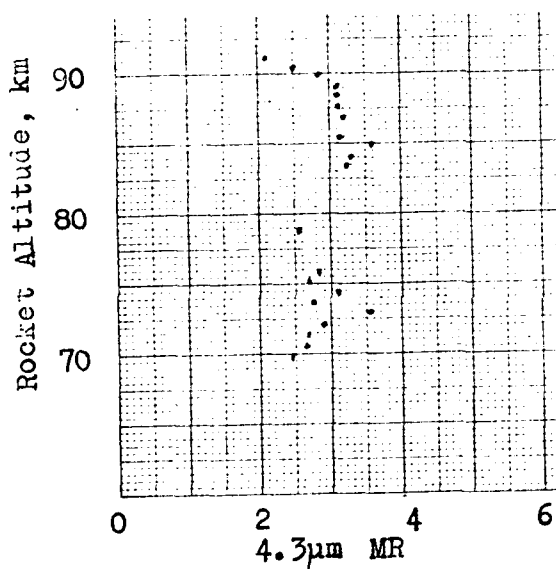
Figure 24.

70-91 km altitude profile of the smoothed, low-elevation 4.3μm radiance averaged over the geomagnetic azimuth range 210°-120° on upleg of A18.219-1.

Our omission of the segments of trace judged to be contaminated by the isolated peaks leaves some gaps in the altitude profiles between ~ 80 and 83 km, as well as above 110 km. We have also indicated in Fig 23 the altitudes and azimuths over which the 4.3μm-band signal has a component that correlates with air fluorescence measured by the photometers coaligned with the sidelooking radiometer.

RADIATION CORRELATED WITH AIR FLUORESCENCE

This component can be seen in the traces between 91 and 110 km rocket altitude over geomagnetic azimuths 270° to 90°, that is, in the half-scans north of the rocket. Typical data between 93 and 106 km, where the correlation is most marked, are shown in Fig 25.

The instruments' pointing geometry during this flight segment is illustrated in Fig's 26 (plan view of the trajectory and nearby auroral arcs) and 27 (view perpendicular to the trajectory plane). The half-maximum brightness contours on the strong (~ 80 kR 3914 $\overset{o}{A}$) arc ~ 35° N of PKR zenith were taken from the elevation angles measured by the photometers at PKR and FYU. During the $9\frac{1}{2}$-sec period spanned by Fig 25 the relative horizontal distance between the rocket and this arc's "center" field lines decreases from 64 km to 58 km (each moves about the same distance toward the other). Typical elevation angle of the radiometer and photometers in the direction of the heavily-irradiated region to the north is $11 - 14^\circ$, and the altitudes at which the fields intercept the narrow E-W-aligned arc are listed in Table 6.

The energy-deposition history in the area of the rocket's trajectory as inferred from the 3914 $\overset{o}{A}$ elevation scans from PKR (without correction for atmospheric scattering and with the assumption of a fixed altitude of energy deposition), is given in Fig 13 of Ref 16. Approximately $2\frac{1}{2}$ min before launch a bright (> 25 kR 3914 $\overset{o}{A}$) region began to form just north of the PKR zenith, and by the time of these measurements its intensity had increased to 90 kR. A few degrees south of the zenith the sky brightness was < 5 kR 3914 $\overset{o}{A}$ at $2\frac{1}{2}$ min before launch, and by
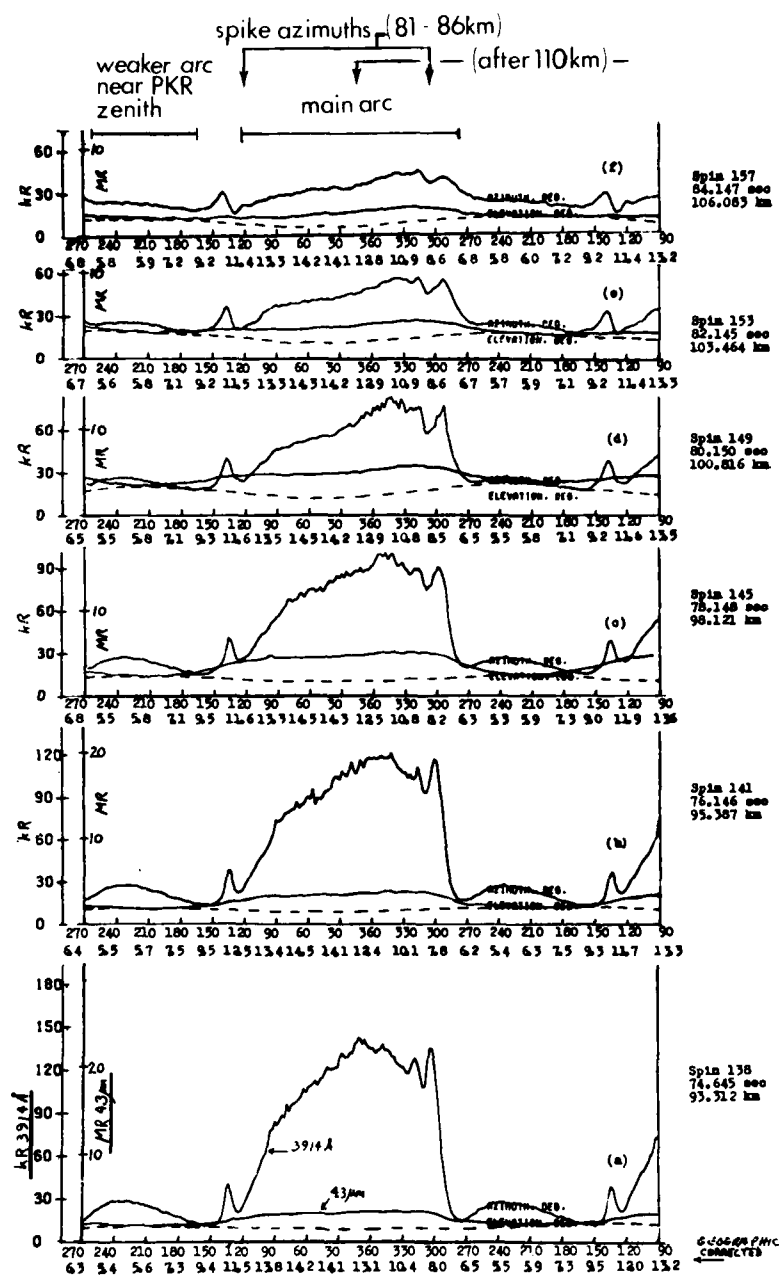
Figure 25. 4.3μm and 3914 Å azimuth-elevation spin cycles between 93.3 and 106.1 km on upleg of A18.219-1 showing the air-fluorescence correlated enhancements and estimated 4.3μm baselines (dashed lines). Azimuthal extent of the main arc N of the rocket, weaker arc near the PKR zenith, and locations of the intense thermal pulses before and after the data period are indicated.

PLAN VIEW

MAG N

PLANE OF FYU
PHOTOMETER 'S SCAN   ⊘FYU

$\frac{1}{2}$ MAX B
CONTOURS
(see Fig 27)

86 KR MAX
(80 sec)

20km

TRAJECTORY
PLANE

80 KM 381 SEC
100 KM 367 SEC

WEAK ARC
TO S

106KM 84 SEC
93KM 74 SEC

⊘PKR

PLANE OF PKR
PHOTOMETER'S SCAN
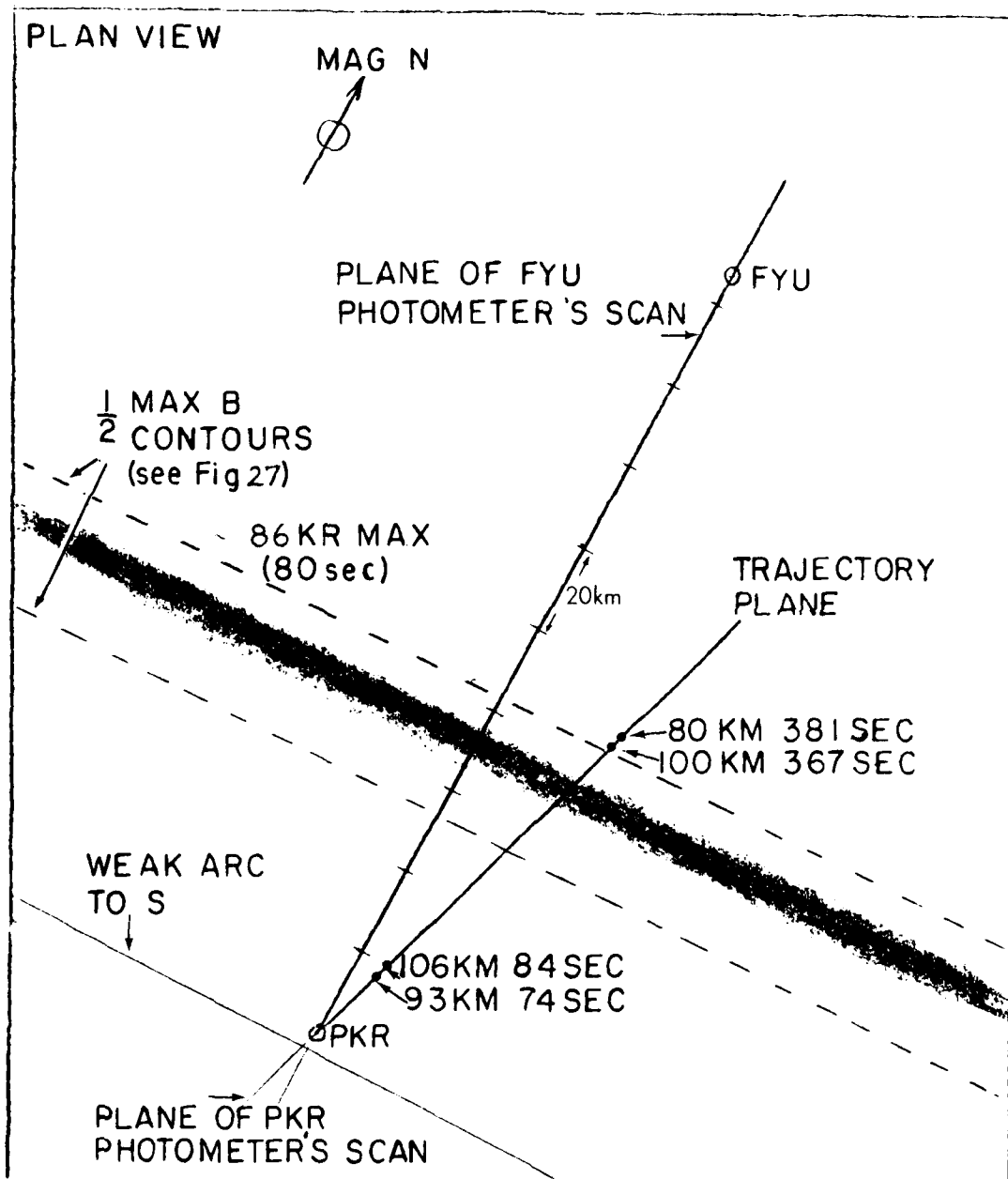
Figure 26. Plan view of A18.219-1's trajectory and locations of the strong
and weak arcs viewed by the sidelooking radiometer and photo-
meter on upleg. The arcs' positions refer to the data interval
of Fig 25.

92
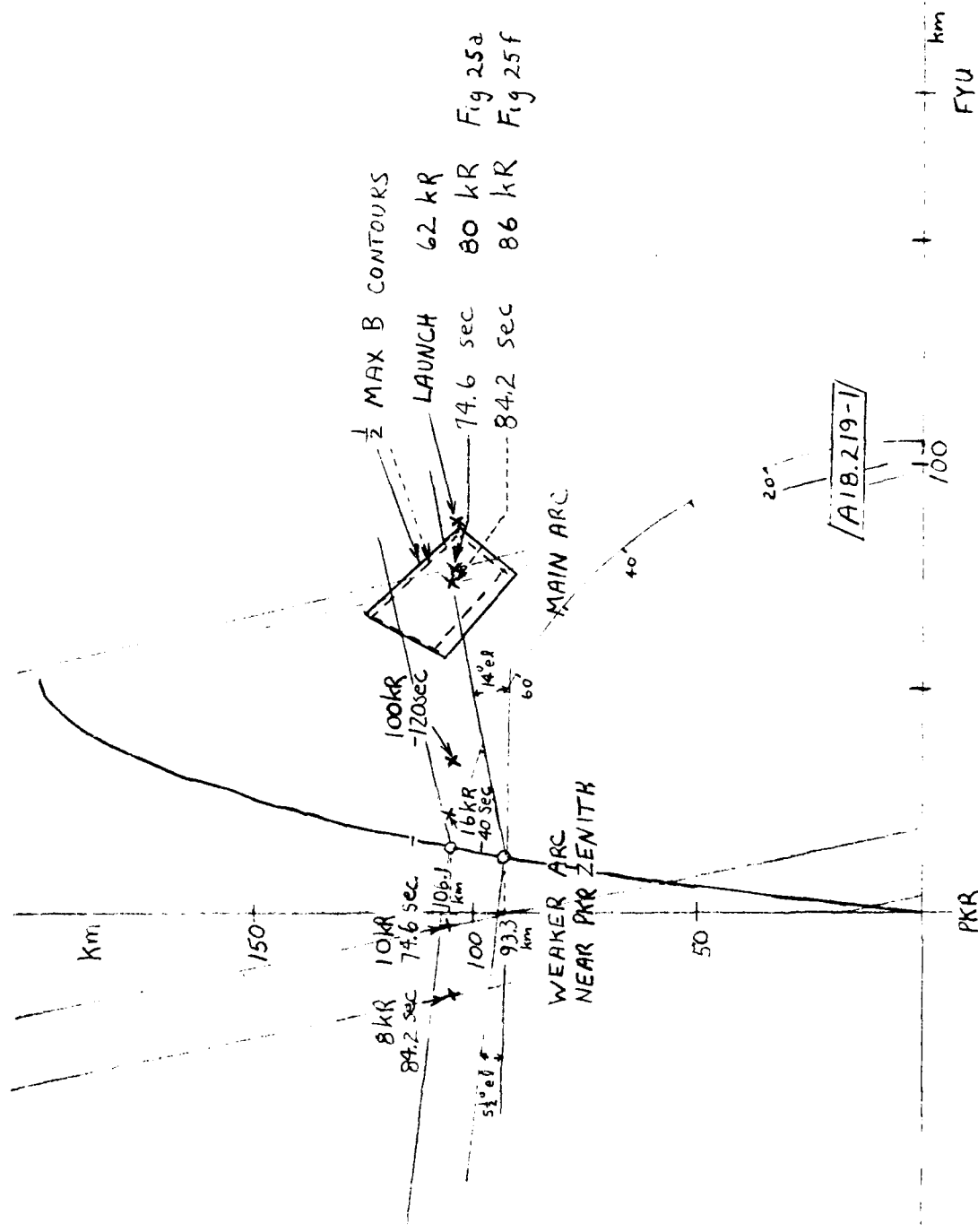
Figure 27. Trajectory plane projection of A18.219-1's flight path, with location of arc "centers" and 3914Å radiances measured by the PKR (USU) photometer. Centers are 105 km altitude intercepts at the zenith angle of peak arc intensity, and half-brightness points of the main arc are taken from the PKR (Ref 27) and FYU meridian data.

+60 sec the weaker arc shown in Fig's 26 and 27 had formed. Thus less predosing had occurred south of the rocket in the ~ 3 min before the measurements. In addition the weaker south-lying arc was being viewed at lower altitudes, as Fig 27 shows.

Fig 25 indicates the qualitative co-variation between the radiance in the 4.3μm band and the instantaneous energy input toward the north. The "match," including the similar upward slopes toward lower azimuths, appears sufficiently close to attribute the increase in infrared signal to radiation from the atmosphere rather than from the spurious object(s) in the radiometer field at nearby (higher and lower) rocket altitudes. The narrower characteristic azimuth dependence of radiation from this later source is shown in Fig's 21 and 22, and the position of the spurious maxima is indicated at the top of Fig 25.

To further investigate, and quantify this correlation, we first estimated the thermal contribution at each elevation angle, applying the assumption that the van Rhijn-like modulation at each upleg altitude should be similar to that at the same altitude on downleg. We fixed the maximum of this background radiance at the minimum radiometer elevation angle (5°, fortuitously at a geomagnetic az where little air fluorescence is present), and scaled the peak-to-valley ratio to match that measured on downleg. The resulting background estimates are shown as dashed lines in Fig 25.

We then constructed scatter plots of the excess 4.3μm radiance and 3914 $\overset{\circ}{A}$ fluorescence, which are shown in Fig 28 for the spin cycles at the highest and lowest rocket altitudes in Fig 25. The radiant intensities in Fig 25 were read at 15° azimuth intervals over the geomagnetic azimuth range 240° to 90°. The aforementioned "match" between the two signals is at least qualitatively borne out by the crossplots. (Correlation coefficients will be calculated when the full set of these plots has been completed.) Two least squares straight-line fits were made, one of which was forced to pass through the origin (the 4.3μm data are uniformly weighted, and the 3914 $\overset{\circ}{A}$ data are assumed to have negligible experimental uncertainty). At the lower altitude the slope of the regression line through the origin is twice that of the conventional best-fit line, while at the higher

94
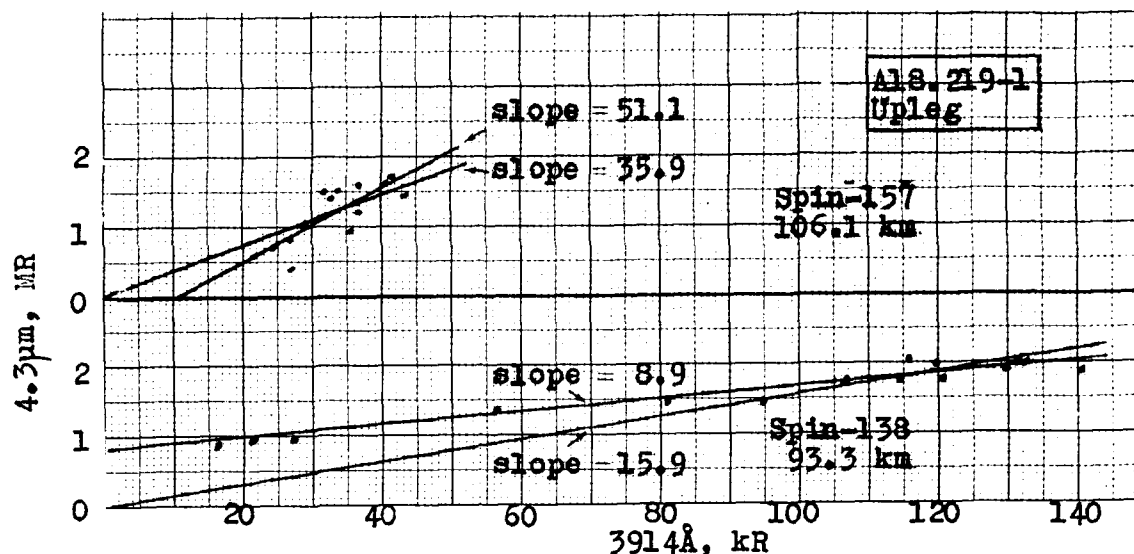
Figure 28. Scatter plots of 4. 3μm excess and 3914 Å
intensities for two of the spin cycles in
Fig 25. The straight lines are least-
squares fits with uniform weighting of the
4. 3μm data, one of which is forced to pass
through the origin.

altitude the latter slope is larger than the former. The slopes, or
apparent ratios, increase with rocket altitude, as would be expected
from the original data in Fig 25. The excess 4. 3μm/3914 Å ratios are
also in general larger away from the geomagnetic meridian, where the
radiometer's field intercepts the arc at higher altitude (Table 6). These
increases are in the direction expected if the excess radiation is being
partially absorbed by the intervening atmosphere (they are of course sub-
ject to alternative interpretations). The log of slope of best-fit lines is
plotted against CO_2 column density in the trajectory plane in Fig 29 ; a
straight-line fit would suggest linear attenuation (which in any case is
not expected for all the rotational lines of CO_2 resonance band). The
slope of the unforced best-fit line averages 37 in the two highest-altitude
scans in Fig 25, a photon ratio at least an order of magnitude greater
than that reported from the downleg data (Section II of Ref 4).

95
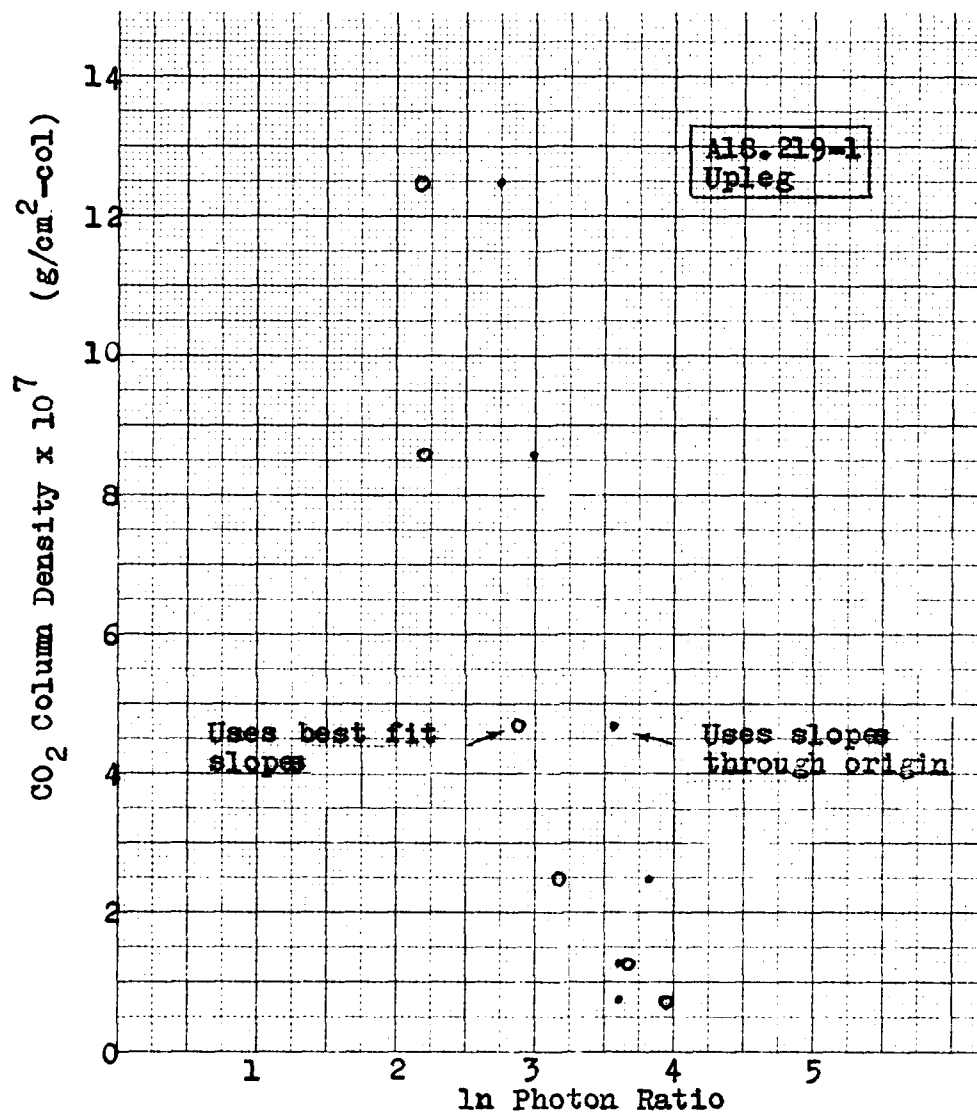
Figure 29. Plots of CO_2 column density between the rocket and the arc (in the trajectory plane) against $\ln$ (excess $4.3\mu m)/(3914$ Å) photon ratio determined from the slopes of best-fit lines as in Fig 28. The data refer to the altitude range 93-106 km on upleg of A18.219-1.

Table 6. Altitudes at which A18.219-1's sidelooking instruments' fields of view intercept the arc N of PKR

Time, sec	Rocket Altitude, km	Horizontal Distance (rocket to arc centers field lines in meridian), km	Intercept Altitude of fov with Arc Center's Field Lines, km		
			360°, 14.1°	45°, 14.0°	315°, 11.8°
84.2	106.1	58	120	125	122
79.0	99	61	$113\frac{1}{2}$	119	116
74.7	93.3	64	$108\frac{1}{2}$	114	111

OBSCURATION BY THE RADIATING OBJECT

The occultation of 3914 Å-band radiation shown in Fig 22 is compelling evidence that a solid object is responsible for the large regularly-recurring 4.3μm-band signal appearing above 110 km. A similar downward excursions is present in scans from the rocket's other sidelooking photometers, while the traces from the coaligned 2.42 - 3.1μm radiometer show very large or offscale pulses at the same (single) eℓ-az and rocket altitudes as the 4.3μm radiometer. Self-emission by the object at visible wavelengths, or reflection off it, is below the threshold of detectability. The limited and essentially-constant angular subtense of the spurious signal is further evidence that this radiator is a solid "warm" body rather than a (diffusing) gas cloud of the type invoked to interpret the altitude profile of 2.8μm-band radiation on downleg (Ref 16). The aforementioned low amplitude "shoulder" in the 4.3μm radiance traces is probably due to the non-zero response of the radiometer at off-axis angles (see Fig 20 of Ref 3).

The apparent intensity at 3914 Å drops by as much as 60% during the period of obscuration between 110 and 120 km. Evidence of blocking is also present in the eℓ-az traces for 81-86 km, in which two infrared-radiating objects 180° apart come into the instrument field. Thus the object at times fills more than half the 5°-circular field of the photometer (again assuming no reflections or short-wavelength emission). Some obscuration of the background aurora is detectable over about 10° in azimuth. From model deconvolutions of these downward-going pulses, further information about the angular extent of the objects near the rocket — and thus about their source — could be derived.

SUMMARY AND RECOMMENDATIONS

As was noted in Ref 4, the data from multi rocket A18.219-1 contain the only direct information available about the flux of 4.21 - 4.305μm radiation at low elevation angles in the disturbed atmosphere above ~ 86 km. Fig 6 of Ref 4 (downleg) and 23 of this Section (upleg) constitute a coherent set of "limb-view" 4.3μm-band altitude profiles

of two neighboring regions of the auroral-latitude ionosphere. The radiances measured on upleg between 90 and 110 km rocket altitude have a component associated with intense air fluorescence, which from experience with similar multi rocket data is expected to come from a near-stable, persisting auroral arc some 60 km to the north. This near-prompt radiation, whose intensity is comparable to the scattering of earthshine by CO_2 molecules, should perhaps be subtracted from the total $4.3\mu m$-band signal when comparing upleg and downleg altitude profiles.

Noise present in A18.219-1's radiometer data turns out to be less troublesome than originally anticipated, and in fact photometry and radiometry of the regularly-appearing spurious peaks carries information about their origin that may be useful in designing future rocket investigations of infrared sky backgrounds. It should be noted that the upleg data from the $2.42-3.11\mu m$ sidelooking radiometer, which exhibit about the same sporadic noise levels, have not yet been reduced and analyzed. The azimuthal dependence of the regularly-occurring spurious $2.8\mu m$ signal should be investigated to verify that the much broader $(\sim 240°)$ $4.3\mu m$ enhancement between 90 and 110 km has little or no contamination from this source. The discrepancy between the upleg and downleg $2.8\mu m$ radiance levels in the zenith direction has been the subject of considerable discussion (Ref 16, and p329ff of Ref 5).

The upleg profiles at low elevation angles also show an increase between ~ 80 and 90 km rocket altitude that may be preliminarily attributed to the $OH^{\ddagger} \rightarrow N_2^{\ddagger} \rightarrow CO_2^{\ddagger}$ airglow mechanism of Ref 26.

The excess $4.3\mu m$ emission has a smoother surface radiance structure than the N_2^{+}-band fluorescence (it is convolved with the instrument's $6°$ field, which subtends ~ 6 km at the arc). Its apparent "yield" — or intensity ratio to that of simultaneously measured air-fluorescent emission — depends strongly on rocket altitude, and has a

maximum an order of magnitude greater than that inferred from the enhancements observed in downleg. This difference, the failure of the lower-altitude upleg data (for example Fig 21b) to show 4.3μm increases, and the reason that the broad arcs nearby on downleg produced no detectable enhancements, are not explained by the limited data reduction and analysis performed to date. The actual dependence of this emission on altitude of energy deposition, previous dosing, and air mass to the radiometer can be better understood after the data from all the upleg scans have been assessed and the contribution of the spurious noise source(s) − if any − more thoroughly investigated.

No "near-prompt" sky background enhancements have been resolved in any of the HAES zenith-radiometry data, perhaps because side views of narrow regions of energetic particle precipitation (Fig 27) provide a more favorable projection than altitude-integrating views. In any case these preliminary results from A18.219-1 can be interpreted as indicating that surveillance systems that view against the atmosphere's limb will encounter more spatial variation in 4.2-4.3μm radiance than near nadir-viewing systems. The zenith data, as they were available earlier, provided impetus and information for developing the current model of 4.3μm-band radiation in the disturbed atmosphere; these sidelooking data, in their present state of assessment, do not appear consistent with this model.

REFERENCES

1. I. L. Kofsky et al., Data Reduction and Auroral Characterizations for ICECAP, HAES Report No. 4, DNA 3511F (10 Apr 75).

2. I. L. Kofsky, R. B. Sluder, and C. A. Trowbridge, Data Reduction and Auroral Characterizations for ICECAP II, HAES Report No. 27, DNA 3789F (25 Oct 75).

3. I. L. Kofsky, D. P. Villanucci, and R. B. Sluder, Data Reduction and Auroral Characterizations for ICECAP III, HAES Report No. 59, DNA 4220F (31 Jan 77).

4. I. L. Kofsky, D. P. Villanucci, and G. Davidson, Assessment and Evaluation of Simulation Data, HAES Report No. 69, DNA 4303F (15 Nov 77).

5. A. T. Stair Jr., and J. C. Ulwick (jt. ed), Proceedings of the HAES Infrared Data Review, AFGL-OP-TM-05 (Jun 77).

6. R. J. Huppi and J. W. Reed, Aircraft Borne Measurements of Infrared Enhancements During ICECAP 1975 and 1976, HAES Report No. 68, AFGL-TR-77-0232 (28 Sep 77).

7. I. L. Kofsky, J. D. Geller, and C. A. Trowbridge, Sky Background Measurement Program, AFCRL-70-0012 (PhM-101-69), (30 Nov 69).

8. R. B. Sluder et al., Aircraft Program for Target, Background and Sky Radiance Measurements, AFGL-TR-78-0123, Scientific Report No. 1 (18 May 78).

9. A. Vallance Jones, Space Sci. Rev's 15, 355 (1973).

10. F. DelGreco and J. Kennealy, private communication, (4 Jan 78).

11. F. S. Acton, Analysis of Straight Line Data, Dover Publications, New York, 1966.

12. D. H. Archer, Requirements for Improved Infrared Prediction Capability, HAES Report No. 78, DNA 4585F (30 Apr 78).

13. C. Bohne, L. Harkless, and E. Dunbar, HIRIS Reflight, HAES Report No. 65, DNA 4337F (10 Apr 77).

14. A. T. Stair Jr., J. W. Rogers, and W. R. Williamson, HIRIS Experiment, Quick Look Data Report, HAES Report No. 46 (15 Apr 76).

REFERENCES (Continued)

15. G.J. Romick, Report on the Geophysical Description and Available Data Associated with Rocket PF-SGT-116 (IC 630.02-1A), HAES Report No. 63, AFGL-TR-77-0073 (Mar 77).

16. A.G. Hurd et al., Comparison of ICECAP and EXCEDE Rocket Measurements with Computer Code Predictions, HAES Report No. 61, AFGL-TR-77-0060 (15 Feb 77).

17. D. Baker, private communication (1977).

18. A.E. Belon, G.J. Romick, and M.H. Rees, Planet. Space Sci. 14, 597 (1966).

19. C.S. Deehr et al., J. Geophys. Res. 81, 5527 (1976).

20. T.M. Watt, HIRIS Experiment – Chatanika Radar Results, Technical Report 9, DNA 4429T (Jan 77).

21. R. Vondrak and R. Sears, J. Geophys. Res. 83, 1655 (1978).

22. J.E.A. Selby and R.A. McClatchey, Atmospheric Transmittance From 0.25 to 28.5μm: Computer Code LOWTRAN 3, AFCRL-TR-75-0255 (7 May 75).

23. C.S. Miller and R.H. Johnson, Radiance and Irradiance Measurements Within Free Atmospheric Clouds, Technical Operations Research, Final Report No. TO-B 65-37 (30 Apr 65).

24. W.F. Grieder and L.A. Whelan, Geometric Aspects of Rocket Photometry, HAES Report No. 41, AFGL-TR-76-0046 (Feb 76).

25. J.B. Kumer, Further Evaluation of ICECAP Auroral 4.3μm Zenith Radiance, HAES Report No. 57, DNA 4260F (Oct 76).

26. J.B. Kumer et al., J. Geophys. Res. 83, 4743 (1978).

27. Aeronomy Observatory, Ground Support Data Report in Support of Black Brant 18.219-1 Flight, Utah State University, (2 Sep 74).

APPENDIXES

TABLE OF CONTENTS

ABSTRACTS AND EXPLANATORY NOTES

Some minor changes from PhotoMetrics' original communications to AFGL and DNA have been made for clarity in Appendixes II, III, IV, and V.

I -- Test Plan for Structure-Sources Measurements

A detailed overview of the aircraft-based investigation and its application to determining surveillance systems performance following nuclear engagements, flight plans and instrument specifications, and procedures for reducing and interpreting the narrow-angle radiometry data to validate (and determine parameters for) code models of SWIR background emission, are presented. Note: The reference numbers refer to the list on page 144.

<u>II</u> --   Infrared Sky Backgrounds and Potential Aircraft
Flight Plans for 26 Feb 79 Total Solar Eclipse

Sources of sky radiance at the short-wavelength infrared wave-
lengths within the eclipse umbra are reviewed, and suggestions for
measuring zenith intensities of the OH Meinel ($\Delta v = 1$) and O_2 $^1\Delta$ air-
glows during and near totality are presented. Flight plans for AFGL's
IR-Optical instrumented aircraft are included.

<u>III</u> --   Infrared Emission Produced by FIREWHEEL

The use of NKC-135 A/C 53120's instruments to measure visible
and SWIR emission from the artificial aurora that is expected to result
from an explosive release of Ba + Li in the magnetosphere is suggested.
The measurements have broad application to investigation of the phenom-
enology of nuclear-explosions at magnetosphere altitudes.

<u>IV</u> --   Potential Applications of Space Shuttle's Laser Radar

Seven (NASA) Candidate Shuttle Lidar Measurements that provide
altitude profiles of reactive species useful in communications-survivability
investigations are listed. Some of these measurements also apply to
determining infrared sky backgrounds. Specific laser/detector types
and expected operational feasibility dates are included.

<u>V</u> --   IR Remote Sensing of D- and E-Region Conditions

The capability of OPR's existing infrared radiometers and spectro-
meters for remotely sensing neutral species column-concentrations,
profiles, and temperatures is reviewed. Perceived applications of the
several infrared-emitting species in ionosphere diagnosis are discussed.

<u>VI</u> --   OH $^2\tau$ Vibrational Fundamental Spectra

Results of calculations with PhotoMetrics AIRSPEC computer
program of OH Meinel-band fundamental airglow spectral intensities
are presented.

APPENDIX I

TEST PLAN

Aircraft Program for Determining Short Wavelength-Infrared
Spatial Structure and Sources in Energetic
Particle-Excited Air

Contents

1. Purpose and Overview

2. Systems Application

3. Current Status of Information on SWIR Structure
and Sources

4. Aircraft Instrumentation

5. Flight Plans

6. Interpretation of the Radiometry Data

1. Purpose and Overview of the Investigation

The NKC-135 aircraft-based measurements described here are
designed to determine the aerochemical and atmosphere-dynamics
mechanisms that result in spatially structured emission at wavelengths
~2.7 to 3.0μm from energetic-particle and -photon irradiated air at
altitudes ~80 to 140 km. Information from the program will be applied
toward validating capability for predicting, with the help of computer
code models, performance of satellite borne sensors operating against
the persisting sky background radiations excited by nuclear explosions.

The simulating source of input power is the energetic (~5 keV)
electrons that precipitate into the upper atmosphere at high latitudes
in association with magnetospheric substorms. Spatial distributions
of flux and deposition altitudes of these charged particles are measured
from the air fluorescence they excite at visible wavelengths, that is,
the optical aurora. The species ionized and excited by direct electron
impact and secondary processes react with ambient molecules and atoms,
producing chemiluminescence that is measurable against other natural
2.7 - 3.0μm atmospheric emissions from subsonic jet aircraft altitudes
(10 - 12 km).

The spatial resolution of the radiance measurements, 2/3 km horizontally, allows infrared output to be correlated with particle-energy input at the scale of interest to future spaceborne sensors. Characteristic times for grow-in and decay of IR emission after energy has been deposited are determined from the temporal correlation between visible fluorescence and infrared chemiluminescence, and from sequential sampling with three spaced radiometers. Procedures for determining aeronomical process and parameters from the narrow-angle radiometer and photometer data are outlined in subsection 6.

In addition the radiating species are identified and their upper-state population distributions measured by high-resolution interferometric spectrometry of the infrared emissions. The visible-infrared correlation and emitting-species information can be applied to assess directly the spatial distributions of IR background excited by past nuclear explosions in the atmosphere, by reference to existing silver halide photographic records of their long-lived skyglows.

The goals of the aircraft program can be summarized as

(a) establish the spatial-temporal correlation of $2.7 - 3.0\mu m$ emission with energy deposition in the atmosphere at the scale of structure detectable by future sensors, and

(b) determine the sources of structured infrared emission to permit effective scaling of the simulation data, by DoD phenomenology and systems codes, to nuclear interchange scenarios.

2. Systems Application

Infrared camera-radiometers will soon have sufficient sensitivity to operate under natural background limited conditions

even when viewing small areas in segments of individual molecular emission bands. Improvements in infrared detectors, cryocooled-telescope technology, and methods for processing image data have combined to give scope to planning of satellite-borne surveillance sensors for identifying and tracking very low intensity military targets from their characteristic spatial, temporal, and spectral "signatures." The performance of sequentially-scanning sensor arrays is sensitive to the spatial distribution of scene radiance, while that of continuously-staring cameras is considered to depend more on the temporal variations in the background (provided that the space-borne platform is sufficiently stable that no time-space mixing occurs). A recent detailed systems analysis shows that increased "noise" in the infrared spatial structure that results from certain nuclear explosions can significantly impair effectiveness of some system designs.

Consequently, an understanding of the aerochemical (and dynamical) processes by which energy deposited in the atmosphere by nuclear bursts produces infrared sky background radiation is needed for evaluating IR surveillance systems designed for transattack operation. The excitation-deexcitation mechanisms must be known to permit simulation data on spatial-temporal correlations to be extrapolated to the energy deposition altitudes (that is, air densities) and dosages of nuclear explosions, and the different projections of satellite cameras. Past DNA-sponsored field and laboratory measurements (as outlined in subsection 3, following) have provided important information about the "lumped parameter" chemiluminous yield of $2.7 - 3.0 \mu$m photons, as well as data of moderate resolution on the correlation of this radiation with visible air fluorescence. The present aircraft program will improve the resolution to the fields of view and framing times of future satellite sensors, and (as noted) determine the infrared emission processes that result in structure different from that of the initial energy input. As also noted, parameters are derived from these structure-sources measurements for

107

input to DoD computer codes that effect the predictions of surveillance systems performance under conditions of nuclear warfare.

3. Current Status of Information on SWIR Structure and Sources

The aircraft measurements will improve by an order of magnitude the resolution of infrared-visible spatial and temporal correlation, and of the emission spectrum of the irradiated upper atmosphere in the short-wavelength infrared (SWIR) region. To put this present investigation in perspective, results of previous aircraft and other DoD SWIR measurement programs are briefly reviewed.

AFGL's IR/Optical Flying Laboratory (NKC-135 S/N 53120) measured zenith SWIR radiance on 14 ~5 hr flights in and near the auroral oval, in conjunction with the DNA-sponsored HAES ICECAP 1975 and 1976 field programs. An operating plan for the 1976 missions containing background material useful for understanding the design of the present test series is in Appendix I of Ref 2. The prime instrument was a single-channel 2.8μm filter radiometer with LN_2-cooled chopper and 10° circular field of view, with which an air-fluorescence (N_2^+ First Negative band) photometer was coaligned. Seven further such flights were made in September 1977, also near Poker Flat Research Range, Alaska. The planning for and partially-evaluated results from the 1975-1976 measurements have been documented in High Altitude Effects Simulations-series and other reports as listed in Table 1, and data from the 1977 flights are now being reduced.

The radiometer (FWHM 2.76 - 2.91μm in 1975, 2.83 - 3.04μm in 1976 and 1977) measured skyglow enhancements that were found to be proportional to the instantaneous rate of column energy deposition by energetic charged particles, within its low spatial-temporal resolution and within a range of $\pm$ about a factor 2. The average "equilibrium" effective SWIR yield derived to date (see in particular Section IV of Ref 2) is close to the average measured with a sidelooking rocket radiometer that viewed near-stable auroral arcs from coaltitude

Table 1. Reports on HAES NKC-135 Aircraft Measurements
of Auroral Particle-Associated 2.8μm Emission

1975 Flight Missions

— Instruments, flight paths, data periods,
coordination with facilities at Poker
Range   Ref 1, Section V

Results from Flight 75-4 (10 Mar 75)

— Preliminary assessment   Ref 1, Section III
— Final evaluation   Ref 2, Section IV

- - - - - - - - - - - -

1976 (and 1975) Flight Missions

— Operating Plan   Ref 2, Appendix I
— Instruments, data periods, coordination
with DNA 617 radar   Ref 2, Section VI
— Data from Flight 76-9 (07 Mar 76)
2.8μm-region synthetic spectra &
filter passbands   Ref 3, p207 ff
— Data from Flights 75-2, -4, -5, -7 &
76-5, -9, -10, -16; information on
instruments, resolutions to photon ratios   Ref 4
— 12-channel photometer data for determina-
tion of deposition altitudes, flight paths   Ref 5, Section VI

- - - - - - - - - - - -

Background for Interpretation

— Synthetic Spectra for NO + OH + thermal
radiation, atmosphere transmission   Ref 1, Section I

— Optical Method for determining auroral   Ref 2, Appendix II
altitudes   Ref 6

Ref 1. I. L. Kofsky et al., Data Reduction and Auroral Characterizations
for ICECAP II, HAES Report No. 27, DNA 3789F, Oct 75.

Ref 2. I. L. Kofsky et al., Data Reduction and Auroral Characterizations
for ICECAP III, HAES Report No. 59, DNA 4220F, Jan 77.

Ref 3. Proc. HAES Infrared Review (ed. Stair, Ulwick), AFGL-OP-
TM-05, Jun 77.

Ref 4. R. J. Huppi & J. W. Reed, Aircraft Borne Measurements of
Infrared Enhancements During Icecap 1975 and 1976, HAES
Report No. 68, AFGL-TR-77-0232, 28 Sep 77.

Ref 5. I. L. Kofsky et al., Assessment and Evaluation of Simulation
Data, HAES Report No. 69, DNA 4303F, Nov 77.

Ref 6. R. Vondrak & R. Sears, Comparison of Incoherent-Scatter
Radar and PhotoMetric Measurements of the Energy Distribution
of Auroral Electrons, J. Geophys. Res. 83, 1655 (1978).

(Section II of Ref 2), especially if the assumption is made that the radiation is the first vibrational overtone sequence of the NO molecule. With this assumption the yield is also consistent with the chemiluminous efficiency inferred from laboratory measurements by AFGL's COCHISE group (Ref 3, p 250 ff).

On the other hand the aircraft results themselves, and those from other ICECAP rocket measurements on naturally-and artificially-excited air (by EXCEDE), show substantial inconsistency. The aircraft SWIR intensities have factor-of-two variability about the mean when referenced to the immediate, local input of energy into the radiating volume (see for example Ref 4); and the data from zenith-viewing spectroradiometers on several rockets show even greater variations (Ref 3, p 404 ff). These results have been interpreted as due to the contribution of previous dosing, and to molecular radiation mechanisms other than those that produce NO, among them vibra-luminescence of CO_2 (Ref 3, p 327 ff; Ref 7). Thus the predictive capability of present DoD SWIR code models is open to question.

Furthermore, spectra of energetic particle-excited air have not had sufficient resolution to allow identification of the species radiating in the 2.7 - 3.0μm region. The 10 cm^{-1} resolution of the high-sensitivity interferometer provides about 6 independent sampling points between peaks of P- and R-branches in NO $\Delta v = 2$ bands.

The footprint on the typically 105-km emission altitude of the radiometers and photometers used to date is 16 km. The aircraft's forward motion causes this horizontal projection of the instrument fields to be traversed in about 1 min. Since the signal/noise ratio of the air fluorescence-associated infrared emission is only of the order of 4 in an integrating time of $\sim$1/2 min, differences in spatial characteristics of this component at less than the 16 km intercept scale cannot be unambiguously distinguished. Similarly the existing aircraft data do not resolve the contribution to infrared output of predosing in the previous $\sim$1/2 min interval. The improvement in

resolution to < 1 km spatial and ~2 sec temporal is achieved principally by cooling the body of the radiometer (rather than only its chopper), which has the effect of decreasing by three orders of magnitude the product of etendue and sampling time required to produce a given ratio of signal to detector noise.

4. Aircraft Instrumentation

Properties of the 2.832 - 3.125μm and hydroxyl airglow monitoring radiometers, coaligned (and multi-wavelength) photometers, interferometric spectrometer, and video and photographic cameras that make up the measurement system are summarized in Table 2. The prime instruments for determining SWIR structure are a radiometer with three narrow fields (Item 1), the center one of which has coaligned an air fluorescence-measuring photometer (Item 3), and a low-light-level video camera along whose image axis the three radiometer fields are aligned (Item 5).

Figure 1 shows the fields of view of these instruments and of the interferometer (which is manually trainable), along with some intercept dimensions and transit times of fields at altitudes where incoming particle energy is deposited. The optic axes of the radiometers and photometers are tilted 13° forward to point up the earth's magnetic field lines when the aircraft's fuselage is aligned southward along a geomagnetic meridian within a few hundred km of its operating base at Fairbanks, AK. In this orientation the instruments view a volume irradiated by incoming charged particles having a unique energy spectrum, which results in an altitude distribution of excitation that can be calculated from ratios of column intensity of emission features (as referenced in Table 1). Functions and further properties of the aircraft instruments are as follows.

a) Item I, SWIR radiometer, measures the particle energy deposition-associated and other atmospheric radiations listed below, in a band extending ~100 cm^{-1} below that isolated in previous missions. In the focal plane are three 0.3 mm-square InSb detector elements with

Table 2. Instrument Characteristics for 2.8μm-Region Spatial-Temporal-Sources Measurements from Aircraft

ITEM	INSTRUMENT, A/C STATION	MAJOR FUNCTION	SPECTRAL RESPONSE	FULL FIELD OF VIEW	APERTURE	DETECTOR SENSITIVITY	FEATURES IN PASSBAND, COMMENTS
1	Radiometer E-40, 510	SWIR (NO)	2.832-3.125 μm FWHM (+3 positions)	3 units 0.36° □, ⦰'s separated 0.82°	2 in diam	InSb, $D^*=1-2\times10^{13}$ cm Hz$^{\frac{1}{2}}$/w	48% of NO overtone sequence, plus OH & thermal (calculated), plus 1R/7R 3914Å fluorescence
2	Radiometer E-15, 550	OH Monitor	1.7003 ± ½ 0.0773μm	10° circular	2 in diam	PbS, NER 8 kR in 3 sec	P&Q of OH (5,3) & R of (6,4), plus 1R/5R 3914Å fluorescence
3	Photometer E-41, 510	Prompt Excitation	3914Å N_2^+ & 5577Å O_2^1	0.36° □, ⦰ aligned to center FOV of Item 1	3 in diam	PMT	Adaptation of interference filter photometers used on HAES rockets
4	Cryogenic Interferometer E-42, 580	Spectrum, Sources	2-5½ μm (+ Filter)	1.15° (Trainable)	2 in diam	InSb, LN$_2$; 1 sec scan	NESR 2 $\times 10^{-12}$ w/(cm^2 ster cm^{-1}) in 1-sec integration, resolution 10 cm with apodization
5	LLL TV E-209, 470	Predosing & Prompt	S-20 (+ Filter)	17½ x 23° or 165°	f/1.5 or f/1.4	ISIT Vidicon	4-position filter wheel, 1 kR in 1-sec integration
6	Photometer E-05, 1030	Deposition Altitude	S-20, Filters	0.5° circular	2 in diam	PMT, cooled	12-position cycling filter wheel, 24 sec; also 5199Å monitor
7	Camera E-13, 990	Morphology	0.38 - 0.68 μm FWHM	165° (all-sky)	f/1.5	EK 2475 photographic	Optical aurora, backup to video. 4.3 or 11.4 sec exposures

Figure 1. Pointing of three-channel 2.8μm radiometer, photometer, interferometer, and low light level video camera from the NKC-135 aircraft. Performance characteristics of these and the other instruments are in Table 2.

EDGE OF LLLTV FRAME
23.3° x 17.5°
(or 160° all – sky)

13° forward of zenith   18°

A/C Motion
(to South)

20 x 20
TV Lines

1.0°

8 sec†

1.75 km

TV Frame Center

0.46° edge separation

12.7 sec†

0.36° square fields*

COALIGNED RADIOMETERS & PHOTOMETERS

1.15°

INTERFEROMETER
Trainable within 20° of zenith‡

* 0.63 km projected 100 km above aircraft, ~ 7 x 7 TV Lines

† at 0.22 km/sec airspeed

‡ can overlie radiometer field

113

centers on a line parallel to the aircraft body's long axis. Projected
back through the radiometer's objective lens, the individual fields are
0.36° square separated by 0.46° (see Fig 1). Edge to edge the array
covers 2.0° of sky, and center to center of the outside detectors (1.64°)
sweeps across the 105-km altitude level in $12\frac{1}{2}$ sec. In addition by
means of a continuously driven internal mirror the three fields can be
swept a maximum of $\pm 1.0^{\circ}$ along the long axis of the array in 1/2 sec,
so that an individual detector can "follow" a region for ~15 sec.

The radiometer is cooled to liquid-nitrogen temperature (77 K), has
an internal 150 Hz chopper, and views through an LN_2-cooled aircraft window.
The system detectivity converts to ~4 kR noise equivalent radiance in 1 Hz band-
width. The background noise may thus be dominated by natural
variations in column intensity of the hydroxyl airglow, whose mean
value in the radiometer's passband is ~190 kR.

This zenith sky background is calculated from the nighttime
hydroxyl fundamental vibrational band and rotational line intensities
stated in Section I of Ref 1, with the further assumption that the
energy sensitivity of the SWIR radiometer is uniform between its half-
response wavenumbers 3200 and 3531 cm^{-1} (only). Essentially all
of the P branch of the OH $(1,0)$ transition, 92% of the P and all of the
Q and R branches of $(2,1)$, and all of the R and Q branches of $(3,2)$
lie in this passband, assuming a winter mesosphere temperature of
213 K. (The transmission of the atmosphere above the aircraft, which
is of the order of 0.97 and which has very little variation over the
passband, is not included in the derivation of these figures.) The
absolute hydroxyl radiance is subject to long-(days) and short-(minutes)
period variations caused by various geophysical perturbations, as
described in Appendix III of Ref 2.

Thermal radiation from the water vapor and CO_2 molecules
above the aircraft contributes of the order of 4 kR to the near-zenith
signal, assuming the model Arctic atmosphere in Section I of Ref 1
(see in particular Fig 7). The actual intensity of this smaller sky

114

background on any given night depends on meteorological conditions near the tropopause. Intensities of both the airglow and thermal radiations vary slowly compared with that of the chemiluminescence induced by precipitating energetic particles.

These particles also excite by direct impact some air fluorescence at wavelengths within the radiometer's passband, in N_2 $B \to W$ and some $A \to B$ and $W \to B$ transitions (Ref 8). The relative intensity of this "prompt" radiation is less than 1 Rayleigh per 7 Rayleighs of N_2^+ First Negative (0,0) 3914 Å band emission. This effective conversion efficiency is an upper limit because the $A\ ^3\Sigma_u^+$ and $W\ ^3\Delta_u$ upper states are to some extent collisionally quenched at the lower energy-deposition altitudes. As this fluorescence component is very small compared to the ~5 SWIR photons per 3914 Å-band photon previously measured (Sections II and IV or Ref 2), the inaccuracy in its absolute value introduces little error when it is subtracted from the total signal.

As previously noted, most of the SWIR emission is currently believed to result from chemiluminescence in the vibrational overtone of nitric oxide. The radiometer is sensitive within its FWHM to 0.48 of this system's intensity when $NO^{\ddagger}$ is produced by the reaction of N^2D with O_2, assuming the AFGL/OPR model of initial distribution of upper states and Einstein coefficients for the radiational cascade. Transmission of the Arctic winter atmosphere above the aircraft to the rotational lines in this fraction of the NO $\Delta v = 2$ sequence is $93 \pm 4\%$.

The uncertainty in atmospheric transmission is expected to be less than that due to other errors from the measurement system and in the theoretical support. These include errors caused by inaccurate modeling of the concentration profile of absorbing H_2O (which can vary during flight), in absolute calibration of the SWIR and OH monitor radiometers, in calculation of the ratio of intensities of OH fundamental to overtone sequence radiation in the nightglow, and in the calculation of the fraction of the NO overtone system that lies within the radio-

meter's passband. (The atmosphere's transmission to the NO over-
tone sequence is now being recalculated using newly-derived positions
of rotational lines. Some systematic offsets, amounting to as much
as 0.3 cm^{-1}, are now thought to be present in the input data adopted
for the earlier calculation (Section I of Ref 1).

If $NO^{\dagger}$ is produced in reactions that result in spectral distri-
butions different from that excited by $N^2D + O_2$ (such as $N_2(A)$ with O)
or if other species' emissions are contributing to the signal in the
SWIR passband, this 0.48 overlap-response figure of course does not
apply. The radiometer has very little sensitivity to the $021 \rightarrow 000$
and $101 \rightarrow 000$ transitions of CO_2 that lie below $\sim 2.8 \mu m$, which as
previously noted may be excited as a result of particle energy
deposition; this is because the instrument's high-wavenumber cutoff
is selected to reduce attenuation by the atmosphere in these bands.
The interferometer (Item 4) is intended (also as noted) to determine
the actual spectrum of the emissions in the SWIR radiometer's passband.

b) Item 2, hydroxyl radiometer, measures the intensity of air-
glow in a segment of the hydroxyl overtone sequence to monitor the com-
ponent of the SWIR radiometer's signal that comes from fundamental-sequence
emission. The OH Meinel-band and air-fluorescence features to
which this auxiliary filter radiometer is sensitive are listed in the last
column of Table 2.

To produce acceptably high signal/noise ratios without cooling,
the narrow wavelength-band instrument's angular field is opened to
10°. As the spatial (and temporal) scale of the natural fluctuations in
hydroxyl airglow intensity is generally larger than the projection (and
transit time) of this field of view, the error in applying the "background"
data to the narrow-field radiometers is small. Extrapolation of the
measured overtone radiances to determine the OH fundamental's
contribution within the SWIR radiometer's $2.832 - 3.125 \mu m$ sensitivity
band requires that the relative intensity distribution within the radiational
cascade remains constant. With the assumptions of the usual excita-

tation-population reaction $H + O_3 \rightarrow OH^\ddagger + O_2$, negligible collisional deactivation of $OH^\ddagger$, and 213 K winter mesosphere rotational temperature (this has only second-order effect on the result), the ratio of column intensity in the SWIR radiometer's passband to that in the monitor radiometer's passband is calculated to be 2.57 photons/photon (at the aircraft, model atmospheric transmissions included). This theoretically-derived ratio can be validated against the ratio measured in the absence of particle bombardment (as is done in the data reductions in Ref 4).

The OH radiometer's wavelengths are selected for minimum sensitivity to air fluorescence. It detects principally only the (2, 5) band of the N_2 First Positive (B $\rightarrow$ A) system. Some N_2 W $\rightarrow$ B bands (Ref 8), and the N_2^+ Meinel (3, 4) band at 1.656μm. A ratio of 1 R signal/5R 3914 Å is calculated from a model auroral spectrum (mainly from Ref 9). This figure agrees with the small (and apparently some-what variable) increases associated with optical aurora that show in the hydroxyl radiometer traces in Ref's 3 and 4, and also when the instrument is used at ground stations (Ref 10). This small air fluorescence component (which is typically a few percent of the intensity of the OH overtone) is subtracted before applying the aforementioned photon ratio to find the OH fundamental-transition radiances.

c) Item 3, photometer, determines energy input into the radia-ting volume by measuring the column intensity of N_2^+ First Negative band fluorescence and OI green line fluorescence-chemiluminescence (as described for example, in Section V of Ref 2). The dual-wavelength photometer is coaligned with the middle field of the SWIR radiometer, with the aid of a specially-designed collimator-optical bench. This auxiliary system (described elsewhere) aligns the radiometer-photo-meter telescopes and the video camera's (Item 5) optic axis by means of a laser-autocollimator and retroreflectors fastened to the topside of the aircraft. These instruments are located within 40 inches of one another to minimize field offsets that might be caused by the airframe's flex in flight. The collimator system is designed to achieve coalign-ment within 1/10 radiometer field, or about 0.6 milliradians.

The two strong emission features at 3914 Å and 5577 Å, which carry about 3/4 of the energy emitted from particle-excited air at photographic-visible wavelengths, are separated by a dichroic mirror after first passing through a common objective lens and field stop. Each is then isolated by an interference filter from other air fluorescence bands in the photocathode's sensitivity range. The principal application of the photometer data is measurement of the prompt energy input to the column, from the 3914 Å -band radiance. Additionally the ratio of column intensities after the OI chemi - luminescence component builds up to equilibrium is a measure of the spectral index of the precipitating electrons, and therefore of the altitudes at which they deposit energy (Appendix II of Ref 2 and references therein).

d) Item 4, interferometric spectrometer, is designed to measure the spectral intensity of chemiluminescence in the SWIR region with sufficient wavelength and intensity resolution to identify emitting species and determine (when Einstein coefficients are known) upper-state populations. In particular, as noted above, the spectro- meter resolves the vibrational bands of NO's overtone sequence. (Thermal radiation by the atmosphere is expected to preclude measure- ment of the fundamental sequence lying above $5.3\mu m$.) To reduce noise due to high background at the longer wavelengths the instrument's spectral range can be limited by the usual internal optical filters. The interferometer's interior is cooled to LN_2 temperature (as is the SWIR radiometer, Item 1) to reduce internally-generated noise.

Spectral intensity in the NO overtone in IBC III auroral- particle bombardment of $> \frac{1}{2}$ min duration is expected to be of the order of 5×10^{-12} w/(cm^2 ster cm^{-1}) refer to Fig 13 of Ref 1, computed for IBC II, which is 5 kR 3914 Å ; and to Fig 60 of Ref 2 . Since the interferometer's noise equivalent spectral radiance is 2×10^{-12} w/(cm^2 ster cm^{-1}) for a single (unfiltered) one-sec scan, useful signal/noise is achieved by coadding a few sec of data. For the more common (and persisting) case of IBC II precipitation

118

~1 - 2 min of coadded interferometer scans produce useful spectra. Computerized synthetic-spectrum and correlation-spectroscopy procedures are now being developed (by AFGL) to correct for hydroxyl, fluorescent, and thermal emission backgrounds, and best-fit the data to model distributions of chemiluminous emission.

The interferometer is mounted in an AFGL/OPR cold "eyeball" window that permits it to be trained to any position within 20° of the zenith. With the aid of the video system, an operator can hold its field on a strongly-emitting region to build up signal.

e) Item 5, low-light-level video camera, measures the predosing of the upper atmosphere as well as the "prompt" energy input in the two outer radiometer fields. In addition in its wide-field (all-sky) mode it displays to the flight crew the morphology and movement of the optical-auroral forms that show where particle energy is being deposited. By measuring the sky's fluorescent-radiance distribution each 1/30 sec, the camera determines both spatial and temporal changes in the energy input. A detailed description of this instrument and its magnetic tape recording and playback system, its intensity-spatial resolution calibration, and its performance in the Sept 1977 aircraft flight series is in Ref 11.

The axis of the narrower $(17\frac{1}{2}^\circ \times 23^\circ)$ camera field points 18° forward of the zenith (refer to Fig 1, which also shows the number of TV lines per unit angle and the pointing of the SWIR radiometer). Thus the particle energy input is measured ~ 29 km or (at the aircraft's normal forward speed of 0.22 km/sec) 2 min before arrival of the radiometer's fields of view. Particle precipitation at substantially greater distances can be observed,at the penalty of decreased spatial resolution,with the all-sky lens in place. Lenses can be switched in 2-3 sec from a control station located at the video monitor. The axis of the all-sky lens points to the zenith to provide the conventional view of auroral-bombardment morphology.

Point intercalibrations against the coaligned and multi-wavelength (Item 6) photometers can be used to ensure photometric accuracy of the video signals. Accuracy is otherwise limited by "shading" nonuniformity and other imperfections of the ISIT vidicon's cathode, and by errors in converting videotape voltage outputs to scene radiance (which requires a correction for the system's automatic gain control). A four-position filter is located at the telecentric stop of the optical system, where the angular divergence of the image beam is a minimum. This arrangement allows the N_2^+ 3914 $\overset{o}{A}$ band or the OI 5577 $\overset{o}{A}$ line (or other emission features) to be isolated by interference filters with passbands as small as 100 $\overset{o}{A}$ when the all-sky lens is used, and 10 $\overset{o}{A}$ with the narrow-field lens.

f) Item 6, multi-channel photometer, has as its major function determination of particle energy deposition altitudes from ratios of intensity of emission features (as described in Appendix II of Ref 2, and in Ref 6). Secondary functions of this instrument, whose optic axis is also coaligned with the radiometer, are measurement of N^2D-^4S ($NO^{\pm}$ precursor) radiation and backup for the Item 3 photometer. The instrument and its calibration are described in the planning document for the 1976 flight series, Appendix I of Ref 2, which also contains reference to its previous applications in measuring visible emissions from the upper atmosphere.

g) Item 7, all-sky camera (also described in Ref 2), serves principally as backup to the video camera. It provides a readily-accessible and -reproducible record of the spatial distribution of energy input, albeit with poorer time resolution ($\sim$ seconds). With fast monochrome film this conventional camera's contrast detectivity, or ability to detect brightness differences, is 40 times worse than that of the aircraft's video system at low levels of average scene radiance.

5. Flight Plans

The procedures that have been used control the aircraft in previous flight series from Eielson AFB (Fairbanks, AK) are outlined

in Section C, Appendix I and Section VI of Ref 2, and in Section IV of Ref 1. As these crew management, launch decision, and inflight procedures have proven effective in the past aircraft SWIR radiometry missions referenced in Table 1, with the exceptions listed below they will be adopted for the present flights. (An operating plan with a schedule of mission dates will be issued by AFGL/OPR approximately one month prior to each field program.)

The nights on which the aircraft is launched will be selected on the basis of instrument/aircraft/crew availability, weather conditions, and lunar cycle (< 1/2 moon or age 21 to 7 days preferred), without consideration of local magnetic activity or other indications of later particle precipitation. This "randomized" mode of operation is chosen because experience from previous flight series indicated no clear correlation between magnetometer deflections at Fairbanks or Fort Yukon in the evening sector, and useful auroral particle-energy input in the local midnight sector at latitudes within flight range. Takeoff will be at approximately 0600 UT (2000 local), with mission durations up to about 5-6 hr, after which time energetic particle precipitation in this region usually falls below useful levels.

The flight trajectory will be north and south along a geomagnetic meridian, preferably near $257^{\circ}E$ geomagnetic latitude to overfly groundbased sensors at Poker Flat Research Range ($\sim 65^{\circ}$-$66^{\circ}N$). Fig 2, adapted from Fig 21 of Ref 1, shows the aircraft's positions in the Q = 3 ("mean") auroral oval at local magnetic midnight. Plots of similar previous flight paths, whose latitude limits were selected to maximize the energy input in the aircraft's zenith (with some longitude constraints to avoid interference with launches of sounding rockets from Poker Flat), are in Appendix D of Ref 4. Projections of this geomagnetic N → S → N track in the coordinates of the rotating auroral oval — that is, location of the aircraft with respect to the oval — are shown in Appendix II of Ref 1 (p II-7). The instruments will take data on the northbound as well as southbound segments of the flights, to provide a cross-field projection of the volume emission rates at infrared and visible wavelengths.

121
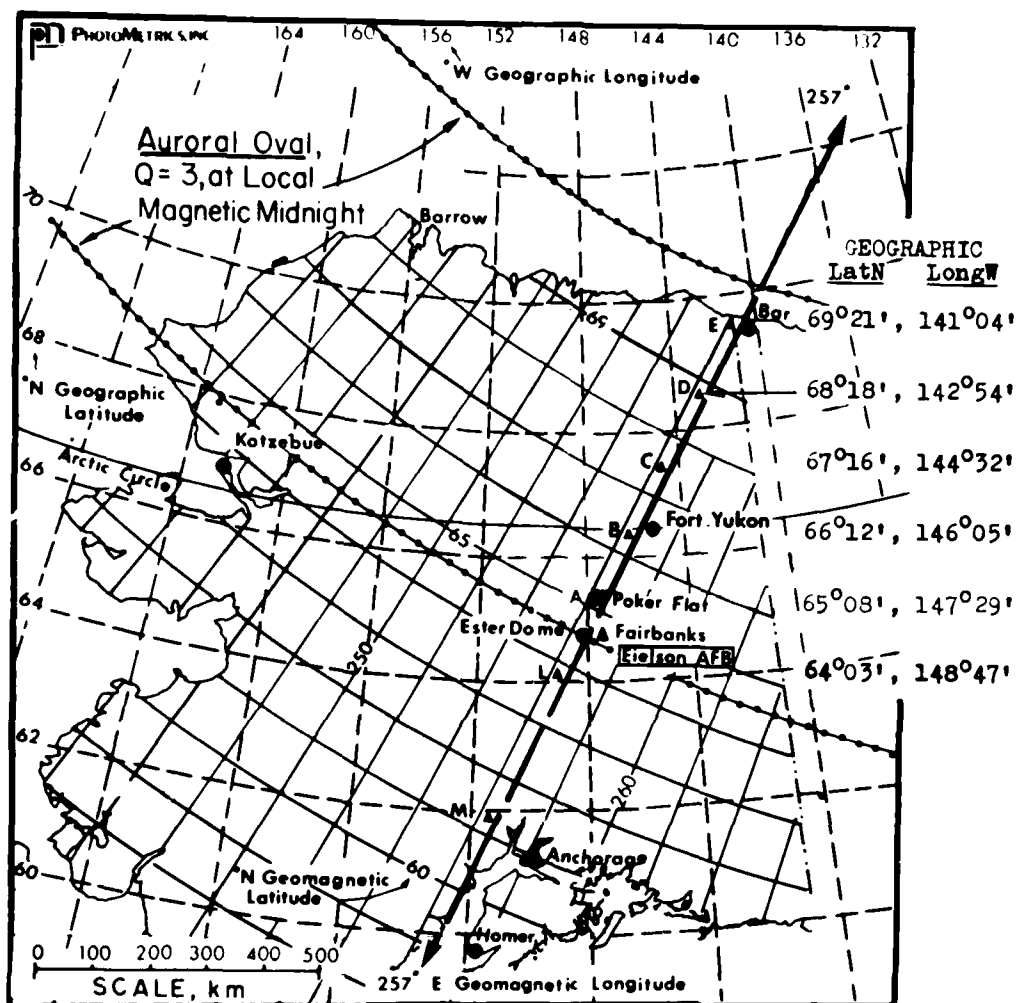
Figure 2. Measurement trajectory, along the geomagnetic
meridian through Poker Flat Research Range, of
the aircraft instrument system (heavy line). The
latitude-longitude points L-E are separated by 10.0
min flight time in the absence of headwind or tail-
wind. Also shown is the "mean" midnight auroral
oval.

Latitude limits on this flight path are selected by the mission controller on the basis of (1) latitudes at which optical aurora is present, as shown on the all-sky video monitor; (2) magnetic activity, as reported from Poker Range, and (3) further information about development of magnetospheric substorms, as furnished by the University of Alaska Geophysical Institute's observers. (N-S-N movement of auroral forms and the eventual "breakup" are associated with the substorm.) On the basis of this information the controller also decides when the night's data mission is to be terminated. Radio communication is maintained through the Institute's Telecommunications Center (in the C. T. Elvey building), at which chart recorders display the College and Fort Yukon 3-axis magnetometer readings. The cost of maintaining this radio link is justified by the potential saving in aircraft operation costs.

Successful performance of the aircraft-based SWIR structure-sources program does not require data from the other instrumentation at Poker Range. Those ground instruments in operation can provide the following backup-support information. (Items are listed in the order of Table I. 3 of Ref 2; refer to Appendix II of Ref 1 for further identification of the sensors.)

— DNA 617 (Chatanika) Incoherent-Scatter Radar	Altitude profiles of ionospheric electron density, irregularity structure
— SWIR Radiometers	OH background variations, (inter-calibration with A/C radiometer)
— 3 Color Photometers	Altitude profile of energy deposition, long-period predosing
— 3 Beam Photometers	Mean phase velocity of region of energy input
— Fixed Photometers, Spectrometers	N^2D and N^2P (NO^+ precursor) concentrations
— (RAOB's: the lower-atmosphere temperature and H_2O profiles are less important since the radiometer's sensitivity band has been shifted to a region of substantially lower thermal emission)	

Symbol	Meaning
$I(x', t)$	Input particle-energy deposition rate, as measured by the column intensity of fluorescent emission (i.e., visible radiance)
$J(x, t)$	SWIR column emission rate (infrared radiance)
$F(x')$	Spatial distribution of energy input, as measured by the low light level video camera
$C(T)$	Cross-correlation function of lag T
$A(T)$	Autocorrelation function of lag T
$R(t - t')$ or $R(s)$	Test function describing the rate at which previous excitation leads to production of $NO^\ddagger$
N	Normalizing factor for R: $N = \left[\Gamma(n+1) \tau^{n+1} \right]^{-1}$
K	Total number of SWIR photons emitted per unit particle energy deposited (altitude-dependent, perhaps dose rate-dependent)
$R_p(s)$	Parameterized form of the test function $R_p = \left[\Gamma(n+1) \tau^{n+1} \right]^{-1} s^n e^{-s/\tau} \, (= N s^n e^{-s/\tau})$
n, τ	Adjustable parameters in R_p; R_p has its maximum at time $n\tau$
$J_p(t)$	Estimate of J found by substituting R_p into the model equation $$J_p(t) = K \int_{-\infty}^{\infty} I(t') R_p(t - t') dt'$$
x^2	Sum of squares of residuals, used in "best-fitting" to determine n and τ $$x^2 = \Sigma \left[J(t_i) - J_p(t_i) \right]^2 / \sigma_i^2$$
σ_i	Experimental uncertainty in measurement of $J(t_i)$
$q(\omega), j(\omega), r(\omega)$	Fourier amplitudes of $I(t'), J(t), R(t - t')$ respectively
$G(x - x', t - t')$	Spread function of SWIR output (see text)
ϕ	Phase shift between energy input and SWIR output
k	Propagation vector $2\pi/\lambda$
λ	Wavelength
D, l	Diffusion coefficient, diffusion length
d	Separation between successive radiometer fields at typical energy-deposition altitude, 100 km above aircraft
V	Drift velocity of emitting species and/or its precursors
V_A	Aircraft velocity

On the left side, spanning the first three rows:
Primary Measured Quantities

124

— Meridian Photometers, All-Sky Cameras

— DMSP Satellite Photometer (visible-sensitivity channel)

Post-characterization of distributions of particle precipitation over the region in which the aircraft measures infrared-visible correlations and SWIR spectral distributions.

6. Interpretation of the Radiometry Data

a) Qualitative Considerations, Correlation Functions

The major goal of analysis of the temporal and spatial relationships /correlations between the SWIR and air-fluorescent radiance distributions measured from the moving aircraft, is to determine the aeronomic processes relating SWIR emission output to particle energy input. The function of the program is to validate and provide input parameters for the currently-accepted predictive model of $2.8\mu m$-band emission (Ref's 3, 7, 12), which considers the principal radiation to be chemiluminescence of $NO^{\ddagger}$. Altitude dependence of these parameters is determined from measurements on excitation by precipitating-particle beams with a range of characteristic energies.

Radiance data from previous flights with wider-angle radiometers and photometers (~15 km fields of view, traversed in ~1 min) have so far been analyzed by means of simple cross-plots of simultaneously-measured intensities (as in Ref 2). The slope of the regression line on these plots measures the SWIR yield provided that the particle energy inputs, averaged over the instrument field, are not varying substantially in the "characteristic" predosing time. The aircraft instrument system described in subsection 4 is designed to be able to detect spatial-temporal decorrelation to ~0.6 km - 1 sec, a scale small compared to that expected for the aerochemical processes leading to SWIR emission. Thus these higher-resolution data should allow determination of this predosing time, and more generally speaking, of dependence of SWIR output on energy input.

The standard techniques of cross-correlation and Fourier analysis permit the relationships between two data streams to be inferred when one depends on previous as well as instantaneous values of the other, as is expected in this case. The cross-correlation function is defined by the expression (neglecting for clarity questions of normalization)

$$C(T) = \int_{-\infty}^{\infty} I(t) \, J(t + T) \, dt,$$

where $I(t)$ is the time-dependent photometer signal and $J(t + T)$ the
SWIR signal from its coaligned radiometer shifted by a time T (refer
to Table 3 for definition of symbols used with this derivation). If
$J(t)$ were to remain proportional to the instantaneous energy input
$I(t)$, as assumed in the scatter plot analysis, $C(T)$ would be proportional
to the input's autocorrelation function

$$A(T) = \int_{-\infty}^{\infty} I(t) \, I(t + T) \, dt.$$

$A(T)$ of course has a maximum at zero lag, $T = 0$. The
"width" of this peak is a measure of the time span over which the
particle precipitation rate remains self-correlated, or alternatively,
of the amplitudes of the low-frequency components of the data stream.
(Some Fourier transforms of $A(T)$ — power spectra — for real particle
precipitation are shown in Ref's 13 and 14.) $C(T)$ is also expected to
have a maximum at $T = 0$, because the low temporal frequency com-
ponents present in the energy input contribute to an apparently-
"instantaneous" infrared output. A width of $C(T)$ greater than that of
$A(T)$ is a quantitative indication of the effect of predosing. In the
special case that the correlation peaks have approximately Gaussian
shapes, the range of times over which predosing contributes to SWIR
emission can be found by subtracting, in quadrature, the widths-to-
half-maximum. (An important assumption for this illustrative example
is that the region viewed in the time period remains spatially near-
uniform; the argument will shortly be generalized to "moving" auroral
forms.)

Most of the information about aeronomic processes is
contained in the depature of $C(T)$ from simple proportionality to $A(T)$.
The distribution of energy input in time (and/or space, as is described
in subsection 6e) conditions the accuracy with which this difference

126

between the two functions can be measured. Specifically a broad, relatively structureless A(T), which results from slowly changing energy input, would be expected to produce a similarly-broad C(T) whose difference from A(T) cannot be measured accurately. Sharp spatio-temporal variations in I(t), on the other hand, narrow A(T) (and broaden the Fourier spectrum), so that differences of C(T) at time lags comparable to the "characteristic" predosing time can be more accurately determined.

A more quantitative and detailed discussion of this correlation function-Fourier transform approach to extracting information from data from a single coaligned radiometer-photometer pair is presented in subsection 6e. It should be stressed that this method is frequently applied when no a priori information is available about the relationship of two time-varying functions, with the expectation that its numerical results will provide insight into the underlying physical dependence.

b) Model Input-Output Relationship

There exists of course a potentially testable physical model relating J to I, as embodied in the OPTIR chemical-reaction code now being integrated into the ROSCOE systems code. This aerochemical model, major elements of which are shown schematically in Fig 3, predicts an altitude-dependent grow-in time for vibrational excitation of NO molecules, of the order of a few sec for step-function energy input (see, for example, the sample calculations in Ref 15). The model does not include other sources of $2.8\mu m$-emission, for example the CO_2 intercombination-band vibraluminescence suggested as contributing to the field simulation results (p 327 of Ref 3; see also Ref 7); this process has characteristic time ~ 1 min.

Although the notation adopted for this data analysis refers to the nitric oxide aeronomy model, the mathematical procedure also applies to other emitting species (more on this point shortly). The predosing concept can be expressed by the relationship

Fast Electrons

N_2

O_2

O

$N_2(A)$

N^*

N_2^+

N^+*

N_2

O_2^+*

O^+*

NO'

e

N_2D

O_2

NO^+

$NO+$

~2.8μm & ~5.4μm photons

Primary Ionization, Dissociation, & Excitation of Air by Electron Impact

Reactions that Result in Vibrationally-Excited NO^+

IR Emission

Figure 3. Schematic diagram of currently-applied DNA/DoD model of excitation of radiation near 2.8μm from air bombarded by energetic charged particles. Competing reactions that lead to de-excitation without SWIR radiation (for example $N^* + O \rightarrow N + O^*$) are not shown. The model does not consider energy input-associated radiation by other species.

$$q_{NO}(t) = f \int_{-\infty}^{t} q_o(t')R(t-t')dt' ,$$

in which q_{NO} and q_o are rates of production per unit volume of NO and initial ionizations respectively, f is the fraction of these ionizations that ultimately lead to production of an NO molecule, and R is a test function expressing the rate at which power input leads to NO production. (Since the lifetime of $NO^{\ddagger}$ against radiation is short compared to the time for the reactions in Fig 3 to proceed, the production rate of NO molecules is taken as proportional to the production rate of NO vibrational photons.) R in effect "fits" the more complex input-output relationship derived by the computer model, at some mean dose-rate level.

Ionization by incoming energetic electrons of the atmosphere's nitrogen molecules, which leads to the major fraction of the NO production (and whose rate is reasonably closely proportional to the ionization-excitation rates of O_2 and O, which as Fig 3 shows are also contributing) is measured by the N_2^+ 3914 $\overset{o}{A}$ (and 4278 $\overset{o}{A}$) First Negative band emission. Assuming as usual (Section V of Ref 2) that the intensity of this prompt fluorescence is proportional to the column rate of energy input, and that R does not change substantively over the range of altitudes in which energy is deposited (recall that the instruments, pointing up the field lines, view an essentially-unique primary energy spectrum with a relatively narrow range of deposition altitudes) leads to the expression

$$q_o(t') = K' I(t') .$$

Here $I(t')$ is the First Negative-band radiance and K' a constant that takes into account the effective height of the column. Similiarly

$$q_{NO(t)} = K'' J(t) .$$

The 2.8μm column emission rate then becomes

$$J(t) = K \int_{-\infty}^{t} I(t') R(t - t') dt,$$

where K is another proportionality factor encompassing K', K'', and f, whose meaning will be discussed momentarily. This expression will be referred to as the model equation that relates the two measured quantities J and I.

When R is normalized to time-integrated value unity (between limits $-\infty$ and t), K infrared photons are eventually emitted per N_2^+ fluorescence photon. The factor K can be determined directly from data during a period when the particle precipitation changes little over the expected predosing time, since constant $I(t')$ implies

$$J = KI \int_{-\infty}^{t} R(t - t') dt' = KI.$$

This factor would appear to be the same as the lumped-parameter, long-duration-dosing SWIR yield derived from the wide-angle aircraft instruments, described above. More generally, K can be determined from the ratio of long time-averaged visible and infrared radiances.[*]

---

[*] The average SWIR emission in time Δt is

$$\overline{J} = \frac{1}{\Delta t} \int_{t - \Delta t}^{t} J(t) dt$$

$$= \frac{K}{\Delta T} \int_{t - \Delta t}^{t} \int_{-\infty}^{t} I(t') R(t - t') dt.$$

An exchange of the order of integration and substitution of $s = t - t'$ gives the result

130

The model equation which relates the data from a single
coaligned radiometer-photometer pair, applies when the particle
energy input has little spatial variation over the region swept by the
fields during the characteristic predosing time. As noted in sub-
section 4 the time of "effective" uniformity can be extended by moving
the radiometer's field (a maximum of 2° in zenith angle) to compen-
sate for the aircraft's forward motion. The integral in practice
extends back for times of the order of $\frac{1}{2}$ min if $NO^{\ddagger}$ (excited in $N^2D + O_2$
reactions) is the dominant emitting species, and longer if $CO_2^{\ddagger}$ is
contributing substantially to the SWIR radiances. Generalization of
the model equation to spatially-varying and moving energy input
distributions can be straightforwardly done using data from the video
camera, as described below in Section 6d.

c) Evaluation of the Test Function

R can be determined directly from the Fourier transforms

(Footnote cont'd)

$$\overline{J} = \frac{K}{\Delta t} \int_0^\infty R(s) \int_{t - \Delta t}^t I(t - s)\, dt\, ds$$

This average can also be written as

$$\overline{J} = \frac{K}{\Delta T} \int_0^\infty R(s)\, ds \int_{t - \Delta t}^t I(t)\, dt$$

$$+ \frac{K}{\Delta T} \int_0^\infty R(s) \left[\int_{t - \Delta t - s}^{t - \Delta t} I(t)\, dt - \int_{t - s}^t I(t)\, dt \right] ds.$$

Since the second term approaches zero as Δt becomes large,

$$J \approx \frac{K}{\Delta t} \int_{t - \Delta t}^t I(t)\, dt = K\overline{I} \; .$$

131

of the data streams, and indirectly by assuming a physically-reasonable analytical form with free parameters that are fit to the data. To provide insight into how the relationship of output J to input I tests the SWIR emission model, the second approach will be treated first.

The aerochemistry models (Ref 15 for example) indicate that following impulsive energy input R increases as the concentrations of N^2D and other reactive $NO^\ddagger$ precursor species build up (refer to Fig 3) and then decays as these species become depleted. This behavior can be approximated by the form (recall that $s = t - t'$)

$$R_p = N \, s^n \, e^{-s/\tau} \, ,$$

where the parameter τ is a time constant that in a rough sense characterizes the decreasing contribution of earlier predosing, and n a factor that measures the rate of grow-in of excitation of $NO^\ddagger$ (or other radiating species whose concentration first increases and then decreases) after energy is deposited in the atmosphere. The exponent n is of order unity and s and τ are expressed in seconds. N is the factor that normalizes $\int_0^\infty R \, ds$ to 1; performing the integration gives the result

$$N = \left[\Gamma \, (n + 1) \, \tau^{n + 1} \right]^{-1} \, ,$$

where Γ is the gamma function (a tabulated definite integral). The maximum in R comes at $s = n\tau$, which may be viewed as a characteristic buildup time. A two-parameter fit is considered necessary to allow independent rates of grow-in and die-out of SWIR emission.

This first procedure, then, determines the parameters n and τ that make $\int_{-\infty}^t I(t') \, R \, (n, \tau) \, dt'$ most closely fit the observed SWIR column-emission rates J(t). A commonly-used approach is to construct with measured I(t') data $J_p(t)$'s for sets of assumed n's and τ's:

132

$$J_p(t) = KN \int_{-\infty}^{t} J(t')\,(t - t')\; e^{-(t - t')/\tau}\, dt.$$

Standard procedure for assessing when best-fit is achieved (see for example, Ref 13 where it is applied to atmospheric-emission data) is to find the minimum of the sum

$$x^2 = \sum_i \left[J(t_i) - J_p(t_i) \right]^2 \bigg/ \sigma_i^2 \,,$$

where σ_i is the uncertainty in the measurement of $J(t_i)$ (that is, to match by least-squares).

x^2 - the chi-squared commonly used in statistical testing — is most sensitive to n and τ when the particle energy input is changing rapidly; at the other extreme constant input, which according to the aerochemical model results in steady-state SWIR emission, yields (as previously noted) no information about predosing. Noise and the finite intensity resolution of the data of course set limits to the accuracy with which the parameters of R can be determined. If the test function selected refuses to fit the radiance data — as manifested by large values of x^2 for all n, τ — another model is adopted and the calculation repeated. The confidence limits of the fit and estimates of the accuracy of the "best" n and τ, can be determined by applying the standard statistical measures from texts such as Ref 16.

The transform of the test function R can be determined directly by analyzing the radiance data in terms of their Fourier components. Alternatively the accuracy with which n and τ are determined can be improved by making use of temporal frequencies at which the signal-to-noise ratios are high (as discussed in the next paragraph). Let $q(\omega)$, $j(\omega)$, and $r(\omega)$ be the Fourier amplitudes of $J(t')$, $J(t)$ and $R(t - t')$ respectively. Since $R(t - t') = $ zero when $t < t'$, the limits of integration on the model equation can be extended from $-\infty$ to $+\infty$; by the convolution theorem the Fourier transform of the model equation then becomes

$$j(\omega) = Kq(\omega) \, r(\omega) \ .$$

Thus the transform of R is simply

$$r(\omega) = j(\omega)/Kq(\omega) \ .$$

This Fourier spectrum gives an immediate indication of the interval over which predosing contributes to output of infrared radiation; as an extreme example, were there no effect of predosing $r(\omega)$ would simply be a δ-function at $\omega = 0$. Calculation of $j(\omega)$ and $q(\omega)$ over the full frequency range in which $J(\omega)$ is non-zero provides, by Fourier inversion, an independent determination of $R(t - t')$ for comparison with the results of DoD aeronomy models.

Extension of the Fourier-transform method to determining the parameters n and τ proceeds as follows (Ref's 13, 16). An auxiliary function R_p' is defined such that

$$R_p' \begin{cases} = R_p, & s > 0 \\ = 0, & s < 0 \ . \end{cases}$$

The Fourier amplitudes of R_p' are then

$$r_p(\omega) = \frac{K}{2\pi} \int_{-\infty}^{\infty} R_p' \ e^{-i\omega s} \ ds = \frac{KN}{2\pi} \int_{0}^{\infty} s^n \ e^{-s/\tau} \ e^{-i\omega s} \ ds$$

$$= \frac{KN}{2\pi} \int_{0}^{\infty} s^n \ e^{-(1 + i\omega \tau)s/\tau} \ ds \ .$$

Integration and insertion of the expression for the normalizing factor N gives

$$(1 + i\omega \tau)^{-(n+1)}/2\pi = j(\omega)/Kq(\omega) \ .$$

134

Equating amplitudes and phases with the phases so defined that j is real gives

$$(\tan^{-1} \omega\tau)^{n+1} = \Phi(\omega),$$

$$\left[\frac{\sqrt{1 + \omega^2 \tau^2}}{1 - \omega^2 \tau^2} \right]^{n+1} = \frac{j(\omega)}{K |q(\omega)|}$$

where Φ is the phase difference between $q(\omega)$ and $j(\omega)$ and $|q(\omega)|$ is the magnitude of $q(\omega)$. The parameters n and τ are obtained by solving these two last simultaneous equations. Statistical methods are available for determining best values of n and τ from the set of j's, q's, and Φ's (an example is given in Ref 13); accuracy can be improved by giving greater statistical weight in the range of temporal frequencies in which the signal to noise ratios of the Fourier amplitudes are highest.

d) Effects of Spatial Inhomogeneity

When the scale of expected mass (or intermediate-radiation) transport in time $n\tau$ or τ is comparable to the scale of spatial structure in the energy input, a generalization of the model equation can be applied. In this case SWIR emission at $\vec{x}$ depends on energy input into the surrounding ionospheric region, which is measured by the video camera.

The generalized output-input relationship can be expressed as

$$J(\vec{x}, t') = K \int_{-\infty}^{t} dt' \int I(\vec{x}, t') G(\vec{x} - \vec{x'}, t - t') R(t - t')d\vec{x'},$$

where G is the probability (after appropriate normalization) that initial ionization at $\vec{x'}$ results in SWIR emission at $\vec{x}$ in time $(t - t')$. This transport may be due to physical movement of the emitting and/or

135

precursor species, and also to diffusion of photons that play a part in the intermediate reactions. No radiation transport figures in the model of excitation of $NO^{\ddagger}$ (except to some very small extent that of UV photons produced as a result of the initial electron impacts); on the other hand transport of $4.3\mu m$ (001 - 000) CO_2 photons would have the effect of "smearing" any emission near $2.7\mu m$ from this molecule (following the model in Ref 7).

Transport results from this diffusion plus wind-driven drift of reacting-emitting species. A wind vector $\vec{V}$ carries the excitation from $\vec{x}'$ to $\vec{x}' \rightarrow \vec{V}$ (t - t'), while the diffusion term accounts for transport from this latter position to $\vec{x}$. The appropriate solution to the diffusion equation is

$$ G = \frac{1}{[(2\pi)\, D(t - t')]^{3/2}} \exp[-\ell^2/4D\,(t - t')] $$

where D is the effective diffusion coefficient and $\ell = \vec{x} - x' - V(t - t')$.

In the current $NO^{\ddagger}$ model the offset due to upper-atmospheric wind (typically 50 m sec^{-1}) is larger than that due to diffusion (the typical coefficient is 10^3 m^2 sec^{-1}), in characteristic times of the order of 15 sec. Since the wind vector is essentially horizontal the altitude of emission is the same as the altitude where primary energy is deposited. In the limit of small D the spread function G is replaced by a delta function

$$ G[\vec{x} - \vec{x}' - \vec{V}(t - t'),\ t - t'] = \delta[\vec{x} - x' - \vec{V}(t - t)]. $$

This simplification eliminates one integral in fitting to the measured J's, leading to

$$ J(\vec{x},\ t) = K \int_{-\infty}^{t} I[\vec{x} - \vec{V}(t - t'),\ t']\ R(t - t')dt'. $$

The same procedures used when transport need not be considered can

be applied to fit the test function F to the radiance data, with the exception that the values of energy input rate I are taken at the spatial points indicated; the offset of these points from $\vec{x}$ is a function of (t - t'). (As noted, I is read from the video images.) In other words, a linear coordinate transformation $\vec{x} \rightarrow \vec{x} - V(t - t')$ reduces the problem to the one previously considered (spatial uniformity, subsection 6c).

The drift speed $\vec{V}$ for this analysis can be found from the infrared radiances sequentially measured in two (or three) of the radiometer's spatially-separated fields. Consider first, to illustrate the approach, a fluorescent radiance distribution F(x) that remains stable over the period of measurement (a stable auroral arc, for example). As the narrow-field radiometers move across this from the (assumed) downwind direction, they measure SWIR radiation from a region that is both broadened and shifted with respect to the input energy deposition; drift carries the emission a distance of the order of $Vn\tau$ (or $V\tau$) after excitation. Some 2.8μm photons, for example, could originate from directions in which F(x) is zero.

Next consider the more general case of particle precipitation varying in time while retaining the spatial "shape" F(x). The resulting SWIR emission can be decomposed into traveling waves of the form

$$J = B \cos (\omega t - 2\pi x/\lambda) = B \cos (\omega t - kx),$$

where the propagation vector $k = 2\pi/\lambda$, λ being the wavelength of the Fourier component (B is a Fourier amplitude). At time t the wave goes into successive radiometer fields at points separated by distance d, the horizontal separation of the projections of the radiometer fields on the emitting volume (whose altitude is determined as described in subsection 4). The phase shift Φ between the ω-th Fourier component at these points (determined by transforming the two J(t)'s) is kd. The velocity V in the direction of the three-channel radiometer's (i.e., aircraft's) motion can be determined from this measured phase shift through the relation

137

$$V = \omega/k = \omega d/\Phi .$$

Another approach to determining the drift velocity makes use of the cross-correlation between SWIR radiances measured in two channels

$$C(T) = \int_{-\infty}^{0} J_1(t) J_2(t + T)dt$$

This function generally has a peak at a non-zero value of T because ionospheric regions pass into each field at separated times. Taking V_A as the aircraft velocity, the delay T′ in overlap fields on a pre-dosed volume is $d/(V + V_A)$, where V is positive and V and V_A anti-parallel. The drift velocity computed for a cross-correlation peak at lag T is then $V = d/T' - V_A$.

In the event that the Fourier- analysis or cross-correlation methods provide too low a resolution in measuring the infrared emitting volume's drift speed, $\vec{V}$ can be estimated by treating it as a third free parameter fitting $J(x,t)$'s to $I(x - x', t - t')$ as measured by video photometry.

e)   Particularly Useful Distributions

No matter what specific procedures may be applied, certain commonly-occurring spatial-temporal distributions of particle energy deposition are the most effective sources of information about SWIR correlations and emission processes. Rapid, large-amplitude varia-tions in I are most useful in unfolding R from the data, as would be intuitively expected. For example the test function R(t - t′) appears in the model equation convolved with input energy I(t′); the integral is expected to include significant contributions to J(t) for $t - t' < \frac{1}{2}$ min. Direct fitting to the model equation as described in subsection 6c would produce more accurate values of R's parameters when the input energy is fluctuating sharply, that is, when it has large Fourier amplitudes at high temporal frequencies. Further accurate and/or less model-

dependent results will be provided by the following favorable excitation distributions.

One case (already discussed briefly in 6a) is near-random rapid input fluctuations, which would result in an autocorrelation of I narrowly peaked at zero lag. Substituting the photometer-radiometer cross correlation function

$$C(T) = \int_{-\infty}^{\infty} I(t) \, J(t + T) dt$$

in the model equation and replacing $t - t'$ by s yields the relation

$$C(T) = K \int_{-\infty}^{\infty} I(t) \int_{-\infty}^{t+T} I(t') \, R(t - t' + T) \, dt' \, dt$$

$$= K \int_{-\infty}^{\infty} I(t) \int_{T}^{\infty} I(t - s) \, R(s + T) \, ds \, dt.$$

After interchange of the order of integration this equation can be written as

$$C(T) = K \int_{-T}^{\infty} R(T + s) \int_{-\infty}^{\infty} I(t) \, I(t - s) \, dt \, ds = K \int_{-T}^{\infty} R(T + s) \, A(s) ds,$$

where the function $A(s) = \int_{-\infty}^{\infty} I(t) \, I(t - s) \, dt$ is the aforementioned autocorrelation function of input energy. When $A(s)$ has a narrow peak at $s = 0$, the $C(T)$ calculated from the two data streams provides a direct and model-independent determination of R. (This is of course a special case of the introductory example given in Section 6a, in which $A(s)$ had finite width.) The integral equation can be solved for broader A by the fitting methods discussed previously.

A single coaligned photometer-radiometer pair plus video also extracts useful data from stable auroral arcs, because sharp-edged spatial structure also produces information about the test function R. Let $F(x')$ again represent the "shape factor" for distribution

139

of energy input, normalized to $I(x, t')$. SWIR emission measured at position x and resulting in part from energy input at x' comes from intermediate-and-emitting species which have drifted a distance $x - x'$ and were therefore dosed at time $(x - x')/V$. The infrared radiance distribution is given by

$$J(x) = KI \int F(x') R[x - x')/V] dx' ,$$

where the integral extends over the arc. This expression is formally identical to the model equation and can be analyzed by the same means. An independent measurement of V can be made by methods described above in subsection 6d).

More generally, data from a single coaligned photometer-radiometer pair plus video are sufficient for analysis when the energy input distribution holds constant in time, or less restrictively, when its average over an interval of the order of τ is constant. If the mean level of input energy distribution rapidly changes, sequential views by successive radiometers become effective. One such case is the spatially-stable auroral arc whose surface radiance increases or decreases. Let t_1 and t_2 be the time coordinates for two radiometers sweeping across the form; then $\Delta t = t_1 - t_2 = d/V_A$. The difference between signals from the "same" volume is

$$J_1(t_1) - J_2(t_2) = K \int_{-\infty}^{t_1} I(t') R(t_1 - t') dt' - K \int_{-\infty}^{t_2} I(t') R(t_2 - t') dt'$$

$$= K \int_{-\infty}^{t_1} I(t') R(t_1 - t') dt' - K \int_{-\infty}^{t_1 + \Delta t} I(t') R(t_1 - t' + \Delta t) dt'$$

$$= K \int_{-\infty}^{t_1} [I(t') - I(t' + \Delta t)] R(t_1 - t') dt'.$$

This difference between SWIR radiances is therefore proportional to the convolution of the difference in energy input with the test function. A useful sub-case is rapid turn-on or -off of the form; very rapid motion of the previously-stable arc out of the fields would be equivalent to rapid

shutoff of local excitation. (Generalization to the case in which transport is important is accomplished through the coordinate transformation discussed previously.)

This last expression narrows the limits of integration in the fitting equation, for cases in which $I(t')$ changes abruptly. In the particularly simple special case of finite energy input I in the first-arriving field followed by a steep falloff (for example, the arc moving rapidly away in the 12 sec before the third field arrives), the result is

$$
J_1(t_1) - J_2(t_2) = KI \int_{-\Delta t}^{0} R(t - t')\, dt' \, .
$$

Previously stable arcs often move distances large compared to the distance $nV\tau$, while maintaining near constant intensity. As mentioned in the last-but-one paragraph, this geophysical situation gives essentially the same result as if the energy input in the region of measurement had been rapidly switched off. If energy input ceases at $t' = 0$,

$$
J_1(x, t) = KI \int_{-\infty}^{0} F\left[(x - V(t - t')\right] R(t - t')\, dt'
$$

$$
= KI \int_{t}^{\infty} F(x - Vs)\, R(s)\, ds \, .
$$

This same emitting volume is viewed by the second radiometer at position $x + VT'$ and time $t + T'$, where $T' = d/(V + V_A)$. The SWIR radiance is then

$$
J_2(x + VT', t + T') = KI \int_{t}^{\infty} F(x - VS)\, R(S + T')\, ds \, .
$$

The difference between the two radiances

141

$$J_1(x, t) - J_2(x + VT', t + T') = KI \int_t^\infty F(x - Vs)\,[R(s) - R(s + T')]\,ds$$

$$= KI \int_{t - T'}^{t} F(x - Vs)\,R(s)\,ds$$

provides another means for determining the parameters of R.

f)   Summary and comments

In this section is developed a framework for analyzing the radiance data from the aircraft instruments to verify and determine parameters for the current model of SWIR background emission.   The procedures described are derived from those conventionally used for finding the functional relationship between two dependent variables. Results are probably less sensitive to the specific mathematical approach than to the signal/noise ratios in the sky-radiance data and the presence of high-frequency components in the input, which in practice provide the most information about infrared-visible correlations and source processes.

The analysis is facilitated by defining a function $R(t - t')$ to describe the (later) rate of production of SWIR-emitting species through chemical reactions initiated by particle-energy deposition.   R makes the connection between the field measurements and the aeronomy codes, and R also expresses quantitatively the temporal correlation of infrared to visible radiance.   The integral equation relating the observed infrared output J(t) to simultaneous and previous energy inputs I(t') cannot be solved in closed form for R — which lies inside the integral sign — in the time domain.   The two approaches to evaluating R are

- solving the model equation numeri-
  cally by inserting a trial function
  with free parameters;   and

- Fourier-transforming the data
  streams I and J to determine the
  Fourier amplitudes of the transform;

142

then
$$R(t - t') = \frac{1}{K} \int \frac{j(\omega)}{q(\omega)} e^{-i\omega(t - t')} d\omega .$$

The first approach is more direct, and does not introduce artifactual results; however the insensitivity of the fit in the model equation may produce large error bars on the parameters. Although the procedure provides no a priori guidance to the test function – which is taken from the aerochemical model– statistical measures of the fit give a posteriori an indication of the effectiveness of the analytical form chosen, and so validate the model.

Since $r(\omega)$ can be expressed in closed form (as $j(\omega)/Kq(\omega)$; actually the result is a graphed rather than an analytical function) the Fourier approach does not require selection of test functions. On the other hand the ratio j/q can be seriously distorted by measurement errors and noise, so that the possibility of artifacts in $R(t - t')$ must be considered. The principal value of the Fourier approach is to provide guidance in selection of the form of the test function.

The method of data analysis places no restriction on the input energy distribution. However the most accurate values of the parameters of R will be obtained from certain special but not uncommon distributions, specifically, those that result in the largest visible-infrared decorrelation. Complete temporal correlation is present if $C(T) = KA(T)$, which results from replacing R by a delta function in the equation on page 139 (which is precisely the assumption made in the previously-used scatter-plot analysis). The effect of predosing is of course to broaden R. Slowly-varying $I(t')$ broadens $A(T)$, reducing the accuracy of measurement of decorrelation. In the opposite case, A narrowly peaked at zero – that is, when $I(t')$ is very rapidly varying (has a broad Fourier spectrum) – $C(T)$ is very sensitive to R and thus the uncertainty in C does not produce a comparably large uncertainty in R (and its parameters). Spatial structure in I similarly results in accurate determination of R, in effect because drift time from the region of predosing to the region of measurement is well defined;(isolated) stable arcs are particularly effective sources of data

143

A rapid increase or decrease in <u>mean</u> dose rate in a region provides additional information about R, through sequential sampling by two or three narrow-field radiometers. The shift in energy deposition level results in a change in SWIR radiance with time constant determined by R, and therefore provides data on its parameters n and τ.

The techniques described are complementary, and more than one may be used in analyzing the same data. Fourier analysis provides a qualitative estimate of R, and fitting to the model equation gives artifact-free values of its parameters. The best information about predosing processes and transport mechanisms results from analysis of input energy distributions having scales of temporal and spatial structure smaller than $n\tau$ and $nV\tau$ respectively.

References

1-6 -- in Table 1, page 109.

7. D. H. Archer, Requirements for Improved Infrared Prediction Capacity, HAES Report No. 78, DNA 4585, 30 Apr 78.

8. D. C. Cartwright et al., The IR Emission Spectrum of N_2 Excited Under Auroral Conditions, Aerospace Corporation Report SPL-2311, Nov 1971.

9. A. Vallance Jones, Space Sci. Rev's <u>11</u>, 826 (1971).

10. Ground Support Data Report in Support of Black Brant 18.219-1 Flight (Utah State University, 02 Sep 74, unnumbered).

11. R. B. Sluder et al., Aircraft Program for Target, Background, and Sky Radiance Measurements, AFGL-TR-78-0123, 18 May 78.

12. A. G. Hurd et al., Comparison of ICECAP and EXCEDE Rocket Measurements with Computer Code Predictions, AFGL-TR-77-0060, HAES Report No. 61, 15 Feb 77.

13. A. Omholt, The Optical Aurora, Springer, Berlin 1971.

14. G. G. Shepherd and E. V. Pemberton, Radio Sci. <u>3</u>, 650 (1968).

15. W. P. Reidy et al., Analysis of HAES Results: ICECAP 72, HAES Report No. 2, DNA 3247, 22 Apr 74.

16. K. Fukunaga, Introduction to Statistical Pattern Recognition, Academic Press, New York 1972.

PIC-88a
1 of 6
+ 4 fig's
(includes
some
material
from
PIC-83)

PhotoMetrics, Inc.

APPENDIX II

MEMORANDUM

DATE: 8 May 1978

TO: A. T. Stair, Jr., E. R. Huppi/OPR

FROM: I. L. Kofsky, R. H. Johnson

SUBJECT: – Infrared Sky Backgrounds   and
– Sample KC-135 Aircraft Flight Plans
for 26 Feb 79 Total Solar Eclipse

This note follows up our quick-look memo of 24 Jan 78, which suggested measuring zenith intensities of OH ($\Delta v = 1$) and $O_2{}^1\Delta$ (best S/N in 0, 0 band) airglows with the existing aircraft instruments during the forthcoming eclipse.[*] The purpose of these spectroradiometric measurements is to determine concentrations of species that participate in the reactions that control the ionosphere's electron and ion densities, and so contribute to "data sets" considered necessary for modeling the ionosphere's response to disturbances. (General reference on application of the data: W. Berning, The Solar Eclipse of 26 February 1979, Report on SRI project 6308, Nov 1977, unnumbered. "Geometry" of the eclipse is in US Naval Observatory Circular No 157, 05 Dec 77.) It provides planning data for viewing the emitting layers when they lie within the umbra and when they are partially illuminated, from the aircraft within the umbra.

The specific questions addressed are 1) the background radiant intensity of the sky in the short-wavelength infrared, and 2) positioning of the aircraft to achieve measurement goals. Diagrams intended to

---

[*]Briefly summarized, this memo (PIC-83) proposed remote sensing from the aircraft of:

$\underline{O_2{}^1\Delta}$.   Zenith radiance can be measured (in 0, 0 or 0, 1) with the overhead interferometer. The time dependence of column emission rate during totality provides a measure of the initial altitude profile, as the probability of collisional quenching of $O_2{}^1\Delta$ molecules increases with decreasing altitude.

$\underline{OH}$.   Radiance in vibrational fundamental and overtone should be detectable during totality by both interferometers and radiometers. The system intensity measures column integral of $[HO_2] \cdot [O]$ and/or $[H] \cdot [O_3]$ rather than [ground-state OH], and also provides a measure of mesospheric $[H_2O]$. The eclipse provides a unique opportunity for looking at daytime OH Meinel band emission.

$\underline{Mesosphere\ temperature.}$ Can be determined from the rotational line ratios in OH $\Delta v = 1$ or 2, measured by the zenith interferometer.

PL PHOTOMETRICS, INC.

improve understanding of the geometry and movement of the three-dimensional, near cylindrical region of totality are included. The conclusions are, that the scattered-light background is very low but expensive to predict quantitatively, and that the eclipse permits viewing of un-illuminated airglow altitudes for ~2 min and < 4% solar-illuminated altitudes for ~1 min (with the platform in the umbra).

1. Background spectral radiance within the umbra. Several sources contribute to the radiation from the upper hemisphere during totality. Principal among these are:

  a) solar photons that in-scatter (from the partially-illuminated penumbra), and then scatter a second time in the direction of the detector;

  b) solar photons singly-scattered from air molecules at altitudes above the umbral volume (which also lie in the penumbra);

  c) photons originating from the sun's coronal continuum that singly scatter in the umbra;

  d) thermal emission by atmospheric molecules;

  e) starlight, and to a lesser extent zodiacal light; and

  f) chemiluminous and photon-excited emissions, for example $O_3 + H \rightarrow OH\dagger + O_2$ and $h\nu + O_3 \rightarrow$ metastable $O_2{}^3 1\Delta + O$ respectively.

(d), (e), and (f) are the nighttime radiation sources familiar from previous aircraft measurements; and (f) is the signal the spectro-radiometer would be trying to resolve from backgrounds (a) through (e).

Source of sky radiation (a), recently reviewed in detail by G. Shaw (Applied Optics 17, 272 (15 Jan 78)), is dominant at wavelengths below $\sim 1\frac{1}{2}\mu m$ when the observer is near the center of the umbra. Its spectral intensity falls off very steeply with increasing wavelength because of the decreasing probability of double-scattering(with an inverse power of λ).   This radiance also varies with the following factors:

zenith angle:	flat minimum ir the zenith
solar elevation:	decreases with decreasing e l (perhaps)
umbra radius:	decreases with increase
location in umbra:	see below, radiation transfer calculations needed
altitude:	small (!) decrease to A.C flight level
dust, clouds:	can either increase or decrease, as can the brightness of the natural sky.

146

P1 PHOTOMETRICS, INC.

Model figures for the zenith of a clear atmosphere (from the above-referenced paper, considering double scattering mechanism (a) only) with the observer near the center of the umbra, are: 500 R/Å at 6300 Å, and $2\frac{1}{2}$ R/Å or 3 x 10^{-10} w/(cm^2 ster μm) at 1.27μm. In contrast the zenith airglow in the 1.27μm O_2 $^1\Delta(0,0)$ band viewed from aircraft altitude is 5 x 10^6 R(photodissociation-luminescence) by day, 3 x 10^4 R (recombination-chemiluminescence) by night. The daytime-sky continuum near 1.27μm is about 10^6 R/Å, or about six orders of magnitude above the eclipsed-sky continuum near 1.27μm is about 10^6 R/Å, or about six orders of magnitude above the eclipsed-sky's calculated spectral intensity.

As the aircraft moves nearer the edge of the umbra these continuum brightnesses tend to increase, both because of increased intensity of double-scattering and, toward the edge of the umbra away from the sun, single-scatters of type (b). (The geometry of these latter scatters is illustrated later, in Fig 2.) Qualitatively speaking, however, the infrared backgrounds remain "low" because of the low Rayleigh (and Mie) scattering cross-sections and weakening solar spectral irradiance toward longer wavelengths.

This conclusion is supported by J. Cahill and J. Rex's partially-reduced 07 Mar 70 eclipse sky-radiance data on p 135 of the 1970 Aspen Fourier Spectroscopy Conference report, AFCRL-71-0019. These data show only noise looking away from the solar corona at wavelengths between the interferometer's cutoff at 1.3μm and the CO_2-H_2O atmospheric thermal emission band beginning near 2.4μm (a background source of type (d)). Looking directly at the corona from aircraft altitude, the equivalent spectral "radiance" 1.3 - 2.4μm was comparable to that in the 2.7μm thermal-emission band (p 136). The angular response of the spectrometer is greater than the effective angular extent of the corona, whose surface brightness falls off very rapidly away from its maximum at the sun's limb. The latter is usually observed to be 10^{-6} w/cm^2 ster μm. Since the steradiance of scattered skylight would be $\sim 10^{-5}$ that of this narrow-corona source — (c) in the list above —, background due to coronal-scatter above 1.3μm is of the order of the starlight background — (e) — between 1 and 3μm. (Occasional solar prominences during the course of totality might produce about 10x this intensity confined in narrow H emission lines at 1.090, 1.2817, 1.8751, 2.630, and 4.050μm.)

Contrary to previous expectations, during totality the brightness of the sky in the visible is only about a factor 2 lower at the aircraft's operating altitude than at ground level. This small decrease predicted by Shaw's radiation-transport model shows in a comparison of data that we took from A/C 53120 with the 10 narrow-wavelength-band photometer at the 10 Jul 72 Hudson's Bay total eclipse (in Section V of AFCRL-TR-74-0142, Mar 73) against ground data taken at the Kenya eclipse in 1973 (in Shaw's paper). Thus pushing the aircraft to a few km higher altitude results in only a very small decrease of the

PhotoMetrics,INC.

scattered radiation background, though of course it reduces the backgrounds from thermal H_2O - CO_2 emissions.

All factors considered, we judge it safe to conclude that

- the near-zenith spectral radiance in the eclipse umbra at wavelengths > 1.1μm is sufficiently close to that of the night sky ($SZA > 100^O$) to allow the usual nighttime infrared-airglow measurements to be made, both from the aircraft and ground stations.

On the other hand, the actual radiance values are non-intuitive and the radiation transport calculations complex. That is,

- reliable, quantitative model data on the sky's spectral radiance distribution from the aircraft (and any ground station), as a function of position within the moving umbra and parametrized for aerosol-dust-clouds, would require considerable effort to derive.

As soon as the aircraft passes into the penumbra, the sky brightness becomes dominated by singly-scattered photons from the unobscured portion of the solar disk. Some infrared airglow measurements could be made from within the penumbra (provided, or course, that flare from direct sunlight striking the instruments and its windows is under control). For example, when 1/100 of the visible disk area is showing (we neglect limb darkening-brightening effects), which occurs about 1 min after third contact or before second contact, the zenith spectral radiance near 1.27μm jumps to 2×10^{-6} w/(cm^2 ster μm) or $1\frac{1}{2} \times 10^4$ R/Å. This figure should be compared to the aforementioned O_2 $^1\Delta$ (0, 0)-band radiances of 5×10^6 R day and 3×10^4 R night. At 1.58μm the zenith continuum radiance is about 5×10^3 R/Å at this time. Compare intensity of the OH (4, 2) band, nominally 70×10^3 R in narrow rotational lines spread over about 1000 Å; and the O_2 $^1\Delta$ (0, 1) dayglow, 200×10^3 R over ~200 Å.

2. **Flight plans** for viewing the dark and partially-illuminated mesosphere. Please refer to Fig 0 (based on Fig 1 of the SRI report) for a view of the projection of the umbra at ground level. The center-line of this area is moving northeastward at ~780 m/sec. Its essentially elliptical shape is a result of the projection of the virtually-cylindrical obscured volume onto a near-flat earth. The axis of this cylinder tilts out of the paper at 26° elevation and 151° azimuth, the direction of the sun-and-moon.

The length of the ellipse's major axis is 290 km at 90 km altitude near points labeled 5 - 6, where duration of totality at sea level reaches its maximum, $2^m 52\frac{1}{2}^s$ to an observer on the mirror axis.

PHOTOMETRICS,INC.

Note that the region 5 - 6 is well within the KC-135's flight range from/ to Pease AFB, NH or Dayton, OH. Totality at the aircraft – which is not the sole consideration for airglow measurements, as will be discussed shortly – could be extended to $3^m 53^s$ by flying at the usual 220 m/sec along minor axis centerline B in Fig 1, which is a detailed map of the area of Manitoba and Ontario in the umbra between 1648 and 1658 UT (1052-1058 local time).

Refer now also to the side views of the umbra, Fig's 2 and 3. Fig 2 is the projection looking along the line of eclipse movement, that is, perpendicular to the ellipse's major axis; and Fig 3 is looking perpendicular to the minor axis from the northwest, that is, toward the sun-and-moon's azimuth. Each figure is a projection of the cylindrical eclipsed shadow into the page; Fig's 0 and 1 are also projections, in the (vertical) direction perpendicular to both the other two viewing directions. The following analysis is based on the assumptions that the aircraft flies parallel to the shadow's minor axis, and that its radiometers and spectrometers point in the zenith.

The maximum altitude at which the upper edge of the umbra intercepts the aircraft's zenith decreases as the flight path moves from position E to A, as Fig 2 shows. (Fig 2 also indicates that the zenith and northern sky brighten as the aircraft approaches A, because of scattering of sunlight in the nearby penumbra, source (b) above.) All altitudes above 30 km are always partially illuminated from A, which is near the northern edge of totality at the aircraft; while from E, which is 25 km horizontally from the umbra's lower edge, all zenith altitudes below 142 km at least momentarily go into full shadow. To keep the 80-km altitude level always partially illuminated, fly along B; to achieve some complete obscuration below 100 km, fly between D and E.

Suppose, as an example, that the desired airglow measurement cycle were: 90-km airglow level is first partially illuminated, then passes into the umbra, and then is re-illuminated, with the further condition that the aircraft remain in the umbra to achieve adequately low sky background. Fig 3, the view perpendicular to flight on line D (that is, from the northwest; see Fig's 0 and 1)illustrates that the 90-km altitude level would be dark for 118 sec and partially illuminated for 55 sec on both sides of totality at the aircraft's altitude. It also shows that the 100-km level would always lie in the penumbra, and the 80 km level, from above which most of the OH nightglow originates, would be dark for 157 sec and partially illuminated at both ends for $35\frac{1}{2}$ sec. For this measurement sequence, the aircraft would position at D' – 51° 04' N, 95°, 30'W – at 1650:34 UT and fly at 54° azimuth.

(The instruments of course are not always viewing the same air volume, because of the aircraft's forward motion. The calculation could be refined for the trackable interferometric spectrometer, which can maintain pointing at a fixed airglow volume.)

149

PI PHOTOMETRICS,INC.

        Flying along line A, the aircraft would stay in the umbra for 157 sec and the atmosphere would remain partially illuminated down to at least 30 km. This flight path would offer the moderate advantage of increased solar irradiance at the airglow layers, as they lie farther out in the penumbra. A preliminary calculation of the actual illumination, however, shows that it only reaches 3 or 4% full sun when the aircraft lies within the umbral shadow. That is, the solar flux on the airglow is only a small fraction of the uneclipsed flux (exact calculations require consideration of the solar disk's limb darkening, which varies with wavelength of emission).

        The duration of partial illumination at mesosphere altitudes could be furthered "tailored" to measurement needs by flying at an angle to the ellipse's minor axis, or by re-pointing the spectro-radiometers during totality at the 10-km flight altitude. For example a trajectory at 144° azimuth moves the upper edge of the umbra up a maximum of 10 km, while reducing the time during which the aircraft lies in the umbra. Alternatively a trajectory of $144^\circ + 180^\circ$ moves the umbra's edge down 10 km, and also sacrifices measurement time.

Summary

        The background spectral radiance in the infrared during solar eclipse totality does not appear substantively higher than that of the night sky. Although radiation transport calculations would be needed for quantitative planning-predictions, measurement of OH and $O_2{}^1\Delta$ emissions with good signal/noise can be made (from the ground as well as aircraft).

        Fig's 0, 2, and 3 are three perpendicular projections of the near-cylindrical shadow volume that illustrate the geometry of the eclipse, aircraft, and airglow. The times during which the atmosphere's photochemiluminous layers are in the umbra or partially illuminated depend on the separation from the minor axis or "centerline" of the aircraft's flight path in the projection in Fig's 0 and 1. A small $\sim 4\%$ fractional illumination of these layers can be achieved with the aircraft platform in the umbra. An outline of the procedure for adjusting these times, and some typical durations of totality in both the mesosphere and at the aircraft which — are— 2 or 3 min — are presented.

Four figures are attached.

FIGURE 0. PATH OF TOTALITY; SOLAR ECLIPSE OF 26 FEBRUARY 1979

151
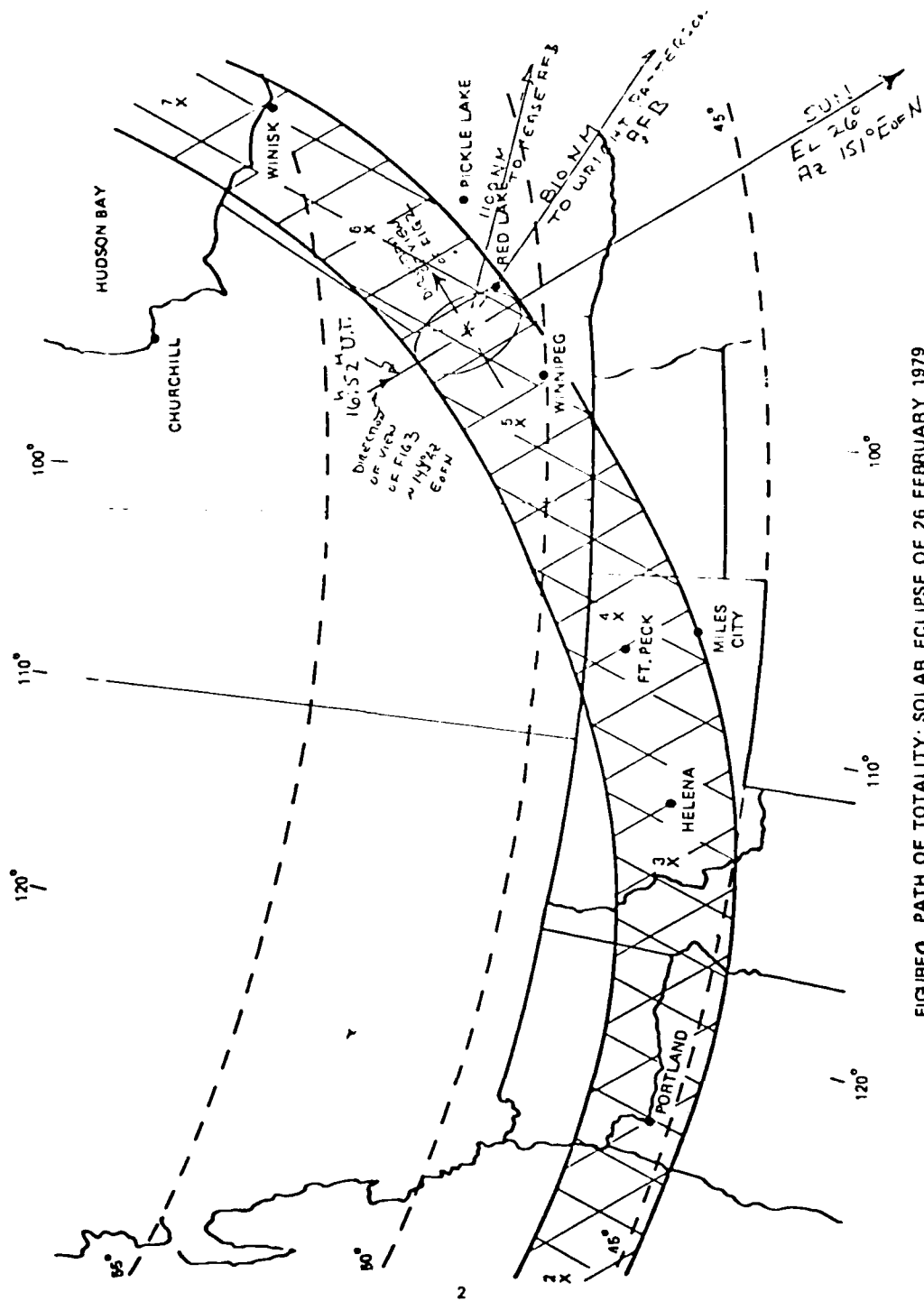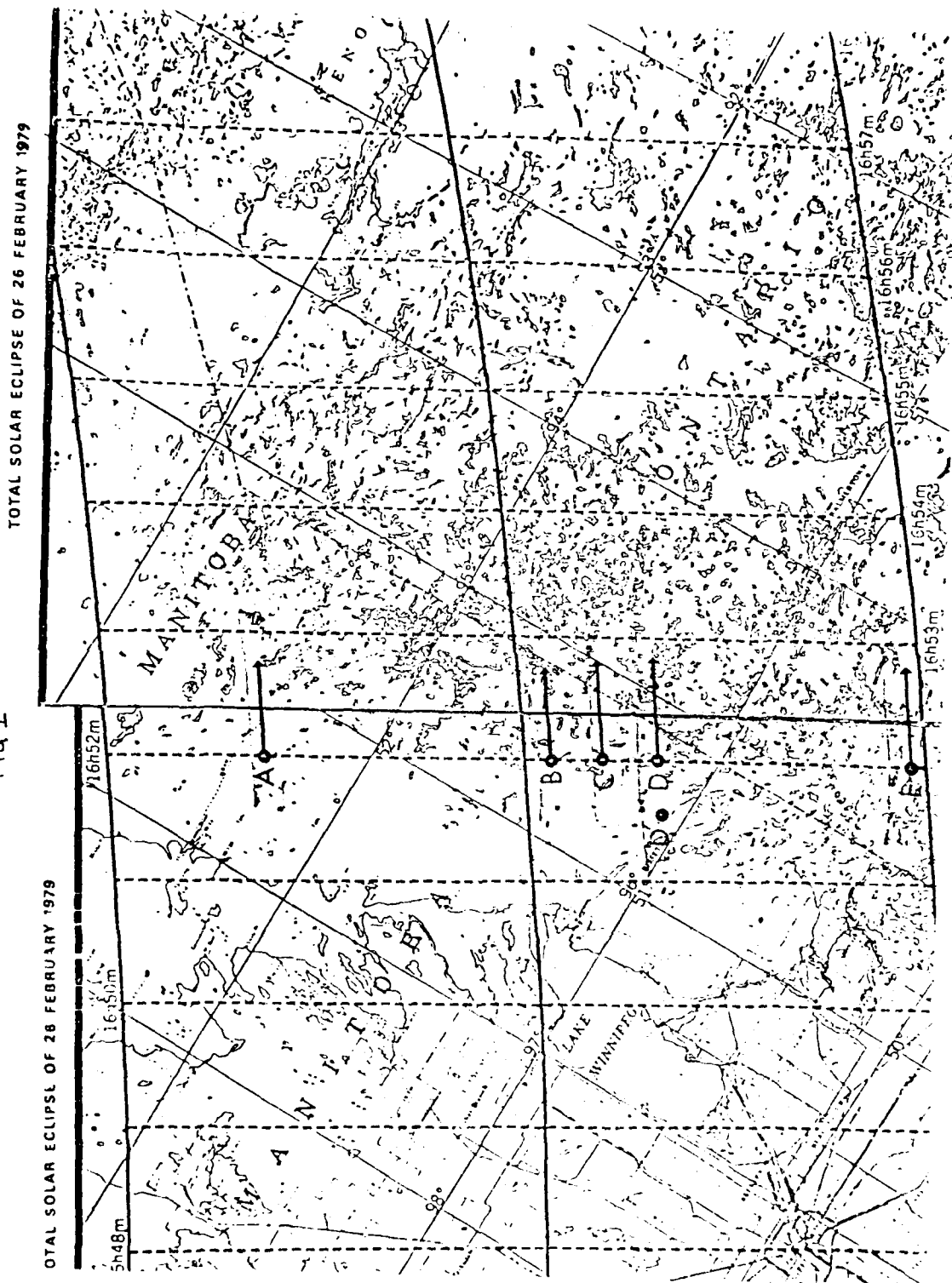
TOTAL SOLAR ECLIPSE OF 26 FEBRUARY 1979

Fig 1

FIG 2

TOTAL SOLAR ECLIPSE - 26 FEB 1979

SIDE VIEW OF ECLIPSE SHADOW - 16h 52m U.T.
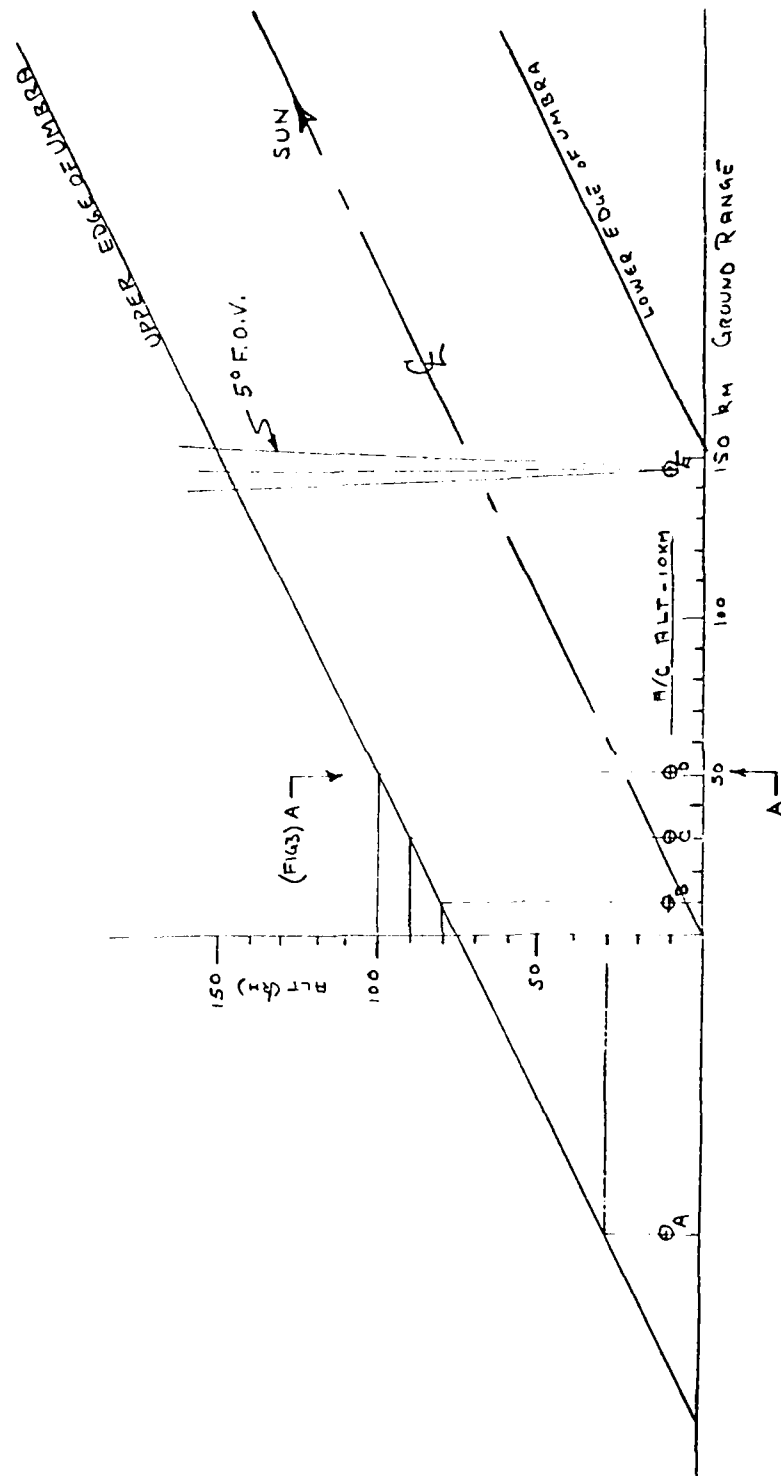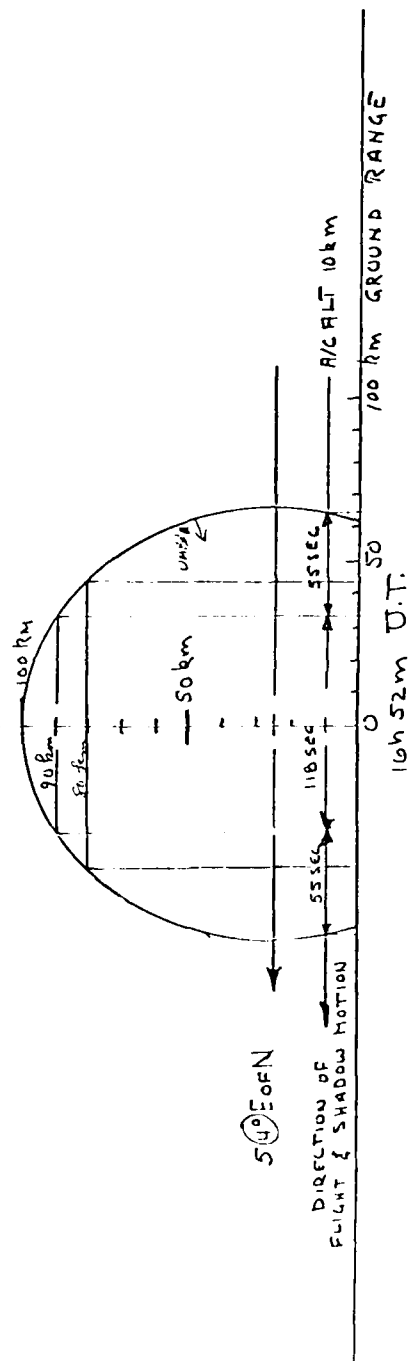
DIRECTION OF VIEW   54° E OF N   (⊥ TO FIG 3)

FIG 3

SECTION A-A (FIG 2) POSITIONS D-D'

TOTAL SOLAR ECLIPSE - 26 FEB 1979 - 16h 52m U.T.

DIRECTION OF VIEW ⊥ TO FIG 2 ~144° E OF N

RELATIVE VELOCITY OF SHADOW TO A/C = 558 m/s

P1 PHOTOMETRICS, INC.

APPENDIX III

MEMORANDUM

DATE: 13 July 1978

TO: A. T. Stair, Jr., E. R. Huppi/OPR

FROM: I. L. Kofsky

SUBJECT: Infrared Emission Data (and Related Nuclear-Effects-
            Simulation Information) from the Artificial Aurora
            Produced by FIREWHEEL

ESA's FIREWHEEL explosive release of ~100 kg Ba + Li in the mag-
netosphere, scheduled for Nov 79, is expected to result in dumping of
~keV electrons   which will produce an artificial aurora in the Alaska
sector.   This energy input offers an opportunity for measuring infrared
output with NKC-135 A/C 53120's instruments.

FIREWHEEL is also a potential source of information about other
aspects of the phenomenology of strategic nuclear explosions – among
them plasma interactions related to coupling, field line trajectories,
magnetospheric perturbations –, some of which could be provided by
the aircraft's instruments. The second technical issue, which I would
expect also to be of interest to DNA/RAAE is only touched on here.
I've also omitted discussion of the use of sounding rockets, even though
the excited volume lends itself to the "small rockets" experiment and
to SPIRE-like IR surveying.

Expected characteristics of the artificial aurora are:

Intensity	5-10 erg/(cm^2 sec) (IBC ~II) for		$\frac{1}{4}$ hr –	
	IBC I	for	2 hr –	

Dimensions 10 km x 200 km E-W –

Velocity   ~50 m/sec W (compare A/C's 220 m/sec)

Latitude   ~Anchorage, 61° Geomagnetic. The release
            will be designed to hold the auroral footprint
            over accessible territory –

Time   Local midnight, between 9 & 26 Nov 79 (alter-
            nate Dec 79, moon-down defines window) –.

G. Haerendel of Max Planck Institute-Garching, who are running
the program for the European Space Agency, tells me that there is a
slim outside chance that the precipitating particle flux could be an
order of magnitude greater. Haerendel, who visited AFGL in June

PhotoMetrics, INC.

(he also talked to ERH & R. O'Neil), was attempting to enlist participation in a large-scale international program of observations of both the aurora and the sunlight-scattering Ba^+ cloud itself (+1 stellar magnitude, 4 kR $\lambda4554$ surface brightness in its $1\frac{1}{4}°$ extent at 10 min after the release).

The benefit to the SWIR structure-sources program is the duration and relative predictability/stability of the auroral form (once it is located; the footprint probably can't be accurately predicted in advance). The spectrometer could track and coadd for ~1 hr; and the radiometers could compile edge traces (for example) to determine infrared-visible spatial correlations for known predosing. We might consider the effect of FIREWHEEL a "no-surprises" aurora, <u>which itself produces an infrared background that might have deleterious effects on spaceborne surveillance systems</u>.

The release would be at $9\frac{1}{2}$ R_e from a transfer satellite orbit. Its exact date is to be determined after the satellite is launched, in part on the basis of good observing conditions (and also on lack of magnetosphere disturbance, which could vitiate the predictions of the footprint and make competing natural aurora). The aircraft could hold on the ground at Pease AFB or W-PAFB if notice of the release is provided ~ $\frac{1}{2}$ da in advance. If the decision to fire is made by 2100 local, base at Fairbanks; if less notice is given, base at Elmendorf (near Anchorage).

Morphological information about the artificial aurora – dimensions and "color" (as determined by the filtered video camera and /or photographic All-Sky camera), electron energy spectrum from the multichannel photometer (and maybe by then the NO^+ intensity !!) – is also wanted. These data of course also relate to the aforementioned magnetosphere-ionosphere physics issues.

Some further information on FIREWHEEL is in a MPI-G report dated 11 Jan 78, a copy of which was left at PHP Branch (we have most of the pertinent pages). Predictions of the auroral footprint's trajectory will be made available later by ESA. The all-sky video can locate the emitting area if it's within ~600 km of the aircraft ($10°$ above the horizon).

<u>To sum up</u>: data taken from 53120 on FIREWHEEL artificial aurora would be of use in DNA's SWIR structure-sources program; and the visible-morphology information also applies toward meeting other DNA goals for validating predictive capability.

PHOTOMETRICS, INC.

APPENDIX IV

MEMORANDUM

DATE: 07 April 1978

TO: Dr. C.A. Blank, DNA/RAAE   FROM: I.L. Kofsky

SUBJECT: Potential Applications of Space Shuttle's Laser Radar
             in Communications-Survivability Investigations

At the time I was finishing my Shuttle reports (DNA 4439F-1 and -2) NASA had accelerated its program of defining investigations to be performed with the facility-grade, multi-user radar probe (lidar) that is to be installed on Orbiter/Spacelab. They organized an international Atmospheric Lidar Working Group, largely an offshoot from AMPS-Atmospheric Science but with several new faces (22 total) that met five times between 22 Sept 1977 and 01 Mar 1978. The last of these meetings was expanded into a pre-proposal conference for a second level definition study for the spacecraft's lidar telescope, which Gil Davidson attended (company funded).

The Working Group had identified about 35 Candidate Shuttle Lidar Measurements to meet seven scientific objectives. None of these object-ives was related directly to understanding deionization in the D region or decay of electron density inhomogeneities in the F region, which is not surprising considering that nobody in the Working Group is expert in these technical issues. Nonetheless we find that some seven of the Candidate Measurements, which I've listed on the attached page, provide altitude profiles of reactive species that are useful in simulation-investigations of the disturbed ionosphere and its effect on communications link performance. [Refer to Appendix V for application of this information.]

The top five measurements in the table are of concentrations of con-trolling "minor" neutral species in the D region. (I should point out that some of these ideas, but not the specific laser/detector types, were already covered in DNA 4439.) The active probing measurements are comple-mentary to the passive limb scanning radiometry described in Appendix V 12 Dec 1977 (PIC-82). This "output" information, which figures in the determination of ion species types and thus the important ion mobility, would not otherwise be available in the proposed Dismedia-propagation program. The time scale of changes of D region species concentrations is sufficiently low to allow use of lidar measurements made from a polar orbiting Shuttle vehicle (separate from the vehicle that measures particle-energy input).

The lower four measurements listed (two overlap) apply to chemistry and dynamics of the disturbed F region. Some of the data also have appli-cation in investigations of processes underlying emissions of infrared radiations, as indicated in the parenthesized entries in the table.

I'd be pleased to review with you further how remote probing of atmo-spheric species with NASA's state-of-the-art lidar can contribute to meeting DNA's information needs. Access to this facility is available to all qualified technical groups, and NASA seems anxious to elicit further users and ideas for applications.

157

Topside Lidar in Simulations of Nuclear Explosion Effects on Communications*

QUANTITY MEASURED	DIFFICULTY	LASER METHOD
O_3 profile 35-50 km, night or day	2	Nd:YAG (x4), DIAL (2650 Å, absorbs); PMT detection
OH profile 30-100 km* ($OH \cdot 2.8 \, \mu$m)	3	Nd:YAG (x2) pumping dye (x2), or UV excimer (resonance fluorescence); PMT detection
O_3, H_2O, CO_2, CO, CH_4, N_2O, NO_2, HNO_3 -- altitudes variable* (various SWIR, LWIR)	3-4	Line-tunable or continously tunable IR laser with refro-reflective subsatellite in limb-occultation orbit; heterodyne detection
NO profile 70-150 km* (atom-interchange)	4	Nd:YAG (x4) pumping dye (x2), or UV excimer (fluorescence in 2265 Å band); PMT detection
O profile 75-180 km*	4	As NO (fluorescence in 2256 Å band)
Mg^+ and/or Fe^+ 80-500 km	2-3	Nd:YAG (x2) pumping dye (resonance fluorescence)
$N_2^*(v)$ profile 80-200 km	3	N_2^+ ion (resonance fluorescence); PMT detection

Left margin (rotated): Controlling-Species concentrations in the D region → -- ELF-VLF-HF --

Left margin (rotated): -- VHF & above -- Electron density irregularities in the F region →

*Also apply in investigations of IR-optical background emissions, as indicated in parentheses.

- - - - - - - - - -

Notes for Table: Nd:YAG refers to currently-available powerful neodymium-yttrium-aluminum-garnet lasers, x2 means frequency doubled. PMT is photomultiplier tube. DIAL refers to the concept of comparing an absorption-line return signal to off-line laser backscatter, to perform a differential measurement of species concentration. Difficulty 2 means expected feasible by 1980, 4 by 1985.

PI PHOTOMETRICS, INC.

APPENDIX V

MEMORANDUM

DATE: 12 December 1977

TO: A. T. Stair, Jr., OPR/AFGL (for RAAE/DNA)

FROM: I. L. Kofsky

SUBJECT: Infrared Remote Sensing of D- and E-Region Conditions
             for DISMEDIA - Propagation Tests

Background

The **proposed** DISMEDIA **satellite investigation has the** function of
measuring the input into the high-latitude ionosphere of energy carried
by hard charged particles, such as those of solar proton and relativistic
electron precipitation events. No systematic onboard measurements
of the output of positive and negative ion species are included in the
original proposal, LMSC-D462422 (July 76). (Some localized free
electron concentration data may be available from rocket flights of
AFGL probes.)

The profiles of concentration and mobility of these ion complexes
in the D region are essential input information for the models of ELF
and VLF propagation; and in addition some diagnosis of E- and F-region
conditions is also needed. Predictive capability of these codes will be
validated against actual communications systems performance during
the natural disturbances. Presumably these important output parameters
will be calculated from code models of the lower ionosphere's aeronomy,
which themselves have only tenuous experimental validation.

The minor neutral species play the major role in controlling con-
centrations of the various ions. It is the purpose of this note to point
out that column-concentrations or altitude profiles of most of these
critical species can be systematically determined by infrared spectro-
radiometry of the type now routinely done by OPR. That is to say,
OPR's capability for determining intensities and spectra of the atmo-
sphere's emissions, so far used for assessing backgrounds encountered
by surveillance systems, can be applied to improve significantly under-
standing of the causal relationship between input of charged-particle
energy (simulating nuclear explosion effects) and performance of long-
haul military communications systems. The infrared measurements
are not merely a support function for the program, but by producing
benchmarks to verify the necessarily-complex aeronomy codes make
a major contribution to the propagation investigation of which DISMEDIA
is a part.

PhotoMetrics, INC.

Some History

In September 1977 DNA/AFGL's "SPIRE" rocket spectrometers successfully surveyed the sunlit and nightside earth limb at wavelengths between 1.4 and $16\frac{1}{2}\mu m$. Emission features of OH, $O_2{}^1\Delta$, O_3, H_2O, NO, HNO_3, and CO_2 were observed, many at intercept altitudes down to at least 40 km. The first five or six of these molecules, along with O and H atoms and the complexes HO_2 and H_2O_2, are the very species whose concentrations co-determine those of ions at D- and E-region altitudes (refer to the list in the paragraph following). SPIRE's high-throughput scanned-filter spectrometers, and the radiometers and higher-resolution interferometric spectrometers fielded by OPR in HAES, TEAL RUBY, BAMM, MSMP, and other DoD measurement programs are representative of OPR's capability for infrared remote sensing of thermally-emitting and chemiluminous atmospheric molecules. (The concentrations of the ions themselves are too low to allow direct measurement of their emissions.)

The expected changes in concentrations of these (and other) emitting species under solar proton event bombardment, and applications of remote optical/IR sensing for diagnosing ionosphere conditions during and after the disturbance, were reviewed in connection with an evaluation of the optical data taken in DNA's PCA '69 Composite Study (in AFCRL-TR-74-0476, by I. Kofsky and J. Schroeder: Visible and Infrared Radiations from the Atmosphere Accompanying PCA Events, Sept 74; a copy is appended[*]). This work was performed for DNA under the direction of W. Swider of LKB branch, who has had responsibility for evaluating AFGL's (R. Narcisi) mass spectrometric data on this and other ionosphere disturbances. Swider has recently reviewed (in Cospar Space Research Vol XVII, 1977; an annotated copy is appended[*]) the impact of the optically-detectable neutrals on concentrations of ion species. His conclusions, which reflect what is in DNA's lower-ionosphere aerochemistry models (M. Scheibe, Ali/Niles, Ory/Gilmore) may be very roughly summarized as follows:

O_3 — important in negative ion chain, both speeds processes and destroys ions (refer, for example, to negative ion reaction paths plot in E. E. Ferguson's paper in Atmospheres of the Earth and Planets, Reidel, Dordrecht, 1975)

$O_2{}^1\Delta$ — directly photoionized by solar UV, and collision-ally detaches electrons from O_2^-; also serves as monitor of $[O]$ and $[O_3]$

OH — with HO_2, controls $[O]$ and thus $[O_3]$

NO — its photoionization by Lyman-α is the main source of the quiet D region's ionization; also plays a part in negative ion reactions

---

[*] to original submission to AFGL.

PhotoMetrics, INC.

O   – interferes with oxonium production chain by
reacting with O_4^+; important in negative ion
chain; in equilibrium with O_3 by day

H_2O – source of oxonium ions, $H^+(H_2O)_n$, the
dominant positive species (at least above ~60 km)

HNO_3 – believed to be a clustering agent for negative ions.

Passive Infrared Remote Sensing

We consider here only IR/optical passive sensing of column con-
centrations and altitude profiles (and some temperatures) as performed
using AFGL/OPR's existing spectroradiometer types viewing from
orbiting satellites such as DISMEDIA's vehicle itself or Space Shuttle.
Altitude profiles are derivable from scans through the atmosphere's
limb, and in some cases with the help of models, from data taken staring
at the nadir. (Useful optical measurements of the ionosphere's chemical
state can also be made systematically from ground stations and more
sporadically from jet aircraft, balloon, and sounding rocket platforms.)
Further data on D-region conditions, not specifically discussed, can be
derived from more sophisticated optical procedures. These include
detailed inversions of high-resolution spectra – a method well proven
on Nimbus satellites for determining temperature profiles down to the
~ millibars level; active probing using laser-backscatter telescopes –
as will be done from Spacelab*;and measuring the extinction of radiation
from extraterrestrial sources – which showed the unexpected large PCA '69
decreases in D-region $[O_3]$ (L.Weeks, J. Atmos. Sci. <u>29</u>, 1138 (1972)).

We review the emitting minor species in the order of the list above,
with the wavelength bands that carry information about their concentra-
tions and – the quantity of importance to DISMEDIA-focused investigations –
the ion and other species whose concentrations they control by aero-
chemical reactions. These emissions are thermal or photochemi-
luminous, rather than directly fluorescent; that is, <u>they measure the
output state of the ionosphere's D- and E-layers,</u> rather than the
immediate rates of energy input by the incident hard particles.

<u>O_3</u>   --1) $O_2\,^1\Delta$ emission by day, 1.27 and 1.58μm,
           measures the column-concentration of
           O_3 to altitudes as low as 30 km
           (as solar photons $+ O_3 \rightarrow O_2\,^1\Delta + O$;
           refer to Table 7a of TR-74-0476).

         1a) Altitude profiles of O_3 can be determined
            directly from the twilight dependence of
            column emission in an $O_2\,^1\Delta$ band
            (W. Evans & E. Llewellyn, Radio Sci. <u>7</u>,
            45 (1972)).

---

*Refer to Appendix

Pl] PHOTOMETRICS, INC.

2) Hydroxyl Meinel-band vibrational emission, ~ 1.3-2.2 and 2.8-$3.7\mu m$, provides a measure of the nighttime ozone concentrations between ~ 75 and 95 km (from reaction $O_3 + H \rightarrow OH^\dagger + O_2$). The daytime OH emission may be excited by other processes, as SPIRE has indicated (the spectrum appears different from that in the dark ionosphere).

3) $O_2\,^1\Sigma$ emission, 0.864 and $0.762\mu m$, gives the same type of information as $^1\Delta$ emission, with lower precision (Section V of TR-74-0476).

4) Limb profiles of thermal radiation from O_3 in the vibrational fundamental at $9.6\mu m$ and (101-000) combination band near $4.74\mu m$, provide another measure of ozone altitude profiles (hot-band emission longward of $9.6\mu m$ is _not_ expected to change in SPE's).

$O_2\,^1\Delta$ --1) Daytime profiles down to ~ 30 km can be inferred from the 1.27 or $1.58\mu m$ radiances, as in Item O_3 1), above. The $O_2\,^1\Delta$ concentrations are expected to peak near 60-70 km altitude.

2) Nighttime intensity provides a measure of the O atom column concentrations near the peak at 97 km, from $O + O\,(+M) \rightarrow O_2\,^1\Delta\,(+\,M)$. The $O_2\,^1\Sigma$ and $^3\Sigma$ states can also be populated in this recombination reaction. With sufficient spectral resolution to determine rotational line intensities in the $^1\Sigma$ or $^1\Delta$ band systems, the temperature of the ionosphere at ~ 97 km could be determined.

OH --1) Nighttime Meinel-band intensity measures the $[H]\,[O_3]$ product, summed over the altitude of emission. (Note: Nuclear explosions at certain altitudes will quench hydroxyl emission for hours by photodissociating mesospheric O_3: I. Kofsky, J. Geophys. Res. **67**, 739 (1962)).

2) The ratio of rotational line intensities, which can be straightforwardly measured in any one of several IR and long-wavelength-visible vibration bands, determines the ionosphere's temperature near ~ 85 km (at night).

PN PHOTOMETRICS, INC.

NO -- Column-concentrations can be remotely sensed
by four characteristic radiations, in order of
decreasing wavelength
1) $5.3\mu m$ (1,0) vibrational band from resonance
scattering of earthshine (dominates at alti-
tudes $\lesssim 117$ km) and O atom interchange
($\gtrsim 117$ km)

2) Continuum I, extending to $\sim 2\mu m$, from the
NO + O reaction, whose emission is in a
narrow region centered near 95 km altitude

3) Continuum II, above $0.5\mu m$, from the
$NO + O_3$ reaction, the weak emission from
which is thought to peak in the stratosphere

4) Sunlight fluorescence, in the ultraviolet
and thus not considered here.
Altitude profiles can be derived, in a limited
altitude range, from limb scans in the $5.3\mu m$ band.

O -- As noted above, concentrations near the [O]
peak at night can be inferred from the atmo-
sphere's radiance in the O_2 $^1\Delta$ and O_2 $^1\Sigma$ bands.
Both $0.5577\mu m$ photons and near-ultraviolet
Herzberg I bands also result from oxygen
recombination; the airglow's limb profile in the
former feature has been measured from the
OGO-6 satellite to determine O-atom concen-
tration profiles above the peak near ~ 97 km.

H_2O -- Altitude profiles of water vapor down to the
stratosphere can be derived from unfolds of
the spectral distribution of nadir thermal
radiance in the $6.3\mu m$ band. High spectral
resolution is needed for this measurement.
The water vapor concentrations are expected
to vary with season of the year.

HNO_3 -- Profiles of this lower D-region species can be
determined from limb scans of its thermal
emission just above $11\mu m$.

In addition information about at least one other minor neutral species may
be derived from infrared airglow intensities.

HO_2 -- Daytime concentrations over some altitude range
would be proportional to some of the hydroxyl
band intensities, provided that the $HO_2 + O$
reaction is a source of $OH^{\ddagger}$ (as expected).

PhotoMetrics, inc.

A Note on Detection of Dynamics Effects

Atmosphere-dynamical phenomena are thought to accompany solar proton events, on the basis of the observation of intense gravity waves by A. Faire in PCA '69, variations in F-region neutral densities derived from satellite orbital data at times of other SPE's, and an oscillatory behavior in the zenith OI $0.63\mu m$ nightglow during PCA '69. An effect (p 70-72 of TR-74-0476) of dissipation of atmospheric wave energy is to raise the turbopause, mixing O atoms downward and thus altering ion mobility profiles near the top of the D-region by interfering with production of oxonium. Most of the odd O atom-dependent airglows noted above would be enhanced, and their profiles lowered, if the turbopause were raised during the solar proton events on which DISMEDIA will be concentrating. In addition traveling compressional waves would show directly as spatial-temporal changes in airglow and thermal radiances. Thus infrared radiometry of the disturbed ionosphere also monitors the dynamic effects and potential instabilities induced by the geophysical event, which could be impacting radiowave propagation.

Summary, Ranking of Diagnostic Measurements

The passive remote sensing of neutral species column-concentrations, profiles, and temperatures discussed here could be effectively performed with OPR's existing types of infrared spectrometers and radiometers. As noted, some UV and visible emissions also provide useful diagnosis of the chemical state of the disturbed ionosphere medium. Attention is directed to the fact that more specialized infrared instruments could determine other species that might be playing a part in the aeronomy, in particular HNO_3 up to the mesosphere, CH_4, CO, H_2O_2, and NO_2; and that other investigators may have alternative interpretations of the impact of the various neutral molecule concentrations.

A rough, subjective ranking of the perceived applicability of infrared-radiance information is as follows.

Most Useful: $O_2{}^1\Delta$ radiance by day −

Twilight dependence of $O_2{}^1\Delta$ column emission −

Hydroxyl-bands limb profiles, daytime and nighttime −

O_3 vibrational-bands limb profiles −

NO fundamental-band profiles −

Water vapor profiling.

PHOTOMETRICS, INC.

Moderately Useful:	Temperatures determined from ratios of OH rotational lines —
	HNO_3 concentrations.
Least Useful: (or least resolution in measurement)	Nighttime $O_2 \, ^1\Delta, ^1\Sigma$ intensities for E-region O concentrations —
	NO continuums intensities.

A Table briefly summarizing the applications in ionosphere diagnosis of the several infrared-active nuclear species is appended.

Information About Lower-Ionosphere Conditions Derivable from Infrared Emissions

Item	Quantity	Species	Wavelengths, μm	Perceived Usefulness, Comments
1	$[O_2{}^1\Delta]$, daytime	$O_2{}^1\Delta$ O_3	1.27, 1.58 4.74, 9.6	High. The profile can also be determined from twilight $O_2{}^1\Delta$ intensity variation
2	$[O_3]$ and $[O]$	$O_2{}^1\Delta$ O_3	As Item 1.- As Item 1.-	[O] in the E-region can also be estimated from other airglows (Item 9-10)
3	$[O]$	OH	1.3-2.2, 2.8-3.7	High. Measurements have good S/N
4	$[NO]$	NO	5.3-5.5	High. Also measurable from emission at other wavelengths, with poorer S/N
5	$[H_2O]$	H_2O	6.3 region	Moderate-High. Good spectral resolution required. Seasonal variations expected
6	$[HO_2]$ day	OH	As Item 3	Moderate. Interpretation of daytime hydroxyl emission is incomplete
7	$[OH], [H]$	OH	As Item 3	Moderate. Interpretation incomplete, altitude region limited
8	Temp ~85 km	OH	As Item 3	Moderate. Measurement resolution good, both interpretation and applicability of data in question
9	Temp ~97 km	$O_2{}^1\Sigma$, $O_2{}^1\Delta$, $O_2{}^3\Sigma$, O^1S	SWIR-Vis, UV	Low. Measurement resolution poor, applicability of data limited
10	$[O]$, night	As Item 9	As Item 9	Low. Applicability of data somewhat limited.
11	$[HNO_3]$	HNO_3	11.3μm	Moderate. Mostly stratospheric.

* The daytime concentration of O atoms is expected to follow that of O_3 molecules.

APPENDIX VI

OH $^2\pi$ VIBRATIONAL FUNDAMENTAL (MEINEL-BAND) SPECTRA

Fig 1 is a corrected and annotated version of the emission spectrum of the hydroxyl airglow originally given in Fig 4 of Ref 2 (HAES 27), calculated with PhotoMetrics' AIRSPEC computer program. Due to a formatting error, the (1, 0) R branch had been omitted and some of the line intensities in other bands were incorrect in the earlier version. Input parameters remain those listed in Table 1 of Ref 2, with rotational temperature 213 K and photon intensities in each band as given by A. Vallance Jones in Space Sci. Rev's 15, 355 (1973) (150 kR (1, 0), 87 kR (2, 1), 45 kR (3, 2), 21 kR (4, 3).) Zenith energy intensities are normalized to the maximum of 0.903×10^{-10} w/cm^2-ster in the (1, 0) P_2 (3) line at 3465 cm^{-1} ($16\frac{1}{2}$ kR at 2.89μm).

Fig 2 shows this hydroxyl spectrum after attenuation by the atmosphere above 9 km (30 kft, the nominal NKC-135 aircraft operating altitude), calculated line-by-line with the high latitude winter model given by R.A. McClatchey et al in AFCRL-TR-73-0096 (26 Jan 73). The ordinate is in units of 0.902×10^{-10} watts/cm^2 ster in 1 cm^{-1} "bins."
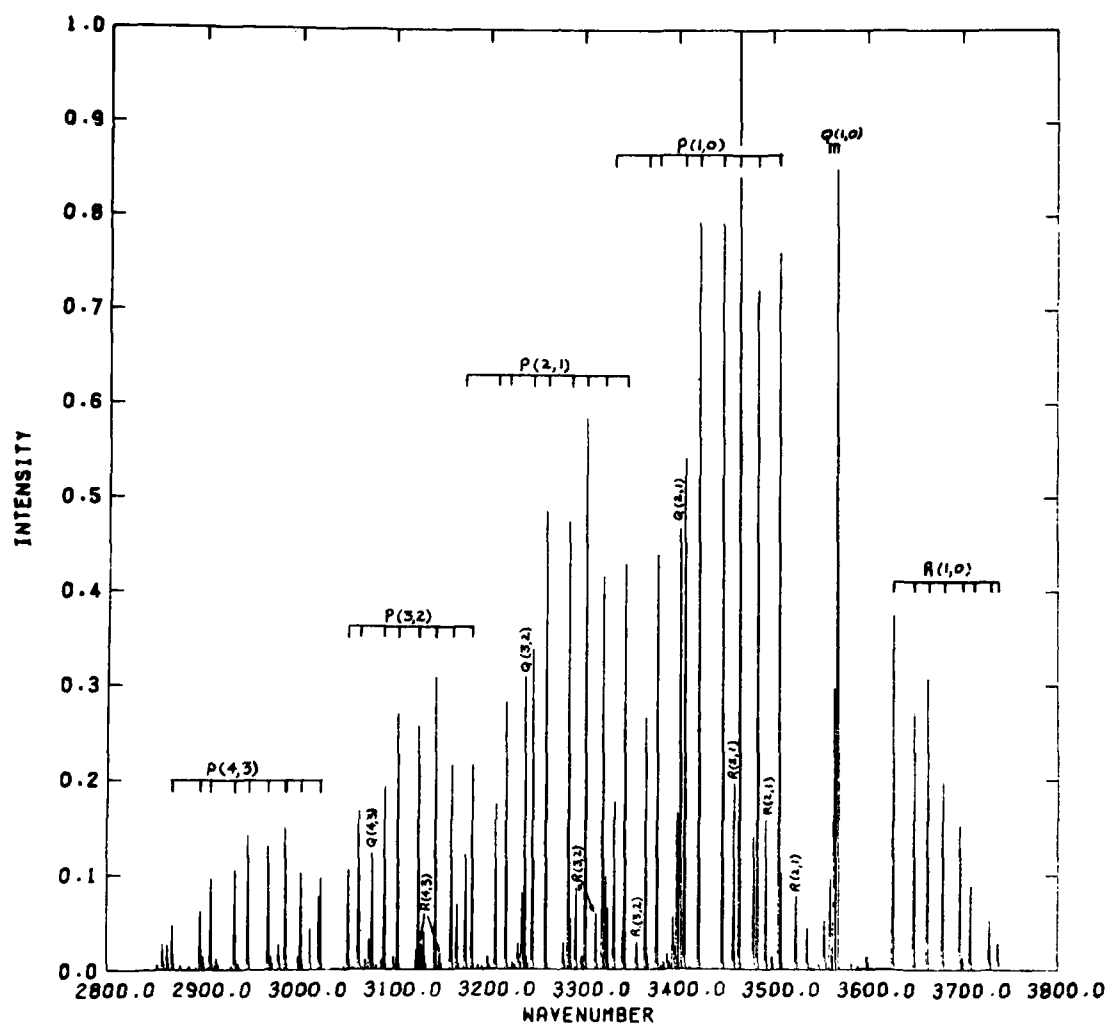
Fig 1. OH airglow spectrum before attenuation by the atmosphere. Intensity units are 0.903 x 10^{-10} w/ster-cm^{-1} bin.
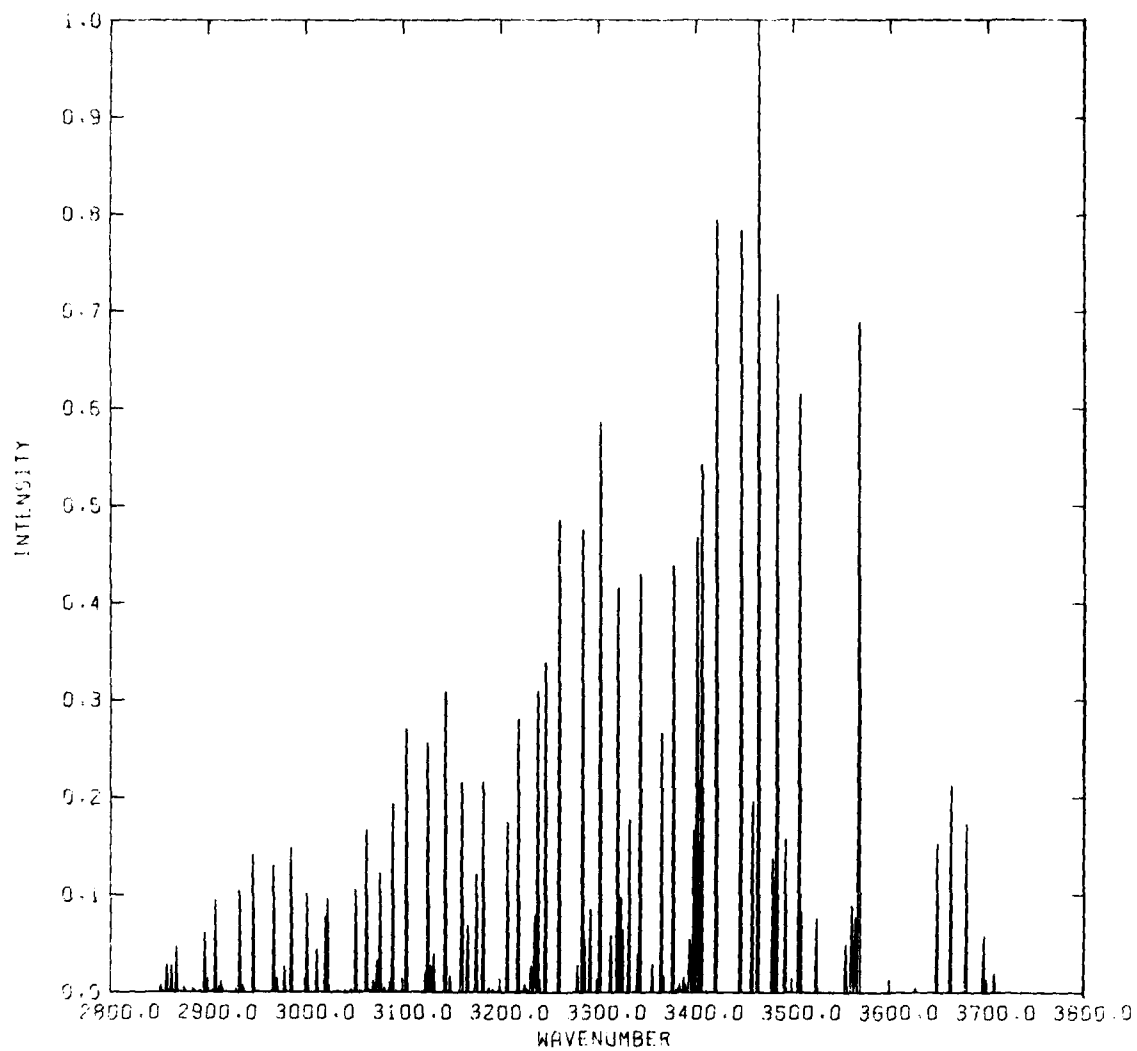
Fig 2 .   OH airglow spectrum transmitted through the high-latitude
           winter model (zenith) atmosphere to 9 km altitude, units
           as Fig 1 .

DISTRIBUTION LIST

DEPARTMENT OF DEFENSE

Assistant to the Secretary of Defense
Atomic Energy
      ATTN: Executive Assistant

Defense Advanced Rsch. Proj. Agency
      ATTN: TIO

Defense Technical Information Center
12 cy ATTN: DD

Defense Nuclear Agency
      ATTN: RAAE, P. Lunn
      ATTN: H. Fitz, Jr
      ATTN: RAAE, W. McKechney
      ATTN: DDST
4 cy ATTN: TITL

Field Command
Defense Nuclear Agency
      ATTN: FCPR

Field Command
Defense Nuclear Agency
Livermore Division
      ATTN: FCPRL

Undersecretary of Def. for Rsch. & Engrg.
      ATTN: Strategic & Space Systems (OS)
      ATTN: Defensive Systems

DEPARTMENT OF THE ARMY

Atmospheric Sciences Laboratory
U.S. Army Electronics R&D Command
3 cy ATTN: DELAS-EO, F. Niles
3 cy ATTN: DELAS-EO-ME, K. Ballard

BMD Advanced Technology Center
Department of the Army
2 cy ATTN: BMDSC-HW

Deputy Chief of Staff for Rsch., Dev. & Acq.
Department of the Army
      ATTN: DAMA-CSS-N
      ATTN: DAMA-CSZ-C
      ATTN: DAMA-WSZ-C

Electronics Tech. & Devices Lab.
U.S. Army Electronics R&D Command
      ATTN: DELET-R, S. Kronenberg
      ATTN: WPNS Effects Section
5 cy ATTN: DRSEL

Harry Diamond Laboratories
Department of the Army
2 cy ATTN: DELHD-N-P

U.S. Army Ballistic Research Labs.
      ATTN: DRCAR-BLB, J. Mester
      ATTN: DRDAR-TSB-S

U.S. Army Foreign Science & Tech. Ctr.
      ATTN: DRXST-SD

U.S. Army Nuclear & Chemical Agency
      ATTN: Library

DEPARTMENT OF THE ARMY (Continued)

BMD Advanced Technology Center
Department of the Army
      ATTN: ATC-O, W. Davies
      ATTN: ATC-T, M. Capps

U.S. Army Research Office
2 cy ATTN: R. Mace

DEPARTMENT OF THE NAVY

Naval Electronic Systems Command
      ATTN: PME 117-20

Naval Intelligence Support Ctr.
      ATTN: Document Control

Naval Ocean Systems Center
      ATTN: Code 5324, W. Moler

Naval Postgraduate School
      ATTN: Code 0142
      ATTN: Code 1424

Naval Research Laboratory
      ATTN: Code 6707, J. Davis
      ATTN: Code 2627
      ATTN: Code 6750, D. Strobel
      ATTN: Code 7122, D. McNutt
      ATTN: Code 6700, T. Coffey
      ATTN: Code 6780, S. Ossakow
      ATTN: Code 7175, J. Johnson
      ATTN: Code 6780, J. Fedder
      ATTN: Code 6709, W. Ali
      ATTN: Code 6701, J. Brown

Naval Surface Weapons Center
      ATTN: Code X211
      ATTN: Code F31

DEPARTMENT OF THE AIR FORCE

Aeronautical Systems Division
Air Force Systems Command
      ATTN: ASD/YH-YEF, Capt Guice

Air Force Geophysics Laboratory
      ATTN: OPR, A. Stair
2 cy ATTN: OPR, J. Kennealy
2 cy ATTN: LKD, R. Narcisi
2 cy ATTN: LKO, R. Huffman
2 cy ATTN: OPR, R. Murphy
5 cy ATTN: LKB, K. Champion
5 cy ATTN: OPR-1, J. Ulwick

Air Force Systems Command
      ATTN: SDR
      ATTN: DLTW
      ATTN: DLXP
      ATTN: Technical Library
      ATTN: DLAE
      ATTN: DLS

Air Force Technical Applications Center
      ATTN: Technical Library
      ATTN: TD
      ATTN: TF

Preceding Page Blank

DEPARTMENT OF THE AIR FORCE (Continued)

Air Force Weapons Laboratory
Air Force Systems Commandd
    ATTN: SUL

Deputy Chief of Staff
Research, Development & Acq.
Department of the Air Force
    ATTN: AFRDS
3 cy ATTN: AFRDQ

Foreign Technology Division
Air Force Systems Command
    ATTN: SDEC, A. Oakes

Rome Air Development Center
Air Force Systems Command
    ATTN: OCSA, J. Simons

Headquarters Space Division
Air Force Systems Command
3 cy ATTN: WE

Headquarters Space Division
Air Force Systems Command
    ATTN: DYS, Space Defense Systems

Headquarters Space Division
Air Force Systems Command
    ATTN: SZJ, L. Doan

Headquarters Space Division
    ATTN: YN, P. Sivgals

DEPARTMENT OF ENERGY

Department of Energy
    ATTN: Document Control for OMA

DEPARTMENT OF ENERGY CONTRACTORS

Lawrence Livermore Laboratory
    ATTN: Document Control for L-262, D. Wuebbles
    ATTN: Document Control for L-71, J. Chang
    ATTN: Document Control for L-10, H. Kruger
    ATTN: Document Control for L-48, E. Woodward
    ATTN: Document Control for L-262, W. Duewer
    ATTN: Document Control for L-325, G. Haugen

Los Alamos Scientific Laboratory
    ATTN: Document Control for MS362
    ATTN: Document Control for E. Jones
    ATTN: Document Control for G. Barrasch
    ATTN: Document Control for R. Jeffries
    ATTN: Document Control for Librarian
    ATTN: Document Control for G. Davis
    ATTN: Document Control for M. Sandford
    ATTN: Document Control for R. Carlos
    ATTN: Document Control for M. Pongratz
    ATTN: Document Control for H. Argo

Sandia Laboratories
    ATTN: Document Control for Org. 1250, W. Brown
    ATTN: Document Control for M. Kramm
    ATTN: Document Control for 3141
    ATTN: Document Control for L. Anderson

Sandia Laboratories
Livermore Laboratory
    ATTN: Document Control for T. Cook

OTHER GOVERNMENT AGENCIES

Central Intelligence Agency
    ATTN: OSI/NED

Department of Commerce
National Bureau of Standards
    ATTN: A. Phelps

Department of Commerce
National Bureau of Standards
    ATTN: M. Krauss
    ATTN: S. Abramowitz
    ATTN: J. Devoe
    ATTN: K. Keesler

Department of Commerce
National Oceanic & Atmospheric Admin.
Environmental Research Laboratories
3 cy ATTN: F. Fehsenfeld
3 cy ATTN: E. Ferguson

Institute for Telecommunications Sciences
National Telecommunications & Info. Admin.
    ATTN: W. Utlaut
    ATTN: G. Falcon

NASA
Goddard Space Flight Center
    ATTN: Code 6801, A. Tempkin
    ATTN: Technical Library
    ATTN: Code 900, J. Siry
3 cy ATTN: A. Aiken

NASA
George C. Marshall Space Flight Center
    ATTN: W. Oran
    ATTN: C. Balcher
    ATTN: W. Roberts
    ATTN: N. Stone
    ATTN: J. Watts

NASA
    ATTN: ST-5, D. Cauffman
    ATTN: A. Schardt
    ATTN: J. Haughey
    ATTN: D. Dement
    ATTN: P. Kurzhals

NASA
Langley Research Center
    ATTN: MS-168, C. Schexnayder

NASA
Ames Research Center
    ATTN: N-245-3, R. Whitten

NASA
Wallops Flight Center
    ATTN: J. Gray

DEPARTMENT OF DEFENSE CONTRACTORS

Aero-Chem Research Labs., Inc.
    ATTN: A. Fontijn

Aerodyne Research, Inc.
    ATTN: M. Camac
    ATTN: F. Bien

Aeronautical Rsch. Assoc. of Princeton, Inc.
    ATTN: H. Pergament

Aerospace Corp.
    ATTN: V. Josephson
    ATTN: H. Mayer
    ATTN: T. Widhoph
    ATTN: N. Cohen
    ATTN: T. Taylor
    ATTN: J. Reinheimer
    ATTN: I. Garfunkel
    ATTN: F. Morse

University of Alaska
    ATTN: B. Watkins
    ATTN: J. Wagner
 3 cy ATTN: N. Brown

Argonne National Laboratory
    ATTN: Document Control for Lib. Svcs.
           Reports Section

AVCO Everett Research Lab., Inc.
    ATTN: Technical Library
    ATTN: C. Von Rosenberg, Jr.
    ATTN: A830

Battelle Memorial Institute
    ATTN: R. Thatcher
    ATTN: STOIAC
    ATTN: H. Lamuth

Berkeley Research Associates, Inc.
    ATTN: J. Workman

Boston College
 2 cy ATTN: Chairman, Dept. of Physics
 2 cy ATTN: Chairman, Dept. of Chemistry

Boston College
    ATTN: W. Grieder
    ATTN: E. Hegblom

University of California at Riverside
    ATTN: A. Lloyd
    ATTN: J. Pitts, Jr.

California Institute of Technology
    ATTN: J. Ajello

University of California
    ATTN: H. Johnston
    ATTN: W. Miller
    ATTN: H. Strauss
    ATTN: F. Mozer

Calspan Corp.
    ATTN: J. Grace
    ATTN: W. Wurster
    ATTN: M. Dunn
    ATTN: C. Treanor

University of Colorado
    ATTN: C. Lineberger, JILA
    ATTN: G. Lawrence, LASP
    ATTN: J. Pearce, LASP

Columbia University
    ATTN: Security Officer for H. Foley

Columbia University
    ATTN: B. Phelan

Concord Sciences
    ATTN: E. Sutton

Cornell University
    ATTN: M. Kelly

University of Denver
    ATTN: Security Officer for G. Murcray

University of Denver
    ATTN: B. Van Zyl

Environmental Rsch. Inst. of Michigan
    ATTN: IRIA Library

General Electric Co.
    ATTN: F. Alyea
    ATTN: J. Burns
    ATTN: M. Bortner
    ATTN: P. Zavitsanos

General Electric Co.
    ATTN: R. Edsall
    ATTN: T. Baurer

General Electric Company-TEMPO
    ATTN: T. Stevens
    ATTN: W. Knapp
    ATTN: V. Stull
    ATTN: D. Chandler
    ATTN: B. Gambill
    ATTN: J. Jordano
 5 cy ATTN: DASIAC

General Research Corp.
    ATTN: J. Ise, Jr.

Institute for Defense Analyses
    ATTN: H. Wolfhard
    ATTN: E. Bauer

Lockheed Missiles & Space Co., Inc.
    ATTN: T. James
    ATTN: M. Walt
    ATTN: R. Sears
    ATTN: J. Cladis
    ATTN: J. Kumer
    ATTN: J. Reagan
    ATTN: B. McCormac

University of Lowell
    ATTN: G. Best

University of Minnesota
    ATTN: J. Winkler

Mission Research Corp.
    ATTN: Security Office for D. Sappenfield
    ATTN: Security Office for M. Scheibe
    ATTN: Security Office for P. Fischer
    ATTN: Security Office for D. Archer
 5 cy ATTN: Security Office for D. Sowle

Photometrics, Inc.
    ATTN: I. Kofsky
    ATTN: D. Villanucci
    ATTN: W. Andrus

Physical Dynamics, Inc.
    ATTN: A. Thompson

Physical Science Lab
    ATTN: W. Berning

Physical Sciences, Inc.
    ATTN: K. Wray
    ATTN: R. Taylor
    ATTN: G. Caledonia

Physics International Co.
    ATTN: Technical Library

University of Pittsburgh
    ATTN: M. Biondi
    ATTN: F. Kaufman
    ATTN: W. Fite

Princeton University
    ATTN: Librarian

R & D Associates
    ATTN: R. Latter
    ATTN: R. Turco
    ATTN: R. Lindgren
    ATTN: R. Lelevier
    ATTN: H. Ory
    ATTN: F. Gilmore
    ATTN: A. Latter
    ATTN: C. MacDonald
    ATTN: B. Babbard

R & D Associates
    ATTN: J. Rosengren
    ATTN: H. Mitchell

Rand Corp.
    ATTN: C. Crain

Science Applications, Inc.
    ATTN: D. Hamlin
    ATTN: D. Sachs

Space Data Corp.
    ATTN: S. Fisher

SRI International
    ATTN: D. McDaniels
    ATTN: M. Baron
    ATTN: W. Chesnut
    ATTN: R. Leadabrand

SRI International
    ATTN: C. Hulbert

Stewart Radiance Laboratory
    ATTN: R. Huppi

Technology International Corp.
    ATTN: W. Boquist

Teledyne Brown Engineering
    ATTN: J. Beaupre
    ATTN: N. Passino

Utah State University
    ATTN: Security Office for C. Wyatt
    ATTN: Security Office for D. Burt
3 cy ATTN: Security Office for K. Baker
3 cy ATTN: Security Office for D. Baker
    ATTN: Security Office for A. Steed

Visidyne, Inc.
    ATTN: W. Reidy
    ATTN: T. Degges
    ATTN: J. Carpenter
    ATTN: C. Humphrey
    ATTN: H. Smith

Wayne State University
    ATTN: R. Kummler

Wayne State University
    ATTN: W. Kauppila

Yale University
    ATTN: Engineering Department